ulm university universität ulm

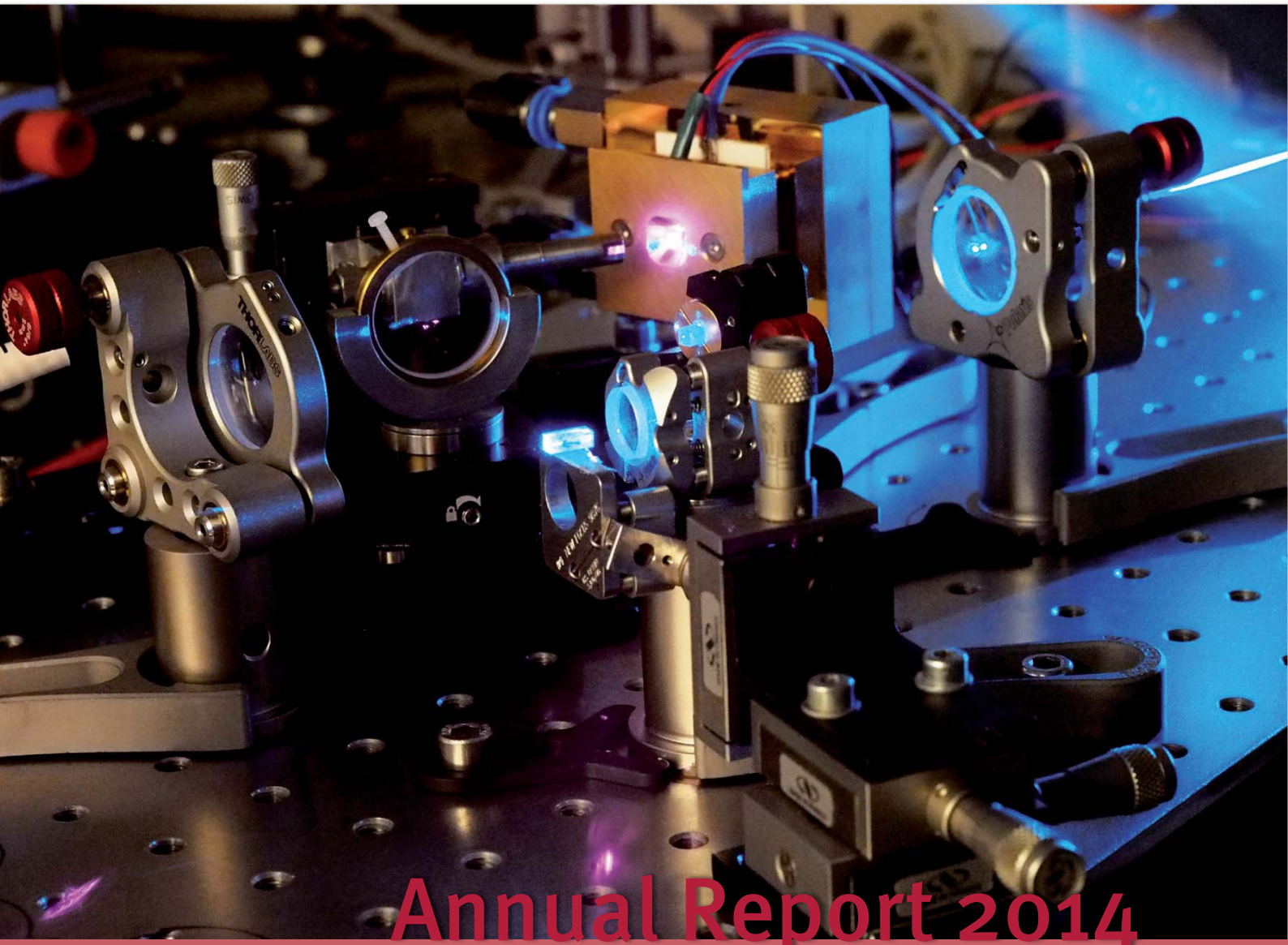

Annual Report 2014

Institute of Optoelectronics

Cover photo:
Optically pumped semiconductor disk laser having a triple-folded external cavity with two nonlinear crystals. The frequency-doubling crystal in the front generates visible blue light with a wavelength of 488 nm. The second crystal provides sum-frequency mixing of the fundamental infra-red radiation at 976 nm and the frequency-doubled light to obtain 90 mW of ultra-violet laser emission at the third harmonic of 325 nm.

Contents

Articles

Lists of Publications

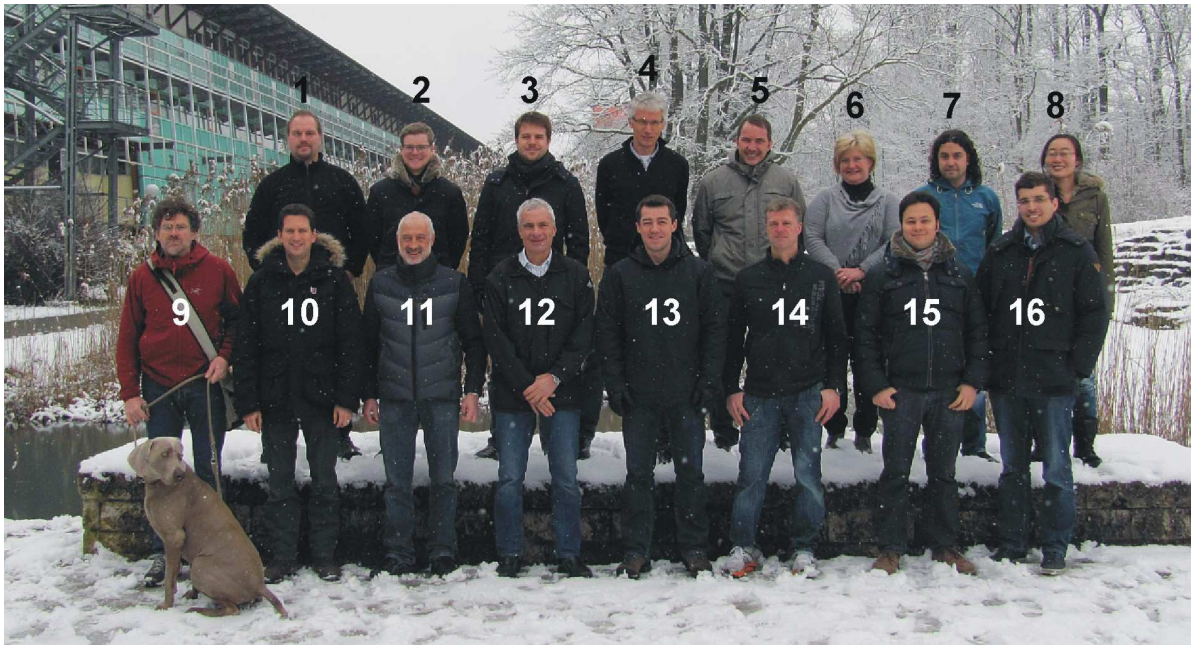

1:	Martin Klein	2:	Sven Bader	3:	Tobias Pusch
4:	Rainer Michalzik	5:	Thomas Zwosta	6:	Hildegard Mack
7:	Tobias Meisch	8:	Junjun Wang	9:	Peter Unger
10:	Markus Daubenschüz	11:	Rudolf Rösch	12:	Ferdinand Scholz
13:	Alexander Hein	14:	Rainer Blood	15:	Marian Caliebe
16:	Dominik Heinz				

Not on the photo:

Karl Joachim Ebeling, Sükran Kilic, Robert Leute, Jürgen Mähnß, Gerlinde Meixner, Susanne Menzel, Eva Nüßle, Ilona Schwaiger

Ulm University
Institute of Optoelectronics

Albert-Einstein-Allee 45, 89081 Ulm, Germany
URL: http://www.uni-ulm.de/opto
Fax: +49–731/50–260 49
Phone: +49–731/50–

Head of Institute			
Prof. Dr.	Peter Unger	–2 60 54	peter.unger@uni-ulm.de
Deputy Head			
Prof. Dr.	Ferdinand Scholz	–2 60 52	ferdinand.scholz@uni-ulm.de
Group Leader			
apl. Prof. Dr.-Ing.	Rainer Michalzik	–2 60 48	rainer.michalzik@uni-ulm.de
President of Ulm University			
Prof. Dr.	Karl Joachim Ebeling	–2 20 00	karl.ebeling@uni-ulm.de
Cleanroom Management			
Dr.-Ing.	Jürgen Mähnß	–2 60 53	juergen.maehnss@uni-ulm.de
Secretaries			
	Sükran Kilic[+]	–2 60 59	suekran.kilic@uni-ulm.de
	Hildegard Mack	–2 60 60	hildegard.mack@uni-ulm.de
	Eva Nüßle	–2 60 50	eva.nuessle@uni-ulm.de
Research Staff			
M. Sc.	Sven Bader	–2 60 37	sven.bader@uni-ulm.de
Dipl.-Ing.	Marian Caliebe	–2 60 39	marian.caliebe@uni-ulm.de
M. Sc.	Markus Daubenschüz	–2 60 38	markus.daubenschuez@uni-ulm.de
Dipl.-Ing.	Alexander Hein	–2 60 46	alexander.hein@uni-ulm.de
Dipl.-Phys.	Dominik Heinz	–2 60 39	dominik.heinz@uni-ulm.de
Dipl.-Ing.	Martin Klein	–2 60 44	martin.klein@uni-ulm.de
Dipl.-Phys.	Robert Leute[*]	–2 60 56	robert.leute@uni-ulm.de
Dipl.-Phys.	Tobias Meisch	–2 60 56	tobias.meisch@uni-ulm.de
M. Sc.	Tobias Pusch	–2 60 37	tobias.pusch@uni-ulm.de
M. Sc.	Junjun Wang[*]	–2 61 95	junjun.wang@uni-ulm.de
Technical Staff			
	Rainer Blood	–2 60 44	rainer.blood@uni-ulm.de
	Gerlinde Meixner	–2 60 41	gerlinde.meixner@uni-ulm.de
	Susanne Menzel	–2 60 41	susanne.menzel@uni-ulm.de
	Rudolf Rösch	–2 60 57	rudolf.roesch@uni-ulm.de
	Ilona Schwaiger[+]	–2 60 56	ilona.schwaiger@uni-ulm.de
	Thomas Zwosta	–2 64 54	thomas.zwosta@uni-ulm.de

[*] Is an alumnus of the Institute meanwhile

[+] Currently on parental leave

Preface

In the year 2014, remarkable progress has been achieved by the three research groups of the Institute of Optoelectronics, as detailed below. Five Ph.D. students have obtained their Dr.-Ing. degrees.

The VCSELs and Optical Interconnects Group has lauched new projects which are conducted in close collaboration with Philips U-L-M Photonics located in Science Park II next to the university campus in Ulm. With electro–optical vertical-cavity surface-emitting laser (VCSEL) modeling we are supporting the development of efficient and temperature-stable lasers suited for 28 Gbit/s digital modulation. Using straintronic techniques we are modifying the optical anisotropy in VCSELs, which is useful for spintronic operation of these lasers. A record-high birefringence of about 250 GHz has been obtained. Furthermore, heterojunction phototransistors with quantum well absorber are investigated in vertical resonant-cavity configurations.

In the GaN Group, we continued our studies about semipolar GaN, where good planar layers could be grown for several semipolar orientations on patterned sapphire wafers. Complete LED structures could be realized, although their electro–optic characteristics are still inferior to c-plane LEDs. First experiments towards semi-insulating GaN grown by hydride vapor phase epitaxy using ferrocene as doping precursor have also been done. GaN-based nanowires grown on N-polar GaN templates show promising performance for sensor applications.

In the High-Power Semiconductor Laser Group, an optically pumped semiconductor disk laser making use of quantum well pumping has been realized. A record continuous-wave output power of close to 7 W has been achieved for a pump wavelength of 940 nm and an emission wavelength of 984 nm. Due to the low quantum defect, the device operates at room temperature and does not need any sophisticated cooling setup, e.g., the use of diamond heat spreaders.

In a major effort to use floor-space in the University West campus more efficiently, the VCSELs and Optical Interconnects Group has entirely rearranged their optical laboratories. This has allowed the GaN Group to move laboratories back to the main location of our Institute in building 45.

Rainer Michalzik
Ferdinand Scholz
Peter Unger Ulm, March 2015

Effects of Miscut of Prestructured Sapphire Substrates and MOVPE Growth Conditions on $(11\bar{2}2)$ Oriented GaN

Marian Caliebe

In this work [1], the influence of sapphire mis-orientation on the quality of coalesced $(11\bar{2}2)$ *GaN layers grown on r-plane prestructured sapphire substrates (r-PSS) is investigated. It was found that the angle of the GaN* $(11\bar{2}2)$ *plane towards the surface plane of the sapphire wafer can be adjusted by the mis-orientation of the substrate. Furthermore, we discovered that the c-direction of GaN is tilted by more than 1° towards the c-direction of the sapphire wafer. Moreover, the influence of the MOVPE growth temperature, V/III ratio and reactor pressure on the coalesced layer has been studied. While a high temperature and small V/III ratio are beneficial, the reactor pressure did not show any significant impact on the crystal quality and surface roughness.*

1. Introduction

While highly efficient blue and red light-emitting diodes (LEDs) are commercially available, yet, there is a lack of efficient LEDs emitting green and yellow light. In literature, this problem is called the "green gap". One possible reason, blamed for this behavior, is the quantum-confined Stark effect. High internal piezo-electric fields separate electrons and holes in the InGaN quantum wells and thus decrease the recombination probability considerably [2–6].

Our approach to reduce the internal field is the use of semipolar $(11\bar{2}2)$ oriented GaN substrates. While there is the possibility to grow $(11\bar{2}2)$ GaN on m-plane sapphire [7], the achievable material quality is poor [8]. Another option is slices, cut from bulk, produced by Hydride Vapor Phase Epitaxy (HVPE). While homoepitaxy permits best results, these substrates are limited in size and are highly expensive [9–11].

Here, the following approach is used: Trenches with a c-plane-like side facet are etched in r-plane sapphire substrates. To prevent growth of a-plane GaN on the $(10\bar{1}2)_{Al_2O_3}$ facet, a SiO_2 layer is deposited by Plasma-Enhanced Chemical Vapor Deposition (PECVD). By Metalorganic Vapor Phase Epitaxy (MOVPE), GaN grows on the c-plane-like facets of the trenches predominantly in c-direction. After a while the individual GaN stripes coalesce to a closed layer. Due to growth in the well established c-direction, a high material quality can be achieved. Also, this method can be easily scaled up, allowing growth on low-priced, large substrates exceeding 100 mm in diameter. It was first demonstrated by Okada et al. [12]. Excellent $(11\bar{2}2)$ GaN layers have also been grown by de Mierry et al. [8] and Leung et al. [13] following this approach.

Typically, such semipolar samples have a fairly large RMS roughness of approximately 50 nm on an area of $50 \times 50\,\mu m^2$. This study was motivated to improve the surface quality. However, by the two attempts described here, we mainly gained other insights. First, the influence of mis-orientation of sapphire wafers has been studied systematically. Then, we searched for proper growth conditions for the GaN layer after coalescence by varying the temperature, V/III ratio and pressure. The impact of the growth temperature and V/III ratio before coalescence has already been studied by Kurisu et al. [14]. However, the focus of their study was to find the optimum growth conditions on a sapphire wafer without any SiO_2 mask and not optimizing the surface quality. By investigating the influence of the growth parameters after coalescence, we want to find optimum conditions for $(11\bar{2}2)$ oriented GaN in particular.

2. Experimental

2.1 Template preparation

All GaN layers are grown on r-plane sapphire substrates (r-PSS). which have been pre-structured as described by S. Schwaiger *et al.* [15]. At first, a 200 nm thick SiO_2 mask layer is deposited by PECVD on the bare r-plane sapphire wafer. By conventional photolithography, resist stripes with a period of 6 µm and a width of 3 µm are manufactured and a Ni etch mask is deposited. After lift-off, the trenches are etched by Reactive-Ion Etching (RIE). The remains of the metal mask are removed wet chemically. The average resulting sidewall angle of the c-plane like facet is 75°.

2.2 MOVPE growth

GaN growth by MOVPE is carried out in a commercial Aixtron-200/4 RF-S HT reactor with the precursors TMGa, NH_3 and TMAl. Following our experience on c-plane GaN growth [16], first an AlN:O nucleation layer with an oxygen content of approximately 10% [17] is deposited at 990°C. A GaN buffer layer follows at 1105°C, a V/III ratio of 870 and a reactor pressure of 150 hPa. After 3.5 min, the reactor temperature is decreased to 1025 °C. After growth of approximately 0.5 µm in c-direction on the sidewalls, GaN growth is paused for the *in-situ* deposition of a SiN_x interlayer that is formed with the precursor SiH_4 [18]. Then, GaN growth continues for 105 min at 1025 °C and a V/III ratio of 870 resulting in a total layer thickness of 5.7 µm.

3. Mis-Orientation of the Sapphire Substrate

As calculated in [15], the theoretical angle between the $(11\bar{2}2)_{GaN}$ and $(0001)_{GaN}$ plane is 58.41°, while the angle between the r- and c-plane of the sapphire substrate is only 57.61°. Thus, if we assume that the c-planes of GaN and sapphire are parallel, the theoretical angle of the $(11\bar{2}2)_{GaN}$ plane towards the $(0001)_{GaN}$ plane differs from the angle of the $(10\bar{1}2)_{Al_2O_3}$ plane towards the $(0001)_{Al_2O_3}$ plane by 0.8°. Hence, the $(11\bar{2}2)_{GaN}$ plane is expected to be tilted with respect to the surface (for exactly oriented r-plane sapphire

wafers), which might lead to a saw-tooth like coalesced layer and a rough surface (Fig. 1). Using mis-oriented sapphire substrates could compensate this tilt so that the individual GaN stripes can coalesce without height difference. This motivated some other groups to use sapphire wafers with a miscut of 0.5° [12, 14, 19]. Kurisu et al. measured an angle of 0.29° of a macrostep on the surface by Atomic Force Microscopy (AFM), which supports this expectation [14]. However, systematic studies about the influence of various miscut angles on the properties of the final semipolar GaN layer have not yet been reported.

Therefore, we have investigated the influence of the mis-orientation in more detail: For this experiment, we have taken sapphire wafers with a mis-orientation of 0.0°, 0.5°, 1.0° and 1.5° around the a-axis towards the c-direction (Fig. 1). The wafers are patterned and growth is carried out as described above.

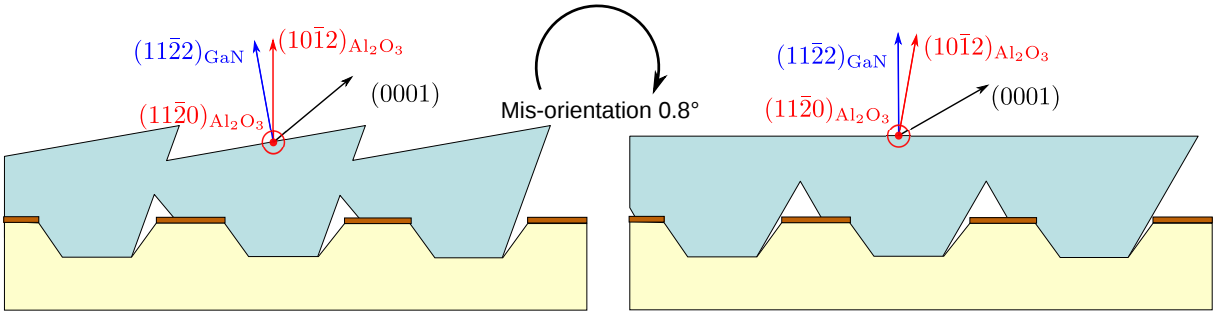

Fig. 1: Hypothesis: By using mis-oriented sapphire wafers the GaN $(11\bar{2}2)$ plane might be aligned parallel to the surface (angles exaggerated).

The crystallographic orientations of the $(11\bar{2}2)_{GaN}$, $(0006)_{GaN}$, $(10\bar{1}2)_{Al_2O_3}$ and $(00012)_{Al_2O_3}$ with respect to each other have been measured by High Resolution X-ray Diffraction (HRXRD) in a Bragg-Brentano configuration. For highest accuracy, ω and 2θ of the planes $(11\bar{2}2)_{GaN}$, $(0006)_{GaN}$ and $(10\bar{1}2)_{Al_2O_3}$ have been determined in an asymmetric scan. Then, the reciprocal space coordinates s_x and s_z of these reflexes have been calculated as described in [20]. From the position in reciprocal space, the angular difference follows directly. However, due to geometric limitations, it is not possible to measure the $(00012)_{Al_2O_3}$ reflex in this way. Therefore, the inclination of the c-planes has been determined by using additional symmetric χ-scans.

As can be seen in Fig. 2 (a), the c-planes of GaN and sapphire are tilted by more than 1° towards each other and are not in parallel as previously assumed. Thus, the $(11\bar{2}2)_{GaN}$ and $(10\bar{1}2)_{Al_2O_3}$ planes are more parallel than the theoretical tilt of 0.8° (Fig. 2 (b)). This results in an offset of the orientation of the $(11\bar{2}2)_{GaN}$ plane towards the wafer surface (Fig. 2 (c)). From this series, the sample without miscut is the one with the most parallel $(11\bar{2}2)_{GaN}$ plane with respect to the wafer surface.

However, the influence of the mis-orientation on the full width at half maximum (FWHM) of the HRXRD rocking curves and surface roughness is almost negligible (Fig. 3). From statistics of several wafers, grown under exactly the same conditions, the error-bar of the HRXRD and AFM measurements has been determined to 10% and 15%, respectively.

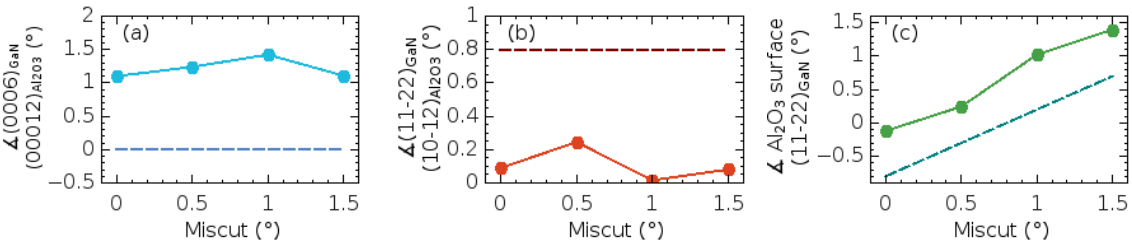

Fig. 2: Measured data and expected angles (dashed line) of tilt between different lattice planes and wafer surface, respectively. (a) Angle between the c-planes of GaN and Al_2O_3. (b) Angle between the $(11\bar{2}2)_{GaN}$ and $(10\bar{1}2)_{Al_2O_3}$ plane. (c) Orientation of the $(11\bar{2}2)_{GaN}$ plane towards the wafer surface plane.

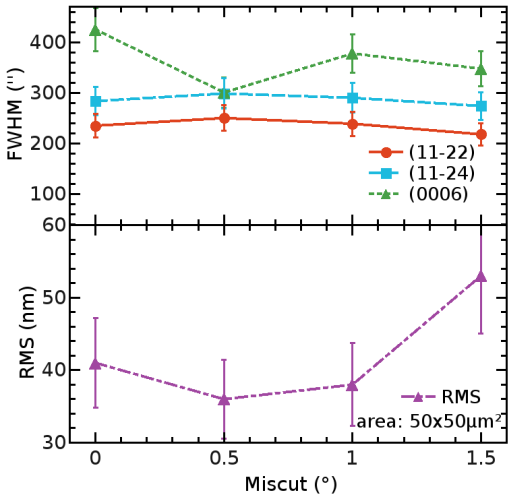

Fig. 3: FWHM of HRXRD rocking curves (top) and surface roughness (bottom) measured by atomic force microscopy (AFM).

Regarding the low-temperature ($T = 13\,\mathrm{K}$) photoluminescence (PL) spectra (Fig. 4), the miscut decreases the intensity of the peak related to the density of basal plane stacking faults (BSF) with respect to the band of the donor bound exciton D^0X, whose FWHM is slightly decreasing as well. From cathodoluminescence measurements (CL) and transmission electron microscopy (TEM) [15, 21], we know that the BSFs are mainly present in the -c-wing and are overgrown by the +c-wing (see also [22, 23]). With an estimated absorption coefficient of $\alpha = 1 \cdot 10^5 \mathrm{cm}^{-1}$ [24, 25], we obtain a penetration depth of 100 nm only, for our exciting laser beam ($\lambda = 325\,\mathrm{nm}$). Thus, by PL, we only see the BSFs penetrating to the surface.

4. Variation of Growth Parameters of GaN Top Layer

In a next step, we investigated the influence of various growth parameters of the GaN layer after coalescence in order to minimize the surface roughness and improve its crystalline

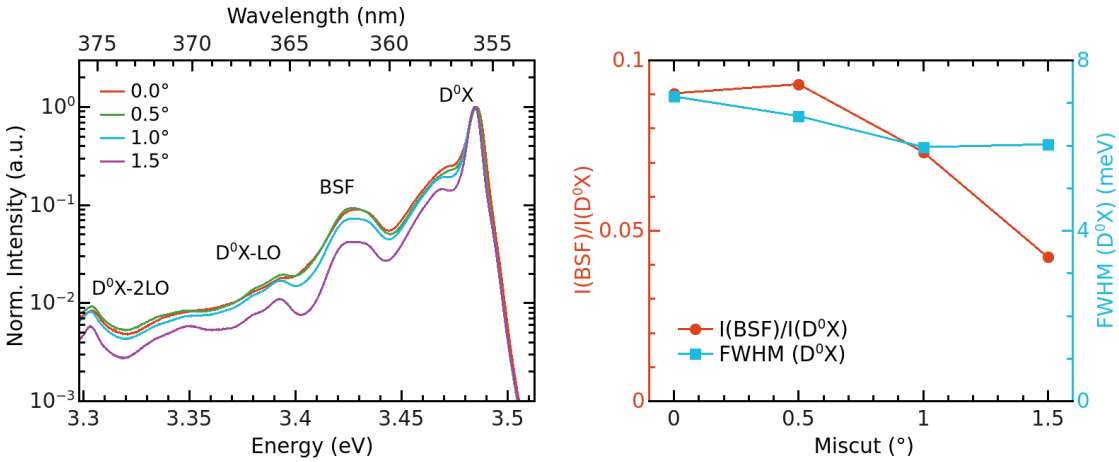

Fig. 4: Left: PL spectra, normalized to the donor-bound excitonic transition D^0X. Right: Ratio of BSF peak and D^0X peak intensities and FWHM of D^0X. The basal plane stacking fault luminescence (BSF) is decreasing with higher miscut.

quality. The samples investigated here are grown on sapphire wafers without miscut and are produced as described in Sect. 2. Here, after the deposition of the SiN_x interlayer, GaN growth continues for only 60 min under the conditions described above. Then, the TMGa flux is increased from 26 sccm to 40 sccm (growth rate increases from 2.9 µm/h to 4.4 µm/h) and growth is continued for another 60 min with several top layer variations. The resulting total layer thickness (measured from the sapphire surface) is approximately 7.9 µm.

Beside the growth temperature and V/III ratio studies that are discussed below, the reactor pressure has been decreased from 150 hPa to 75 hPa in a further experiment. However, there was no observable difference in the crystal quality or surface roughness.

4.1 Temperature variation

When increasing the growth temperature, at a V/III ratio of 565, the BSF luminescence is decreasing, pointing to a reduction of the BSF density (Fig. 5). Moreover, the FWHM of the donor bound exciton signal D^0X becomes narrower and the free exciton band (FE) appears.

While there seems to be a minimum for the surface roughness at 1066 °C (Fig. 6 (bottom)), the FWHM of the HRXRD rocking curves is hardly influenced (Fig. 6 (top)) by the growth temperature. Fig. 7 shows an AFM micrograph of the sample grown at $T = 1066$°C at a V/III ratio of 565. Typical for those samples are the flaky appearance and "arrow-head" shaped elevations.

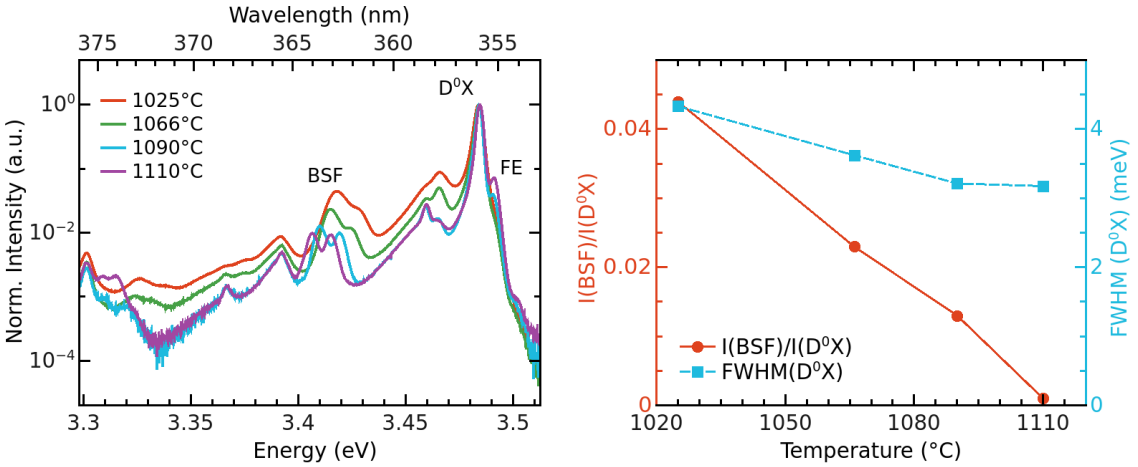

Fig. 5: Normalized PL spectra. The intensity of the basal plane stacking fault related peak (BSF) is decreasing with higher temperature and the FWHM of the D^0X becomes narrower while the band of free excitons (FE) appears.

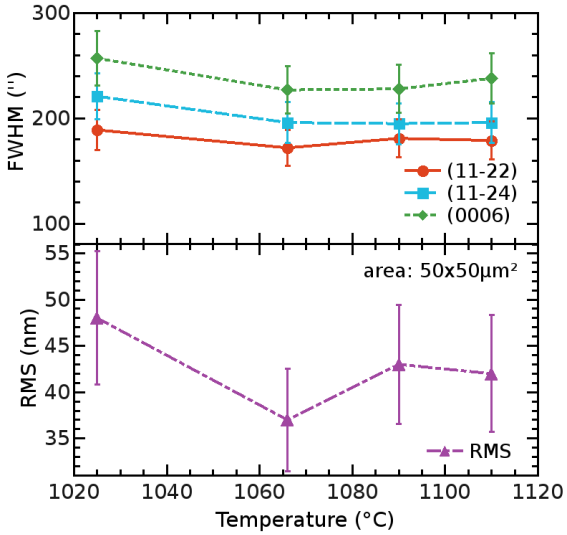

Fig. 6: The growth temperature shows almost no influence on the FWHM of HRXRD rocking curves (top). However, there seems to be a minimum of the surface roughness at 1066 °C (bottom).

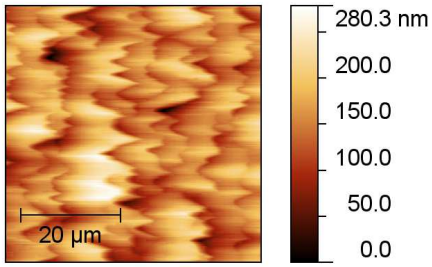

Fig. 7: AFM micrograph of the sample grown at $T = 1066$°C at a V/III ratio of 565.

4.2 V/III ratio variation

The conditions from the temperature series that led to the smallest surface roughness (f(TMGa) = 40 sccm, T = 1066 °C) were chosen for a subsequent V/III ratio variation, by varying the NH_3 flux. The total gas flux in the reactor has been kept constant by compensating with H_2.

With decreasing V/III ratio, the intensity of the BSF related peak and the FWHM of the D^0X become smaller and the free exciton band (FE) emerges (Fig. 8). Also, both the FWHM of HRXRD rocking curves and the surface roughness improve for V/III ratios around 150 (Fig. 9).

The slightly larger RMS values of this series (Fig. 9), as compared to the temperature series (Fig. 6), are probably caused by small process fluctuations in sapphire structuring and MOVPE growth in not subsequently manufactured samples.

5. Summary

These studies show that the orientation of the $(11\bar{2}2)_{GaN}$ plane towards the wafer surface can be adjusted by using sapphire wafers with miscut. However, we observed that the c-plane of GaN is tilted by more than 1° towards the c-plane of the sapphire template on all wafers. Thus, for sapphire wafers without mis-orientation, the $(11\bar{2}2)_{GaN}$ plane is already parallel to the surface. While the PL spectra can be interpreted as slight improvements of the crystal quality with increasing wafer miscut, there is hardly any change visible in HRXRD and AFM.

In experiments with various top layer growth conditions, we found that a high growth temperature above 1066 °C and moderate V/III ratio of 150 seems to be beneficial for

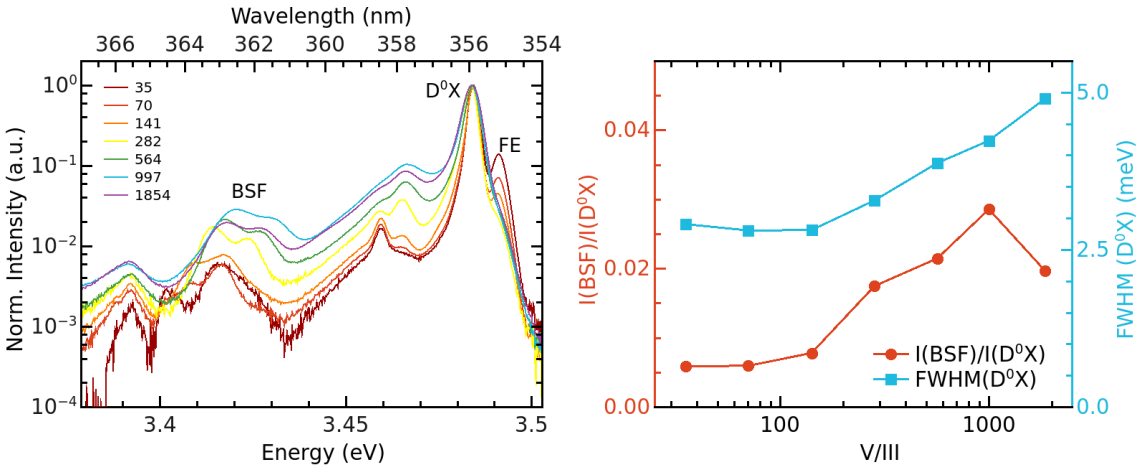

Fig. 8: Left: Normalized PL spectra. The band of free excitons (FE) appears at a small V/III ratio. Right: The basal plane stacking fault luminescence (BSF) and the FWHM of the D^0X are decreasing with smaller V/III ratio.

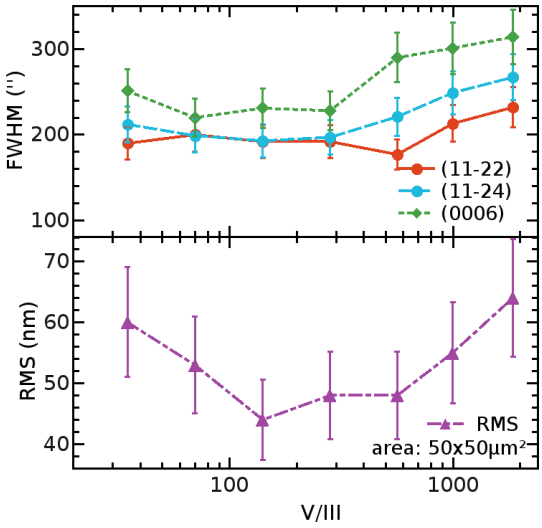

Fig. 9: Top: FWHM of HRXRD rocking curves. Bottom: Surface roughness measured by AFM.

crystal quality and surface roughness. However, the surface roughness can not be improved considerably by varying the growth parameters of the coalesced layers only.

Acknowledgment

I thank the coauthors of this article [1] T. Meisch and F. Scholz of the Institute of Optoelectronics at Ulm University and M. Madel of the Institute of Quantum Matter, Semiconductor Physics Group at Ulm University for their scientific support. We gratefully acknowledge the support of K. Thonke of the Institute of Quantum Matter, Semiconductor Physics Group, in interpreting the PL spectra. For their technical contribution, we thank R. Rösch, C. Steinmann and Z. Cheng of the Institute of Optoelectronics. This work was financially supported by the European Commission (FP7) within the framework of the project "AlGaInN materials on semi-polar templates for yellow emission in solid state lighting applications" (ALIGHT).

References

[1] M. Caliebe, T. Meisch, M. Madel, and F. Scholz, "Effects of miscut of prestructured sapphire substrates and MOVPE growth conditions on (11$\bar{2}$2) oriented GaN", *J. Cryst. Growth*, vol. 414, pp. 100–104, 2015.

[2] F. Scholz, T. Wunderer, B. Neubert, F. Feneberg, and K. Thonke, "GaN-based light-emitting diodes on selectively grown semipolar crystal facets", *MRS Bulletin*, vol. 34, pp. 328–333, 2009.

[3] T. Takeuchi, H. Amano, and I. Akasaki, "Theoretical study of orientation dependence of piezoelectric effects in wurtzite strained GaInN/GaN heterostructures and quantum wells", *Jpn. J. Appl. Phys.*, vol. 39, pp. 413–416, 2000.

[4] F. Bernardini, V. Fiorentini, and D. Vanderbilt, "Spontaneous polarization and piezoelectric constants of III-V nitrides", *Phys. Rev. B*, vol. 56, pp. R10024–R10027, 1997.

[5] O. Ambacher, "Growth and applications of group III-nitrides", *J. Phys. D: Appl. Phys.*, vol. 31, pp. 2653–2710, 1998.

[6] A.E. Romanov, T.J. Baker, S. Nakamura, and J.S. Speck, "Strain-induced polarization in wurtzite III-nitride semipolar layers", *J. Appl. Phys.*, vol. 100, pp. 023522-1–10, 2006.

[7] T.J. Baker, B.A. Haskell, F. Wu, J.S. Speck, and S. Nakamura, "Characterization of planar semipolar gallium nitride films on sapphire substrates", *Jpn. J. Appl. Phys.*, vol. 45, pp. L154–L157, 2006.

[8] P. de Mierry, N. Kriouche, M. Nemoz, S. Chenot, and G. Nataf, "Semipolar GaN films on patterned r -plane sapphire obtained by wet chemical etching", *Appl. Phys. Lett.*, vol. 96, pp. 231918-1–3, 2010.

[9] M. Ueda, K. Kojima, M. Funato, Y. Kawakami, Y. Narukawa, and T. Mukai, "Epitaxial growth and optical properties of semipolar (11-22) GaN and InGaNâGaN quantum wells on GaN bulk substrates", *Appl. Phys. Lett.*, vol. 89, pp. 211907-1–3, 2006.

[10] K. Fujito, S. Kubo, and I. Fujimura, "Development of bulk GaN crystals and nonpolar/semipolar substrates by HVPE", *MRS Bull.*, vol. 34, pp. 313–317, 2009.

[11] F. Scholz, "Semipolar GaN grown on foreign substrates: a review", *Semicond. Sci. Technol.*, vol. 27, pp. 024002-1–15, 2012.

[12] N. Okada, A. Kurisu, K. Murakami, and K. Tadatomo, "Growth of semipolar (11-22) GaN layer by controlling anisotropic growth rates in r -plane patterned sapphire substrate", *Appl. Phys. Express*, vol. 2, pp. 091001-1–3, 2009.

[13] B. Leung, Q. Sun, C. Yerino, Y. Zhang, J. Han, B.H. Kong, H.K. Cho, K.Y. Liao, and Y.L. Li, "Growth evolution and microstructural characterization of semipolar $(11\bar{2}2)$ GaN selectively grown on etched r-plane sapphire", *J. Cryst. Growth*, vol. 341, pp. 27–33, 2012.

[14] A. Kurisu, K. Murakami, Y. Abe, N. Okada, and K. Tadatomo, "Characterization of semipolar $(11\bar{2}2)$ GaN on c-plane sapphire sidewall of patterned r-plane sapphire substrate without SiO_2 mask", *Phys. Status Solidi C*, vol. 7, pp. 2059–2062, 2010.

[15] S. Schwaiger, S. Metzner, T. Wunderer, I. Argut, J. Thalmair, F. Lipski, M. Wieneke, J. Bläsing, F. Bertram, J. Zweck, A. Krost, J. Christen, and F. Scholz, "Growth and coalescence behavior of semipolar $(11\bar{2}2)$ GaN on pre-structured r-plane sapphire substrates", *Phys. Status Solidi B*, vol. 248, pp. 588–593, 2011.

[16] J. Hertkorn, P. Brückner, S.B. Thapa, T. Wunderer, F. Scholz, M. Feneberg, K. Thonke, R. Sauer, M. Beer, and J. Zweck, "Optimization of nucleation and buffer layer growth for improved GaN quality", *J. Cryst. Growth*, vol. 308, pp. 30–36, 2007.

[17] J. Bläsing, A. Krost, J. Hertkorn, F. Scholz, L. Kirste, A. Chuvilin, and U. Kaiser, "Oxygen induced strain field homogenization in AlN nucleation layers and its impact on GaN grown by metal organic vapor phase epitaxy on sapphire: An x-ray diffraction study", *J. Appl. Phys.*, vol. 105, pp. 033504-1–9, 2009.

[18] M. Caliebe, T. Meisch, B. Neuschl, S. Bauer, J. Helbing, D. Beck, K. Thonke, M. Klein, D. Heinz, and F. Scholz, "Improvements of MOVPE grown $(11\bar{2}2)$ oriented GaN on pre-structured sapphire substrates using a SiN_x interlayer and HVPE overgrowth", *Phys. Status Solidi C*, vol. 11, pp. 525–529, 2014.

[19] H. Furuya, Y. Hashimoto, K. Yamane, N. Okada, and K. Tadatomo, "Characterization of {11-22} GaN grown using two-step growth technique on shallowly etched r-plane patterned sapphire substrates", *J. Cryst. Growth*, vol. 391, pp. 41–45, 2014.

[20] M.A. Moram and M.E. Vickers, "X-ray diffraction of III-nitrides", *Rep. Prog. Phys.*, vol. 72, pp. 036502-1–40, 2009.

[21] Y. Han, M. Caliebe, T. Meisch, M. Pristovsek, M. Kappers, F. Scholz, and C. Humphreys, "Structural characterisation of semi-polar GaN templates grown on pre-structured r-plane sapphire substrates", in *15th European Workshop on Metalorganic Vapour Phase Epitaxy (EWMOVPE XV), June 2-5, 2013, Aachen, Germany, Extended Abstracts*, pp. 55–58, Forschungszentrum Jülich GmbH, 2013.

[22] N. Kriouche, M. Leroux, P. Vennéguès, M. Nemoz, G. Nataf, and P. de Mierry, "Filtering of defects in semipolar (11-22) GaN using 2-steps lateral epitaxial overgrowth", *Nanoscale Res. Lett.*, vol. 5, pp. 1878–1881, 2010.

[23] B. Lacroix, M.P. Chauvat, P. Ruterana, G. Nataf, and P. de Mierry, "Efficient blocking of planar defects by prismatic stacking faults in semipolar (11-22)-GaN layers on m-sapphire by epitaxial lateral overgrowth", *Appl. Phys. Lett.*, vol. 98, pp. 121916-1–3, 2011.

[24] J.F. Muth, J.H. Lee, I.K. Shmagin, R.M. Kolbas, H.C. Casey Jr., B.P. Keller, U.K. Mishra, and S.P. DenBaars, "Absorption coefficient, energy gap, exciton binding energy, and recombination lifetime of GaN obtained from transmission measurements", *Appl. Phys. Lett.*, vol. 71, pp. 2572–2574, 1997.

[25] R. Dingle, D.D. Sell, S.E. Stokowski, P.J. Dean, and R.B. Zetterstrom, "Absorption, reflectance, and luminescence of GaN single crystals", *Phys. Rev. B*, vol. 3, pp. 497–500, 1971.

Doping Behavior of $(11\bar{2}2)$-GaN Grown on Patterned Sapphire Substrates

Tobias Meisch

We present results of the investigation on the doping behavior of planar semipolar $(11\bar{2}2)$*-oriented GaN grown on* $(10\bar{1}2)$ *patterned sapphire substrates mainly focusing on the magnesium incorporation. We observed that Mg is incorporated with much lower efficiency into the* $(11\bar{2}2)$ *plane as compared to polar c-plane GaN. This problem could be decreased by varying the growth temperature. On the one hand, at reduced growth temperature we observed higher Mg concentrations while keeping the Mg flow constant. On the other hand, parasitic background charge carriers due to defects, O-doping etc. could be reduced simultaneously. Using these conclusions, a planar semipolar InGaN/GaN-LED on* $(11\bar{2}2)$*-oriented GaN was grown. Electroluminescence measurements show a suitable electrical and optical performance.*

1. Introduction

Most of the common optoelectronic devices based on group III nitrides emitting in the visible and ultraviolet range are grown in the well-known c-direction. Lots of techniques are investigated already to achieve excellent crystal quality and smooth surfaces. Nevertheless, the crystal symmetry of the group III nitrides causes strong piezoelectric fields in heterostructures like InGaN/GaN, leading to a bending of the valence and conduction band. The wave functions of electrons and holes get spatially separated and the recombination probability is significantly reduced [1]. Furthermore, the effective band gap decreases resulting in a redshift of the emission spectrum. This behavior is known as quantum confined Stark effect (QCSE). To reduce or even avoid these internal piezoelectric fields, the growth in non-c-directions has been proposed. The epitaxy of nonpolar GaN (perpendicular to the c-axis) is typically dominated by a poor crystal quality. Choosing semipolar directions like $(11\bar{2}2)$, $(10\bar{1}1)$, or $(20\bar{2}1)$ seems to be a good compromise between a reasonable crystal quality and a reduced QCSE. For these particular directions, the amount of the piezoelectric field is reduced to a third as compared to c-plane and additionally, the field direction is inverted. Therefore, an externally applied voltage counteracts the internal field and hence reduces the band bending. However, the epitaxy of $(11\bar{2}2)$ GaN seems to be a big challenge. Typically, $(11\bar{2}2)$ GaN templates are produced by cutting thick c-plane wafers grown by HVPE, which results in wafers limited in size to just a few square mm [2]. This limitation can be overcome by growing such GaN layers on foreign substrates like sapphire or silicon with uncommon orientations. Similar as reported by Okada et al. [3], we are able to grow $(11\bar{2}2)$ GaN layers on $(10\bar{1}2)$ patterned sapphire

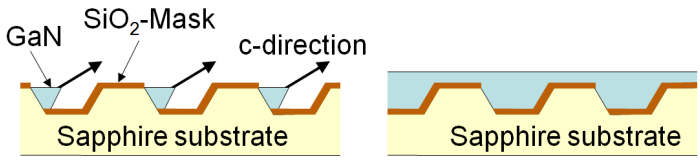

Fig. 1: Patterned sapphire substrate, schematically. All non-c-plane facets are covered with SiO_2 (brown) avoiding parasitic growth. The GaN nucleates on the c-plane sidewall, forms triangular-shaped stripes (left) and coalesces after a suitable growth time to a closed semipolar surface (right).

substrates with a reasonable crystal quality. By etching trenches into these wafers, c-plane-like sidewalls are formed on which the growth of GaN starts developing triangular shaped stripes. After a suitable growth time, these stripes coalesce and form a planar $(11\bar{2}2)$ oriented surface (see Fig. 1). By this procedure, we make use of the well-established growth in c-direction, eventually resulting in a semipolar surface. This approach offers some essential advantages: First, the growth of a full LED or laser diode structure in a single epitaxy run is possible. Second, the diameter of the template is just limited by the reactor size. In our studies, 2“ diameter sapphire wafers were used. Well-known from the growth of c-plane GaN, a SiN mask can help to stop defects penetrating to the surface and therefore reduce the defect density in the subsequent layers significantly [4]. Most of the common materials acting as an acceptor in GaN like oxygen and silicon show a very high incorporation efficiency. Therefore, achieving $(11\bar{2}2)$-oriented GaN layer with a suitable n-conductivity is not a big challenge. However, on the other side a parasitic n-doping (due to impure material sources, external leakages etc.) means a more challenging p-doping process. On the one hand, to achieve a reasonable hole concentration, one has to compensate all free electrons in the layer at first. On the other hand, magnesium acts in GaN indeed as an acceptor, but due to the comparably high activation energy of about 200 meV not very efficient [5]. For c-plane oriented InGaN/GaN-LEDs it is known, that for a suitable hole concentration in the range of $8{\cdot}10^{17}\,\mathrm{cm}^{-3}$, a Mg concentration of more than $10^{19}\,\mathrm{cm}^{-3}$ is necessary [7]. However, it is reported that the Mg incorporation in $(11\bar{2}2)$-oriented GaN is less efficient than in c-plane surfaces [6]. To establish a suitable p-doping process for our semipolar GaN structures, the doping behavior of Mg and related parasitic materials was investigated systematically.

2. Experimental

2.1 Structuring process and growth of $(11\bar{2}2)$ GaN

In order to achieve $(11\bar{2}2)$ GaN as described above, we have etched trenches into $(10\bar{1}2)$ oriented sapphire wafers. At the beginning of the structuring process, an about 1.7 µm thick layer of a negative photoresist is spin-coated on the substrate, which is patterned by optical lithography with a stripe shadow mask with an opening of 3 µm and a period of 6 µm. Via reactive ion etching, the stripes get transferred into the sapphire substrate.

Covering all non-c-plane-like facets with SiO_2 (see Fig. 1) by directed sputtering prevents parasitic growth.

The MOVPE growth was done in a commercial Aixtron-200/4 RF-S HT reactor using the standard precursors ammonia (NH_3), trimethylgallium (TMGa) and trimethylaluminum (TMAl). The growth starts with our about 20 nm thick standard AlN nucleation layer at relatively low temperature of about 950 °C [8]. For the subsequent GaN growth a reactor temperature of about 1020 °C is choosen. The GaN gets pushed in c-direction and builds triangularly formed stripes, which coalesce after a suitable growth time to a planar, semipolar $(11\bar{2}2)$-oriented surface. An in-situ deposited SiN interlayer helps to improve the crystal quality by stopping defects penetrating to the sample surface [4]. By decreasing the growth temperature of the topmost GaN layer to 970 °C, the growth gets pushed further in c-direction and the coalescence of the stripes gets improved. The total thickness of the GaN layer is about 5 µm. X-ray rocking curve measurements give a FWHM of about 200 arcsec for the $(11\bar{2}2)$ reflection indicating a suitable crystal quality. Atomic force microscopy (AFM) measurements show a surface roughness of 10 nm in an area of 70 µm × 70 µm.

From low temperature photoluminescence (PL) measurements (10 K), using a 1000 mm monochromator and a 1200 mm^{-1} grating, we obtained more detailed information about defects and doping behavior close to the crystal surface.

2.2 n-doped GaN

The doping experiments have been performed in parallel on standard c-plane wafers and our semipolar $(11\bar{2}2)$ samples to investigate possible differences from our well-established c-plane results. Therefore, (0001) and $(11\bar{2}2)$ GaN were overgrown side by side with Si-doped GaN. The Si flow was systematically varied between 6 nmol/min and 17.5 nmol/min. The Si concentration was then analyzed by secondary ion mass spectrometry (SIMS)[2] (see Fig. 2). Obviously, the incorporation efficiency of silicon is independent of the surface orientation within reasonable error bars, similar as reported by other research groups like Xu et al. [9]. Standard InGaN/GaN-LEDs require an electron density of about $10^{19}\,cm^{-3}$ in the n-layer. Therefore, a molar Si flow of 12 nmol/min was established for the n-layer of the InGaN/GaN-LEDs grown on $(11\bar{2}2)$ oriented GaN (see below).

2.3 Parasitic background doping of GaN

To achieve a suitable hole concentration, the parasitic electron density due to O, Si, defects etc. has to be suppressed as much as possible. Hall measurements show a very high electron density of $7{\cdot}10^{18}\,cm^{-3}$ in $(11\bar{2}2)$ layers grown at a temperature of 970 °C. A growth temperature variation of nominally undoped $(11\bar{2}2)$ GaN was done. Subsequent Hall measurements show a strong temperature dependence of the parasitic electron concentration (see Fig. 3). In the range of 910 °C there seems to be a minimum with $1.5{\cdot}10^{18}\,cm^{-3}$. Compared to our standard c-plane oriented GaN layers with a parasitic

[2]Done by Lutz Kirste, Fraunhofer-Institut für Angewandte Festkörperphysik IAF, Freiburg

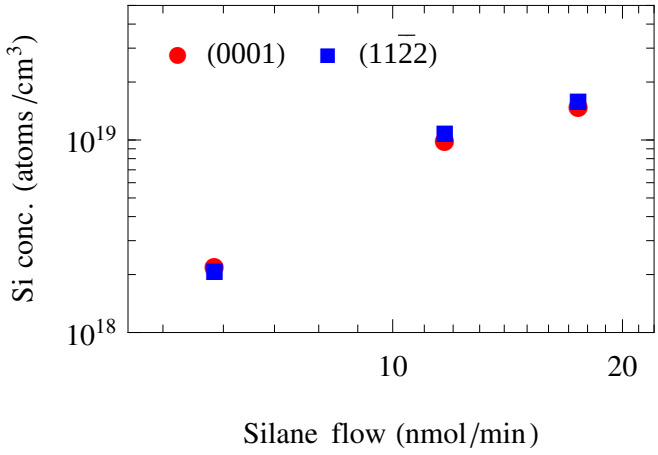

Fig. 2: Silicon concentration in GaN depending on the molar Si flow measured by SIMS.

electron density below $10^{16}\,\mathrm{cm}^{-3}$, it is still a very high value. A further reduction of the growth temperature leads to a poor crystal quality and therefore to an increasing electron density again.

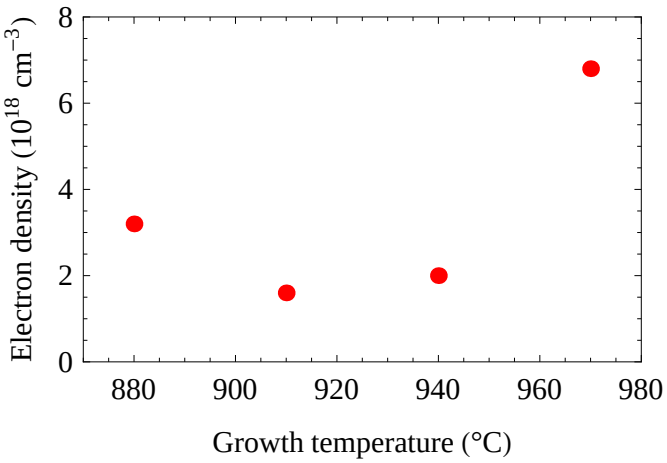

Fig. 3: Electron concentration in nominally undoped GaN grown at different temperatures.

2.4 p-doped GaN

Analog to the Si doping, (0001) and (11$\bar{2}$2) GaN were overgrown side by side also with Mg-doped GaN. The magnesium flow was systematically varied between 100 nmol/min and 350 nmol/min. Subsequent SIMS measurements (see Fig. 4, left) show that, grown at a temperature of 970 °C, (11$\bar{2}$2)-oriented GaN seems to incorporate just a tenth compared to a polar surface. This means that a 10 times larger Mg flow is needed to achieve the same Mg content on (11$\bar{2}$2) surfaces as compared to c-plane. Similar results were reported by Cruz *et al.* in 2009 [6]. Using these growth conditions, a maximum hole concentration

of $1{\cdot}10^{17}\,\mathrm{cm}^{-3}$ with a Mg flux of 390 nmol/min was achievable. Unfortunately, this value is still far away from desirable hole concentration in the range of $8{\cdot}10^{17}\,\mathrm{cm}^{-3}$, as mentioned before. Moreover, LEDs grown with this p-layer showed a fairly low output power. This may be caused by a degradation of the quantum wells during the subsequent p-GaN overgrowth at such comparably high temperatures. Emitting at a wavelength of 470 nm, the semipolar InGaN/GaN-LED had a fairly low optical output power of 50 µW at 20 mA driving current.

In order to reduce the parasitic background n-conductivity (cf. Sect. 2.3) and the thermal treatment of the InGaN/GaN-QWs due to the p-layer growth, its growth temperature should be reduced as much as possible. Corresponding investigations of the temperature dependence of the Mg incorporation show a significantly increased Mg incorporation efficiency at lower reactor temperatures (see Fig. 4, right). Keeping the Mg flow constant and reducing the temperature from 970 °C to 910 °C, the Mg concentration gets more than doubled. A further reduction of the growth temperature leads, as already mentioned, to a poor crystal quality and an increasing electron density again. Therefore, the temperature of the p-doped layer was fixed at this temperature as well.

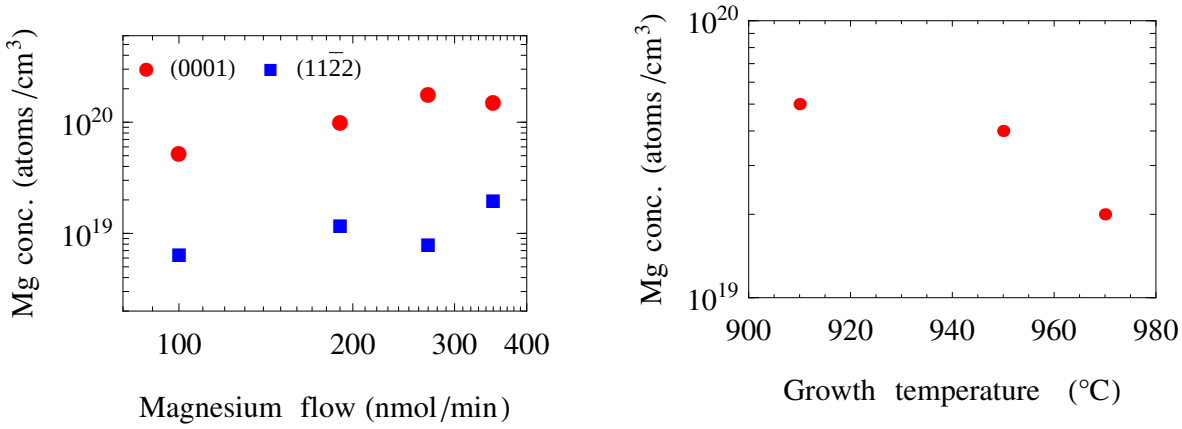

Fig. 4: Left: Magnesium concentration in GaN depending on the molar Mg flow measured by SIMS. Right: Growth temperature dependend Mg incorporation for a Mg flow of 350 nmol/min measured by SIMS.

Hall measurements are a standard method to investigate the carrier density in p-doped GaN. Unfortunately, a too low Mg doping is not able to compensate the parasitic electrons — the p-doped GaN layer is (semi-) isolating. A too high doping level leads to a high defect density, which increases the parasitic electron density as well — the p-doped GaN layer may be again (semi-) isolating. To distinguish between these two situations just by Hall measurements is difficult. However, a too high Mg content leads to a very strong defect related signal in low temperature photoluminescence (LTPL) measurements, whereas a too low p-doped layer gives just a weak donor-acceptor-pair (DAP) transition related signal. In Fig. 5 (left, top), the LTPL signal of the sample with a Mg flow of 390 nmol/min grown at 910 °C is shown. A very intense defect related signal at 3.1 eV is visible, which indicates, as already mentioned, a too high Mg content. Reducing the Mg flow to 140 nmol/min, a first DAP related signal is indicated. A further reduction of the Mg flow to 50 nmol/min

leads to a very clear DAP signal at 3.28 eV. The corresponding phonon replica at 3.19 eV, 3.10 eV and so on are clearly visible as well. Hall measurements on this sample show a hole density of $1.2{\cdot}10^{17}\,\mathrm{cm}^{-3}$, which is still, as already mentioned, far away from the desired value of $8{\cdot}10^{17}\,\mathrm{cm}^{-3}$ for an InGaN/GaN-LED.

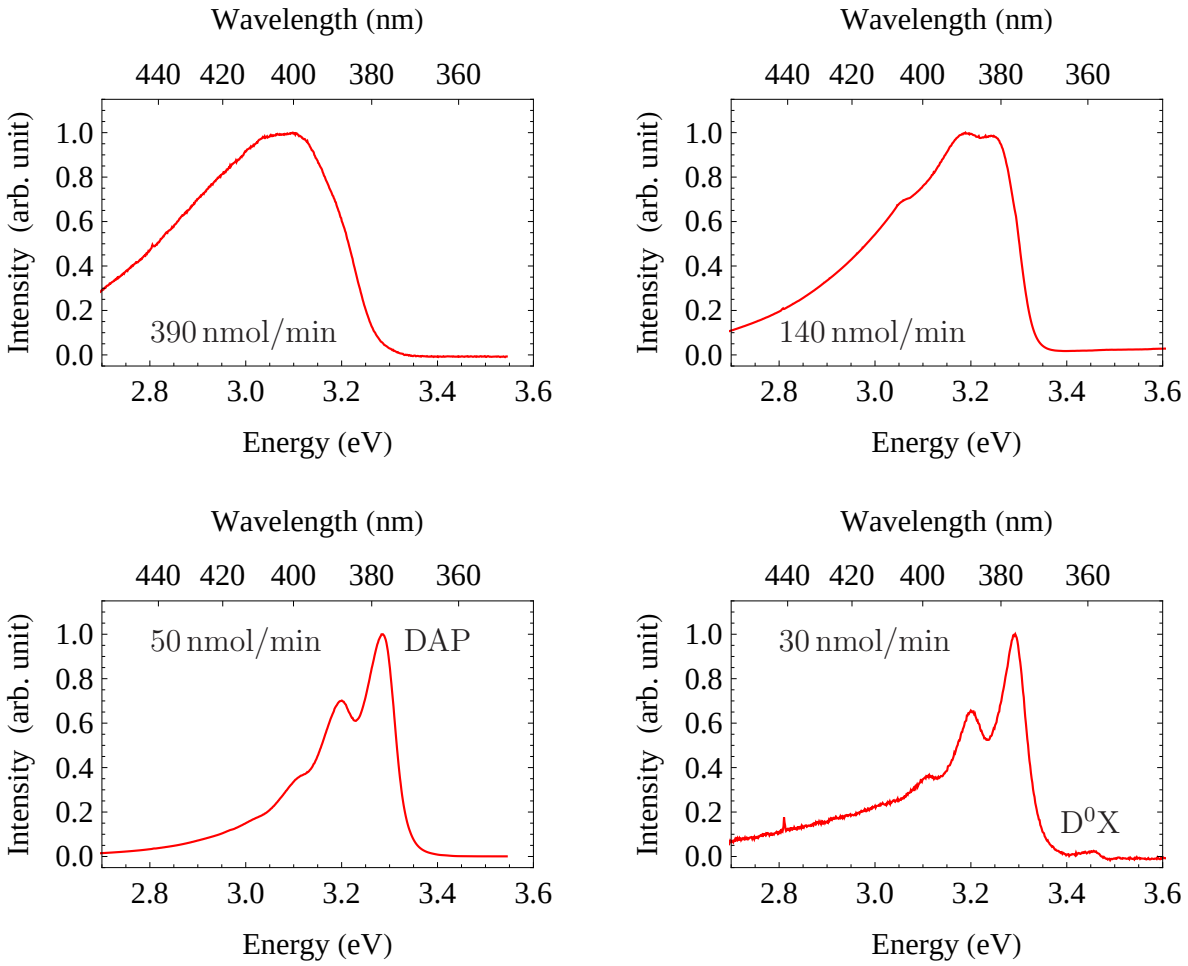

Fig. 5: Photoluminescence spectra of GaN grown with different Mg molar flows.

2.5 Semipolar InGaN/GaN-LED

After having optimized the n- and p-layers, we have integrated such layers together with InGaN/GaN-QWs to realize a semipolar LED structure. Therefore, five InGaN quantum wells (QW) with a thickness of 3 nm and 6 nm thick GaN barriers were grown on the top of an about 2 µm thick n-doped semipolar GaN layer. Between the p-doped layer and the QWs an about 30 nm thick intrinsic GaN spacer was grown in order to minimize the back-diffusion of Mg atoms into the InGaN layers. The p-layer itself has a thickness of about 100 nm. Corresponding electroluminescence (EL) measurements give a QW emission wavelength of 470 nm and an optical output power of 91 µW at a driving current of 20 mA measured with simple contact processing on the wafer (see Fig. 6, right). Thus, an optimized p-doping process and a reduced growth temperature of the layers subsequently

grown on the top of the InGaN-QWs improved the optical output power by 50 %. In Fig. 6 (left), the I-V-curve of this LED is shown. A reverse current of 5 µA at −10 V indicates a nice diode behavior of the LED. However, we observed a fairly large series resistance leading to a forward voltage of about 10 V at 20 mA. This may be a consequence of a not yet completely optimized p-doped GaN layer.

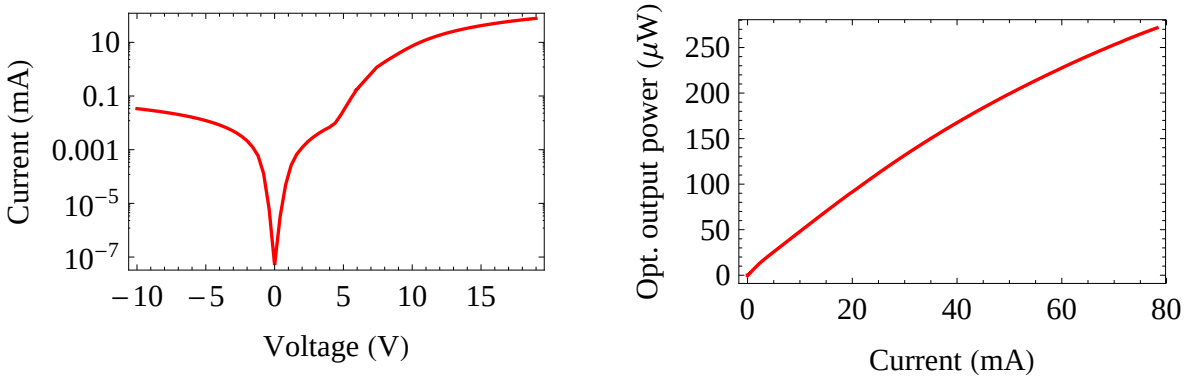

Fig. 6: Left: Voltage dependent current measurement of an InGaN/GaN LED based on the improved Mg doping process. Right: Optical output power versus drive current.

3. Conclusion

Using $(10\bar{1}2)$ patterned sapphire substrates, we were able to grow planar semipolar $(11\bar{2}2)$ GaN with a suitable crystal and surface quality. Systematic investigations of the Mg-doping behavior of $(11\bar{2}2)$-oriented GaN showed a strong temperature depended incorporation efficiency. The lower the growth temperature, the more Mg atoms were incorporated. However, in comparison to c-plane surfaces, the efficiency seems to be still significantly lower. Fortunately, a decreased growth temperature seems also to reduce the amount of parasitic background charge carriers. Choosing the optimized growth conditions, a LED with a suitable electrical and optical performance was grown. The LED shows a good diode behavior and the optical output power at a driving current of 20 mA was measured to 91 µW.

Acknowledgment

I thank Raphael Zeller and Sabine Schörner for the intensive cooperation. Furthermore, I thank Rudolf Rösch and Rainer Blood for the technical support. All the fruitful discussions with Robert Leute and Junjun Wang are gratefully acknowledged.

References

[1] J.S. Im, H. Kollmer, J. Off, A. Sohmer, F. Scholz, and A. Hangleiter, "Reduction of oscillator strength due to piezoelectric fields in GaN/$Al_xGa_{1-x}N$ quantum wells", *Phys. Rev. B*, vol. 57, pp. R9435–R9438, 1998.

[2] K. Fujito, S. Kubo, and I. Fujimura, "Development of bulk GaN crystals and nonpolar/semipolar substrates by HVPE", *MRS Bull.*, vol. 34, pp. 313–317, 2009.

[3] N. Okada, H. Oshita, K. Yamane, and K. Tadatomo, "High-quality (20-21) GaN layers on patterned sapphire substrate with wide-terrace", *Appl. Phys. Lett.*, vol. 99, pp. 242103-1–3, 2011.

[4] J. Hertkorn, F. Lipski, P. Brückner, T. Wunderer, S. Thapa, F. Scholz, A. Chuvilin, U. Kaiser, M. Beer, and J. Zweck, "Process optimization fort the effective reduction of threading dislocations in MOVPE grown GaN using in-situ deposited masks", *J. Cryst. Growth*, vol. 310, pp. 4867–4873, 2008.

[5] B. Santic, "Statistics of the Mg acceptor in GaN in the band model", *Semicond. Sci. Technol.*, vol. 21, pp. 1484–1487, 2006.

[6] S.C. Cruz, S. Keller, T.E. Mates, U.K. Mishra, and S.P. DenBaars, "Crystallographic orientation dependence of dopant and impurity incorporation in GaN films grown by metalorganic chemical vapor deposition", *J. Cryst. Growth*, vol. 311, pp. 3817–3823, 2009.

[7] U. Kaufmann, P. Schlotter, H. Obloh, K. Köhler, and M. Maier, "Hole conductivity and compensation in epitaxial GaN:Mg layers", *Phys. Rev. B*, vol. 62, pp. 10867–10872, 2000.

[8] J. Hertkorn, P. Brückner, S. Thapa, T. Wunderer, F. Scholz, M. Feneberg, K. Thonke, R. Sauer, M. Beer, and J. Zweck, "Optimization of nucleation and buffer layer growth for improved GaN quality", *J. Cryst. Growth*, vol. 308, pp. 30–36, 2007.

[9] S.R. Xu, Y. Hao, J.C. Zhang, Y.R. Cao, X.W. Zhou, L.A. Yang, X.X. Ou, K. Chen, and W. Mao, "Polar dependence of impurity incorporation and yellow luminescence in GaN films grown by metal-organic chemical vapor deposition", *J. Cryst. Growth*, vol. 312, pp. 3521–3524, 2010.

Internal Quantum Efficiency and Carrier Injection Efficiency of c-plane, $\{10\bar{1}1\}$ and $\{11\bar{2}2\}$ InGaN/GaN-Based Light Emitting Diodes

Junjun Wang

The electroluminescence (EL) output power of c-plane light emitting diodes (LEDs) is much higher than that of semipolar $\{10\bar{1}1\}$ and $\{11\bar{2}2\}$ LEDs on sapphire at the same operation current. In order to elucidate the reasons for this behavior, we have fitted the pulsed EL data by the well-known ABC model to extract the internal quantum efficiency (IQE) and the carrier injection efficiency (CIE) to clarify which parameter weighs more for the poor EL output power of the semipolar LEDs. On our semipolar LEDs, we observe a CIE of only about 4 %, whereas their c-plane counterparts show a CIE of nearly 80 %. The IQE values are fairly the same for all three structures. The fit of resonant photoluminescence (PL) data at room temperature confirms the similar IQE values for all three structures.

1. Introduction

Nowadays, InGaN/GaN based light emitting diodes (LEDs) are widely used as visible light sources ranging from blue to green. Owing to the polar character of the nitride semiconductors, the strain in InGaN/GaN quantum wells (QWs) leads to an internal electric field resulting in a local separation of electrons and holes, reducing their recombination probability and hence decreasing the InGaN/GaN QW efficiency. Consequently, many groups are making efforts to fabricate semipolar/nonpolar InGaN/GaN based LEDs following different approaches [1, 2]. Nevertheless, the luminescence efficiency of semipolar/nonpolar LEDs on foreign substrates is typically inferior as compared to that of the c-plane ones regardless of the expected higher QW efficiency. Is the lower luminescence efficiency caused by actually lower QW efficiency or worse charge carrier transport into the QWs? In this study, we try to answer this question by separating the internal quantum efficiency (IQE) and the carrier injection efficiency (CIE) through fitting of the electroluminescence (EL) data with the well-known ABC model [3] for c-plane, $\{10\bar{1}1\}$ and $\{11\bar{2}2\}$ LEDs. The IQE was additionally determined via the fit of the photoluminescence (PL) data of the same structures in order to check the reliability of the EL fit.

2. Experimental

Epitaxial growth of all three LED structures was carried out in a low pressure MOVPE horizontal reactor AIX-200/4 RF-S using TMGa, TEGa, TMIn, Cp_2Mg, SiH_4 and NH_3

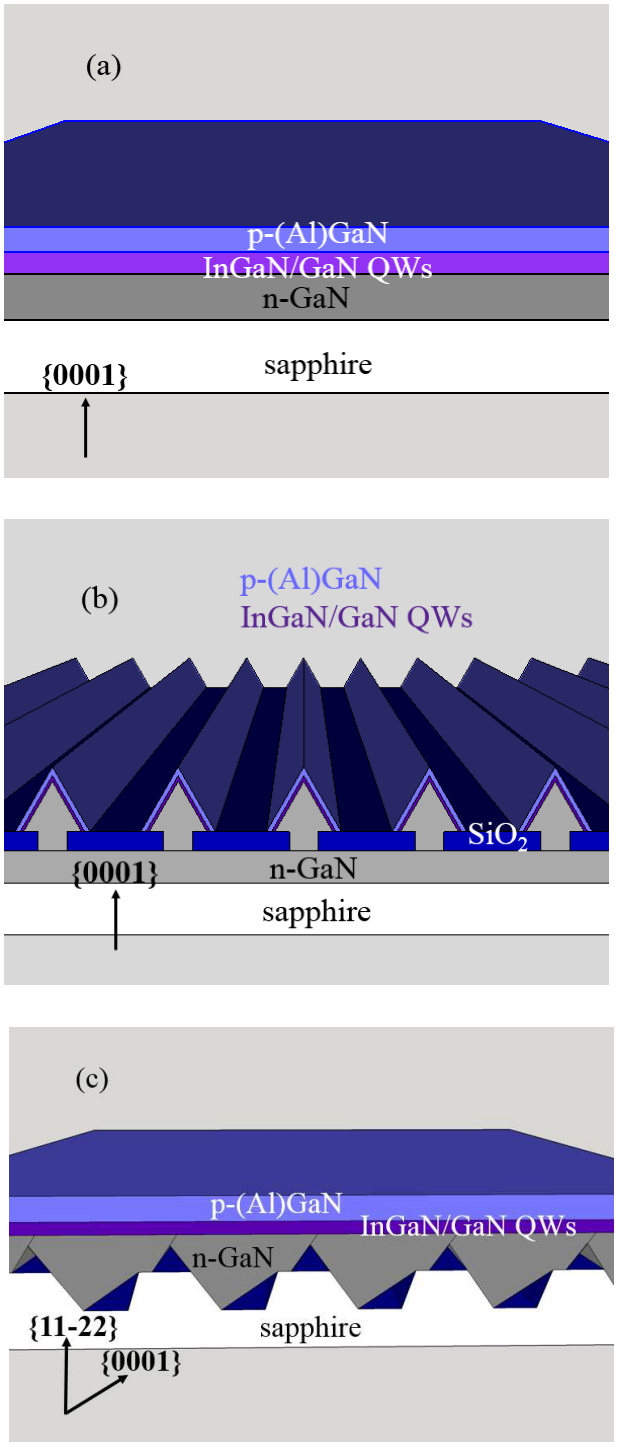

Fig. 1: Schematic structures of the c-plane (a), stripe $\{10\bar{1}1\}$ (b) and planar $\{11\bar{2}2\}$ (c) LEDs.

Table 1: The assumed values of the LEE and the calculated values of the CIE based on the fit for the c-plane LED, the stripe {10$\bar{1}$1} LED and the planar {11$\bar{2}$2} LED.

	LEE	CIE
c-plane LED	23 %	78 %
stripe {10$\bar{1}$1} LED	40 %	4 %
planar {11$\bar{2}$2} LED	40 %	4 %

as precursors. The c-plane LED was grown on a c-plane sapphire wafer consisting of 3 µm thick n-GaN employing an in-situ deposited SiN nanomask layer for defect density reduction [4], 5-fold InGaN/GaN QWs as the active region with an InGaN thickness of 2.2 nm, 200 nm thick p-GaN capped with an excessively p-doped contact layer (Fig. 1a). To fabricate the {10$\bar{1}$1} LED [5], firstly, a 3 µm thick high quality n-doped GaN layer was grown on c-plane sapphire. Then, a 200 nm thick SiO_2 layer was deposited on the GaN template by plasma enhanced chemical vapor deposition (PECVD) and patterned into periodic stripes with 10 µm wide masked area and 3 µm wide opening along the ⟨11$\bar{2}$0⟩ crystal direction via photolithography and dry etching. Finally, 3D n-doped GaN stripes with triangular cross-section and a height of about 8.5 µm were formed providing the {10$\bar{1}$1} facet for the deposition of a single InGaN/GaN QW with the InGaN thickness of 2.5 nm and the subsequent layers to form the complete LED structure (Fig. 1b). A {10$\bar{1}$2} sapphire was employed as the substrate for the {11$\bar{2}$2} LED [6–8]. Firstly, the photoresist on the sapphire substrate is patterned into parallel stripes running along the sapphire a-direction with a period of 6 µm via lithography. The stripe pattern is transferred into the sapphire substrate via reactive ion etching to achieve trenches with c-plane-like sidewalls. Then, SiO_2 is sputtered on top of all non c-plane-like facets to avoid parasitic GaN growth. Finally, the n-GaN growth starts from the c-plane-like sidewall and coalesces into a planar surface, the {11$\bar{2}$2} facet, followed by 5-fold InGaN/GaN QWs with the InGaN thickness of 4.1 nm and p-(Al)GaN layers to complete the LED structure (Fig. 1c).

The LED structures are annealed at 750 °C for 1 min in air for p-doping activation. On-wafer pulsed EL was applied with a pulse width of 1 µs and a duty cycle of 1 % to avoid diode heating at large current densities. The external quantum efficiency (EQE) as an input data for the EL fit besides the measured current density j is evaluated from the experimental data according to the following equation:

$$\mathrm{EQE} = \frac{\Phi q}{E_{\mathrm{ph}} I} \qquad \text{where} \qquad E_{\mathrm{ph}} = \frac{hc}{\lambda} \tag{1}$$

with E_{ph} representing the photon energy, Φ the radiant flux out of the LED, I the current flowing through the LED, q the elementary charge, h Planck's constant, c the speed of light in vacuum and λ the emission wavelength. The radiant flux Φ is measured in an integration sphere whereas the emission wavelength λ is obtained by a spectrometer. For the PL measurements, we employed a 405 nm laser diode as the excitation source to excite the carriers resonantly only in the QWs.

3. Fitting

According to the well-known ABC model, there are three recombination mechanisms, non-radiative Shockley-Read-Hall (SRH) recombination, radiative recombination and Auger recombination whose recombination rates are proportional to n, n^2 and n^3, respectively, with n representing the carrier concentration. Then, the IQE can be expressed as

$$\mathrm{IQE} = \frac{Bn^2}{An + Bn^2 + Cn^3}, \tag{2}$$

where A, B and C are the recombination rate coefficients.

In the case of EL, the external quantum efficiency (EQE) can be separated into three parts, CIE, IQE and light extraction efficiency (LEE):

$$\mathrm{EQE} = \mathrm{CIE} \cdot \mathrm{LEE} \cdot \mathrm{IQE}. \tag{3}$$

By inserting (2) into (3), the relation between EQE and the carrier concentration n can be written as

$$\mathrm{EQE} = \mathrm{CIE} \cdot \mathrm{LEE} \cdot \frac{Bn^2}{An + Bn^2 + Cn^3}. \tag{4}$$

In steady state, the recombination rate R is equal to the carrier injection rate G_{inj}, $R = G_{\mathrm{inj}}$.

$$R = An + Bn^2 + Cn^3, \tag{5}$$

$$G_{\mathrm{inj}} = \frac{\mathrm{CIE} \cdot I}{qV_{\mathrm{QW}}}, \tag{6}$$

where I, q and V_{QW} are the operation current, the elementary charge and the QW volume, respectively. Therefore, the relation between the current density j and the carrier concentration n can be written as

$$j \cdot \mathrm{CIE} = qd_{\mathrm{QW}} \left(An + Bn^2 + Cn^3 \right). \tag{7}$$

Multiplying (4) with (7), the carrier concentration n can be expressed by other parameters as:

$$n = \sqrt{\frac{j \cdot \mathrm{EQE}}{Bqd_{\mathrm{QW}}\mathrm{LEE}}} \tag{8}$$

Inserting (8) into (7), we obtain the relation between j and $\sqrt{j \cdot \mathrm{EQE}}$:

$$\begin{aligned} j = \frac{A}{\mathrm{CIE}}\sqrt{\frac{qd_{\mathrm{QW}}}{B \cdot \mathrm{LEE}}}\sqrt{j \cdot \mathrm{EQE}} \;&+\; \frac{1}{\mathrm{CIE} \cdot \mathrm{LEE}}\left(\sqrt{j \cdot \mathrm{EQE}}\right)^2 \\ &+\; \frac{C}{\mathrm{CIE}}\sqrt{\frac{1}{qd_{\mathrm{QW}}B^3\mathrm{LEE}^3}}\left(\sqrt{j \cdot \mathrm{EQE}}\right)^3. \end{aligned} \tag{9}$$

j is a cubic polynomial function of $\sqrt{j \cdot \mathrm{EQE}}$ with the constant term to be zero. By applying a polynomial fit to the curve of j versus $\sqrt{j \cdot \mathrm{EQE}}$, one obtains the coefficients of all terms in (9). CIE $\cdot$ LEE is determined from the coefficient of the quadratic term

and the IQE is calculated as the ratio of EQE and CIE · LEE. A good estimation of LEE for a certain structure can be achieved by Monte Carlo ray tracing. It is reported to be about 23 % for on-wafer measurements of a c-plane LED [9]. An enhanced LEE is expected for the two semipolar LEDs due to the 3D GaN surface morphology or the sapphire structurization. As a rough estimate, 40 % of LEE is assumed in this study for both structures. Therefore, the CIE is acquired as the ratio of CIE · LEE and the assumed LEE.

The fitting principle of the PL data is similar as that of the EL data. The ratio of the integrated PL intensity I_{PL} and the power of the excitation source P_{PL} is proportional to the IQE:

$$\frac{I_{\mathrm{PL}}}{P_{\mathrm{PL}}} = \eta_1 \frac{Bn^2}{An + Bn^2 + Cn^3} \tag{10}$$

with η_1 denoting an unknown constant. The carrier generation rate G is proportional to the power of the excitation source:

$$G = \eta_2 P_{\mathrm{PL}} \tag{11}$$

with η_2 denoting an other unknown constant. In steady state, the carrier generation rate is equal to the recombination rate, $G = R$. Considering (5), we get

$$\eta_2 P_{\mathrm{PL}} = An + Bn^2 + Cn^3. \tag{12}$$

Putting (10) into (12), one can derive the relation between the parameters I_{PL} and P_{PL} as:

$$P_{\mathrm{PL}} = A\sqrt{\frac{1}{B\eta_1\eta_2}}\sqrt{I_{\mathrm{PL}}} + \frac{1}{\eta_1}\left(\sqrt{I_{\mathrm{PL}}}\right)^2 + C\sqrt{\frac{\eta_2}{B^3{\eta_1}^3}}\left(\sqrt{I_{\mathrm{PL}}}\right)^3 \tag{13}$$

P_{PL} is a cubic polynomial function of $\sqrt{I_{\mathrm{PL}}}$ with the constant term to be zero. By applying again a polynomial fit to the curve of P_{PL} versus $\sqrt{I_{\mathrm{PL}}}$, one obtains the value of $1/\eta_1$ as the coefficient of the quadratic term with which the absolute value of the IQE can be calculated according to (10).

4. Results

The c-plane LED, the stripe {10$\bar{1}$1} LED and the planar {11$\bar{2}$2} LED emit at 435 nm, 430 nm and 428 nm, respectively. As seen in Fig. 2, the c-plane LED has much higher output power in pulsed EL than the two semipolar ones. The fitting method is applied to all three structures to analyze whether the lower luminescence efficiency of the semipolar LEDs on foreign substrates is caused by lower CIE or lower IQE.

For the simple c-plane LED, a tight fit was obtained for the EQE curve (Fig. 3, left). CIE · LEE is determined to be 0.18 as the reverse value of the coefficient of the quadratic term in (9). Thus, the CIE is calculated to be 78 % with the assumed LEE of 23 % (Table 1). Similar IQE data versus current density have been measured on a sister wafer by T. Meyer in the characterization labs of Osram OS (Regensburg) [10] nicely confirming our

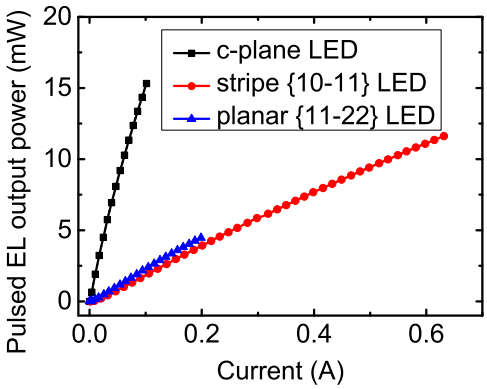

Fig. 2: The output power against the current of pulsed EL for c-plane LED, stripe $\{10\bar{1}1\}$ LED and planar $\{11\bar{2}2\}$ LED.

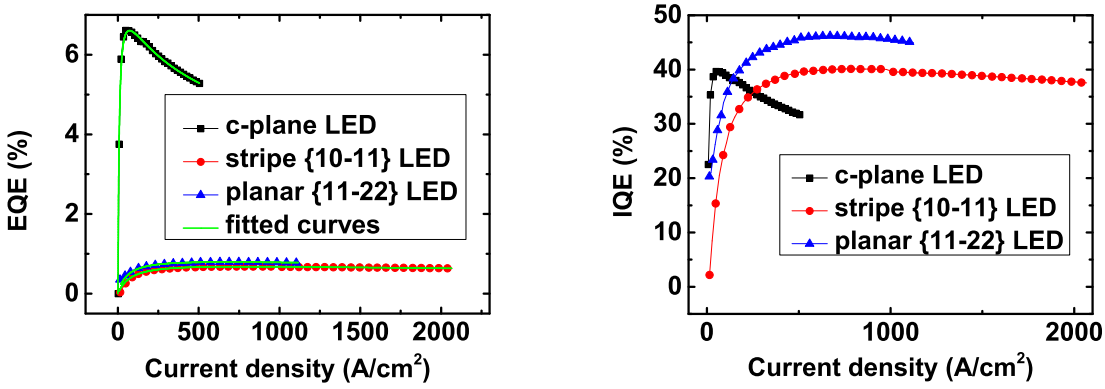

Fig. 3: EQE (left) and IQE (right) at different current density for the c-plane LED, the stripe $\{10\bar{1}1\}$ LED and the planar $\{11\bar{2}2\}$ LED.

evaluation method. From those results, we estimate a maximum error range of our IQE value of about 30 %.

Tight fits were obtained for the EQE curves of the two semipolar structures as well. CIE · LEE is determined to be 1.7 % and 1.7 % for the stripe {10$\bar{1}$1} LED and the planar {11$\bar{2}$2} LED, respectively. The corresponding CIE values are 4 % and 4 %, calculated with the assumed LEE values for the different structures (Table 1). Surprisingly, the CIE of the semipolar LEDs is much lower than 78 % of the c-plane LEDs! As seen in Fig. 3, both, the EQE and the IQE raise fast and start to decrease at a smaller current density for the c-plane LED as compared to the semipolar ones. The IQE of the semipolar LEDs is lower than that of the c-plane LED at low current density, but is similar and even higher at high current density. This can not explain the much higher EQE of the c-plane LED at all current densities. Obviously, the poor carrier injection is responsible for the not satisfying performance of the semipolar LEDs rather than the spectra and hence the crystal quality the InGaN/GaN QWs.

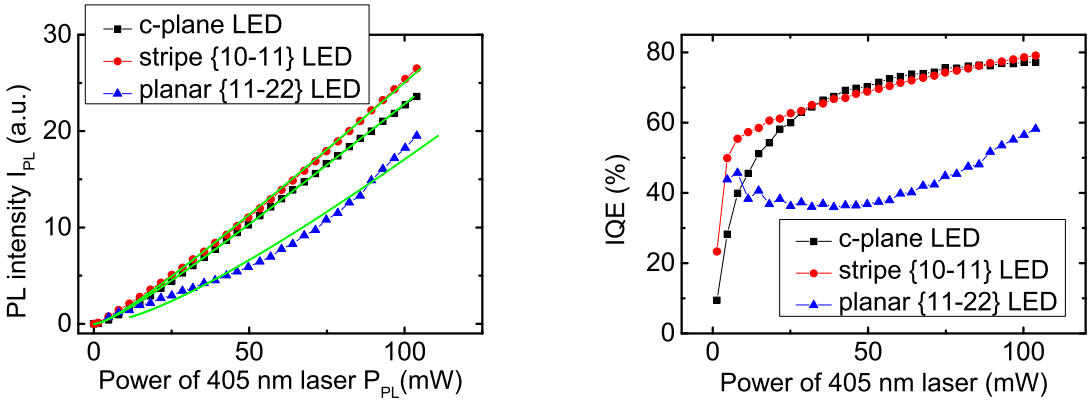

Fig. 4: The PL intensity I_{PL} dependent on the excitation power P_{PL} with the corresponding fitted curves (left) and the IQE estimated by the fit of the PL data (right) for the c-plane LED, the stripe {10$\bar{1}$1} LED and the planar {11$\bar{2}$2} LED.

For the PL measurements, the excitation power P_{PL} was varied from 1.4 mW to 104 mW by varying the driving current of the 405 nm laser diode. A stripe {10$\bar{1}$1} structure with 5-fold InGaN/GaN QWs is employed in the PL measurement since the PL spectrum of the one with the single QW is so weak that it is covered by the spectral tail of the 405 nm laser diode. The quantum efficiency keeps increasing with increasing excitation power since the 405 nm laser diode does not have sufficient power to reach the high carrier concentration where the Auger recombination is expected to dominate. Therefore, the cubic term in (13) is skipped for the fit of the PL data. Reasonable fits were obtained for all three structures (Fig. 4, left). The lack of the data points over a sufficient large range of the carrier concentration would increase the error of the fitting. Nevertheless, the PL fit results in fairly the same IQE values for the c-plane and the stripe {10$\bar{1}$1} LEDs and a slightly lower IQE value for the planar {11$\bar{2}$2} LED (Fig. 4, right). The 35 % lower IQE of the planar {11$\bar{2}$2} LED is definitely not the root reason for its inferior EL performance taking the big difference of the EL output power between the c-plane LED and the semipolar ones into account.

As indicated by the fits of the EL and PL data, the poor CIE rather than the IQE is the root reason for the low EQE of the semipolar LEDs. Therefore, it would be essential to improve the carrier transport or suppress the carrier leakage to achieve brighter semipolar LEDs. This may require to improve the electrical properties of the p-(Al)GaN layers, the p-doping profile or to optimize the AlGaN electron blocking layer and to eliminate any carrier tunneling channels, e.g., stacking faults intersecting the semipolar QWs [11].

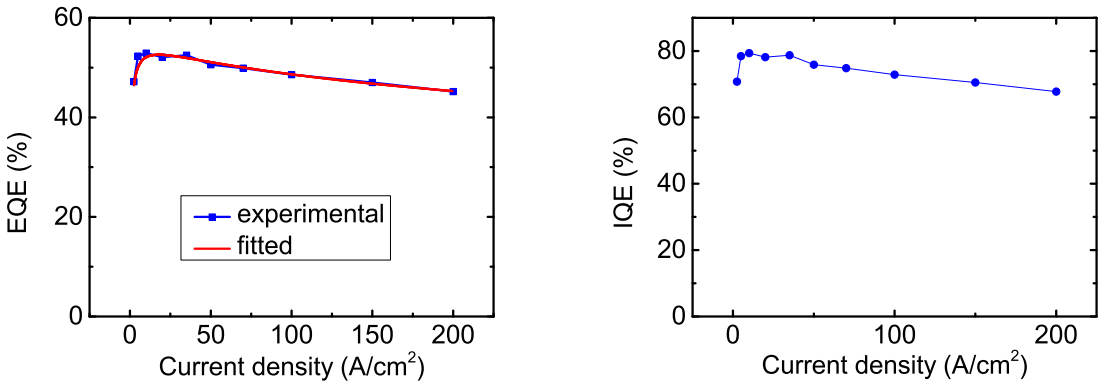

Fig. 5: The EQE curve according to the pulsed EL data and its fit (left) and the IQE curve determined by the fitting (right) dependent on the current density for the $\{20\bar{2}\bar{1}\}$ LED on the native GaN substrate.

Is the low CIE an intrinsic problem of the semipolar GaN? To answer this question, we notice that UCSB reported a high-efficient semipolar $\{20\bar{2}\bar{1}\}$ LED grown on native GaN substrates [12]. The ABC model is able to fit the pulsed EL data with a duty cycle of 1 % very well (Fig. 5, left). CIE · LEE was determined to be 68 % leading to CIE > 68 %. Hence, this LED does not suffer from the poor carrier injection. The estimated IQE reaches its maximum of ∼ 80 % at the current density of 10 A/cm^2 (Fig. 5, right). We see that the poor carrier injection limits the performance of the semipolar LED on the foreign substrate rather than that on the GaN native substrate.

The poor CIE rather than the IQE is the root reason for the low EQE of the semipolar LEDs on foreign substrates indicating that it would be essential to improve the carrier transport or suppress the electron spill-over to achieve brighter semipolar LEDs. Correspondingly, to improve the electrical property of p-(Al)GaN layers, p-doping profile or to optimize the AlGaN electron blocking layer could be good possibilities.

5. Summary

Pulsed EL measurements with a duty cycle of 1 % were applied to c-plane, $\{10\bar{1}1\}$ and $\{11\bar{2}2\}$ LEDs to avoid diode heating. The fit of the pulsed EL data according to the ABC model allows us to obtain the IQE and CIE values. The IQE is comparable for all three structures whereas the CIE is determined to be 78 % for the c-plane LED, but only about 4 % for its semipolar counterparts. IQE values obtained by fitting resonant PL data confirm these findings. Hence, a poor charge carrier injection is responsible for

the lower efficiency of our semipolar LEDs grown on foreign substrates as compared to c-plane LEDs.

Acknowledgment

The authors gratefully acknowledge the discussion with Dario Schiavon (now with TopGaN Lasers), the IQE measurement by Tobias Meyer (OSRAM), the technical support from M. Alimoradi-Jazi and R.F. Gul. This work has been financially supported by the German Federal Ministry of Education and Research (BMBF) in the project Hi-Q-LED (FKZ 13N9977).

References

[1] K. Fujito, K. Kiyomi, T. Mochizuki, H. Oota, H. Namita, S. Nagao, and I. Fujimura, "High-quality nonpolar m-plane GaN substrates grown by HVPE", *Phys. Status Solidi A*, vol. 5, pp. 1056–1059, 2008.

[2] F. Scholz, "Semipolar GaN grown on foreign substrates: a review", *Semicond. Sci. Technol.*, vol. 27, pp. 024002-1–15, 2012.

[3] Q. Dai, M.F. Schubert, M.H. Kim, J.K. Kim, E.F. Schubert, D.D. Koleske, M.H. Crawford, S.R. Lee, A.J. Fischer, G. Thaler, and M.A. Banas, "Internal quantum efficiency and nonradiative recombination coefficient of GaInN/GaN multiple quantum wells with different dislocation densities", *Appl. Phys. Lett.*, vol. 94, pp. 111109-1–3, 2009.

[4] J. Hertkorn, F. Lipski, P. Brückner, T. Wunderer, S.B. Thapa, F. Scholz, A. Chuvilin, U. Kaiser, M. Beer, and J. Zweck, "Process optimization for the effective reduction of threading dislocations in MOVPE grown GaN using in situ deposited SiN_x masks", *J. Cryst. Growth*, vol. 310, pp. 4867–4870, 2008.

[5] T. Wunderer, P. Brückner, B. Neubert, F. Scholz, M. Feneberg, F. Lipski, M. Schirra, and K. Thonke, "Bright semipolar GaInN/GaN blue light emitting diode on side facets of selectively grown GaN stripes", *Appl. Phys. Lett.*, vol. 89, pp. 041121-1–3, 2006.

[6] F. Scholz, T. Meisch, M. Caliebe, S. Schörner, K. Thonke, L. Kirste, S. Bauer, S. Lazarev, and T. Baumbach, "Growth and doping of semipolar GaN grown on patterned sapphire substrates", *J. Cryst. Growth*, vol. 405, pp. 97–101, 2014.

[7] N. Okada, A. Kurisu, K. Murakami, and K. Tadatomo, "Growth of semipolar (11$\bar{2}$2) GaN layer by controlling anisotropic growth rates in r-plane patterned sapphire substrate", *Appl. Phys. Express*, vol. 2, pp. 091001-1–3, 2009.

[8] N. Okada, K. Uchida, S. Miyoshi, and K. Tadatomo, "Green light-emitting diodes fabricated on semipolar (11$\bar{2}$2) GaN on r-plane patterned sapphire substrate", *Phys. Status Solidi A*, vol. 209, pp. 469–472, 2012.

[9] T.X. Lee, K.F. Gao, W.T. Chien, and C.C. Sun, "Light extraction analysis of GaN-based light-emitting diodes with surface texture and/or patterned substrate", *Optics Express*, vol. 15, pp. 6670–6676, 2007.

[10] T. Meyer, OSRAM OS, *Private Communication*, Nov. 2014.

[11] S. Faraji, "Epitaxy and characterization of semi-polar $(10\bar{1}1)$ and $(20\bar{2}1)$ GaN-based hetero-structures on $(11\bar{2}3)$ and $(22\bar{4}3)$ patterned sapphire substrate", Master Thesis, Inst. of Optoelectronics, Ulm University, 2015.

[12] Y. Zhao, S. Tanaka, C.C. Pan, K. Fujito, D. Feezell, J.S. Speck, S.P. DenBaars, and S. Nakamura, "High-power blue-violet semipolar $(20\bar{2}\bar{1})$ InGaN/GaN light-emitting diodes with low efficiency droop at 200 A/cm^2", *Appl. Phys. Express*, vol. 4, pp. 082104-1–3, 2011.

Selective Area Epitaxy of GaN Stripes With Sub-200 nm Periodicity

Robert A. R. Leute

We present growth studies on gallium nitride (GaN) stripes with $\{10\bar{1}1\}$ *side facets grown on c-oriented GaN templates on sapphire. Via plasma enhanced chemical vapor deposition (PECVD), a 20 nm thick* SiO_2 *mask is deposited on top of the templates. Afterwards, a polymethylmethacrylate (PMMA) based resist is patterned with stripes oriented along the GaN a-direction by electron beam (e-beam) lithography. The stripes have a periodicity below 200 nm. The pattern is transferred via fluorine based dry-etching with an inductively coupled plasma (ICP) reactive ion etching (RIE) process. Any remaining resist is removed with oxygen plasma and the samples are cleaned before epitaxy. The influence of e-beam parameters, etching rates, etching agents and etching times on the pattern transfer and subsequent overgrowth is investigated. Semipolar InGaN/GaN quantum wells are deposited on the side facets of the nanostripes.*

1. Introduction

Selective area epitaxy (SAE) of GaN works very well for defect reduction [1, 2]. Even more, by aptly choosing mask patterns and growth conditions, three-dimensional GaN structures — rods, stripes, pyramids — with a high surface to volume ratio as well as non- or semipolar surface facets can be fabricated. These semipolar surface facets on c-oriented templates have great potential for cost-effective light emitters in the green wavelength regime [3]. Reducing them in size allows embedding, resulting in a flat sample surface which enables conventional device processing [4]. Furthermore, the sub-µm sized structures create new potential applications like photonic crystal emitters [5]. For the latter, the periodicity of the GaN nanostructures has to be in the range of the intended emission wavelength. For high refractive index materials, like GaN, periods below 200 nm are necessary for short wavelength emitters. Thus, optical lithography can no longer be used for patterning. Experimentally, the limits of this miniaturization are given by the precision of our growth mask patterning, setting very high requirements for the process control of lithography, dry and wet etching, as well as mask deposition and epitaxy.

2. Experimental

The GaN templates were grown with a horizontal metal organic vapor phase epitaxy (MOVPE) reactor with standard precursors TMAl, TMGa, and high purity ammonia. Purified nitrogen and hydrogen are used as carrier gases. The templates consist of 2 µm

unintentionally doped GaN with an oxygen doped nucleation layer [6] on c-oriented sapphire templates. Then, a 20 nm thin layer of SiO_2 is deposited via PECVD and the samples are cleaned with acetone and isopropanol before lithography. For lithography, the samples are coated with a PMMA based resist before a conductive layer of germanium is deposited for better resolution. The electron beam patterning is performed with a Leica EBPG 5 HR. Afterwards, the Ge is removed and the resist is developed. For pattern transfer into the SiO_2 mask, a dry etching process inside an ICP RIE system with a mixed oxygen and carbon tetrafluoride plasma is used. Any remaining resist is removed with a pure O_2 plasma before the samples are either dipped into buffered hydrofluoric acid (HF) or cleaned with sulphuric acid and an aqueous KOH solution. The second epitaxial step to grow the GaN nanostripes uses the additional precursors TEGa and TMIn. The resulting nanostructures are investigated by scanning electron microscopy and photoluminescence (PL) spectroscopy.

3. Electron Beam Lithography Patterning With Sub-200 nm Periodicity

We choose a periodicity of 170 nm, which relates to the wavelength of a violet-blue light emitter inside GaN. The trench openings are intended to be below 100 nm in width to achieve a filling factor of approximately 1:1. There are several aspects to consider for such an undertaking. In the dimension perpendicular to the trenches, the resolution needs to be extremely high, requiring a very small and well focussed electron beam and a very thin resist. Furthermore, the distance between adjacent trenches is equally small, causing proximity effects of scattered electrons and increasing the unintended exposure of the resist between trenches [7, 8]. The length of the trenches, however, is intended to be at least in the milimeter range, with the ultimate goal of running over the whole wafer. This comes with an additional challenge. Previous studies with resist patterns structured by laser interference lithography (LIL) [9] have shown that any irregularities of the patterned mask, like swaying or frayed edges, directly result in inhomogeneities of the nanostripes and the quantum wells (QWs) deposited thereupon. Homogeneous QWs require highly regular masks [10]. Concerning the electron beam lithography, this results in the need for a quasi continuous exposure along the trenches, vastly aggravating the aforementioned proximity effect. Figure 1 illustrates these challenges. Optimal settings, giving results shown in Fig. 1e), were found to be 50 kV acceleration voltage, 280 pA electron current, 500 µC dosis and an aperture of 400.

4. Selective Area Epitaxy With Sub-200 nm Periodicity

In a first approach, growth conditions were based on the epitaxy of GaN nanostripes with 250 nm period, described in [11]. First, TMGa with a molar flow of 86 µmol per minute is used to grow a pure GaN stripe with $\{10\bar{1}1\}$ side facets. Then, an InGaN layer with $\approx 5\,\%$ indium is deposited to act as pre-well before a single QW with GaN barriers, followed by a thin GaN cap is grown. However, several specific aspects have to be taken into account for the sub-200 nm stripe masks patterned with electron beam

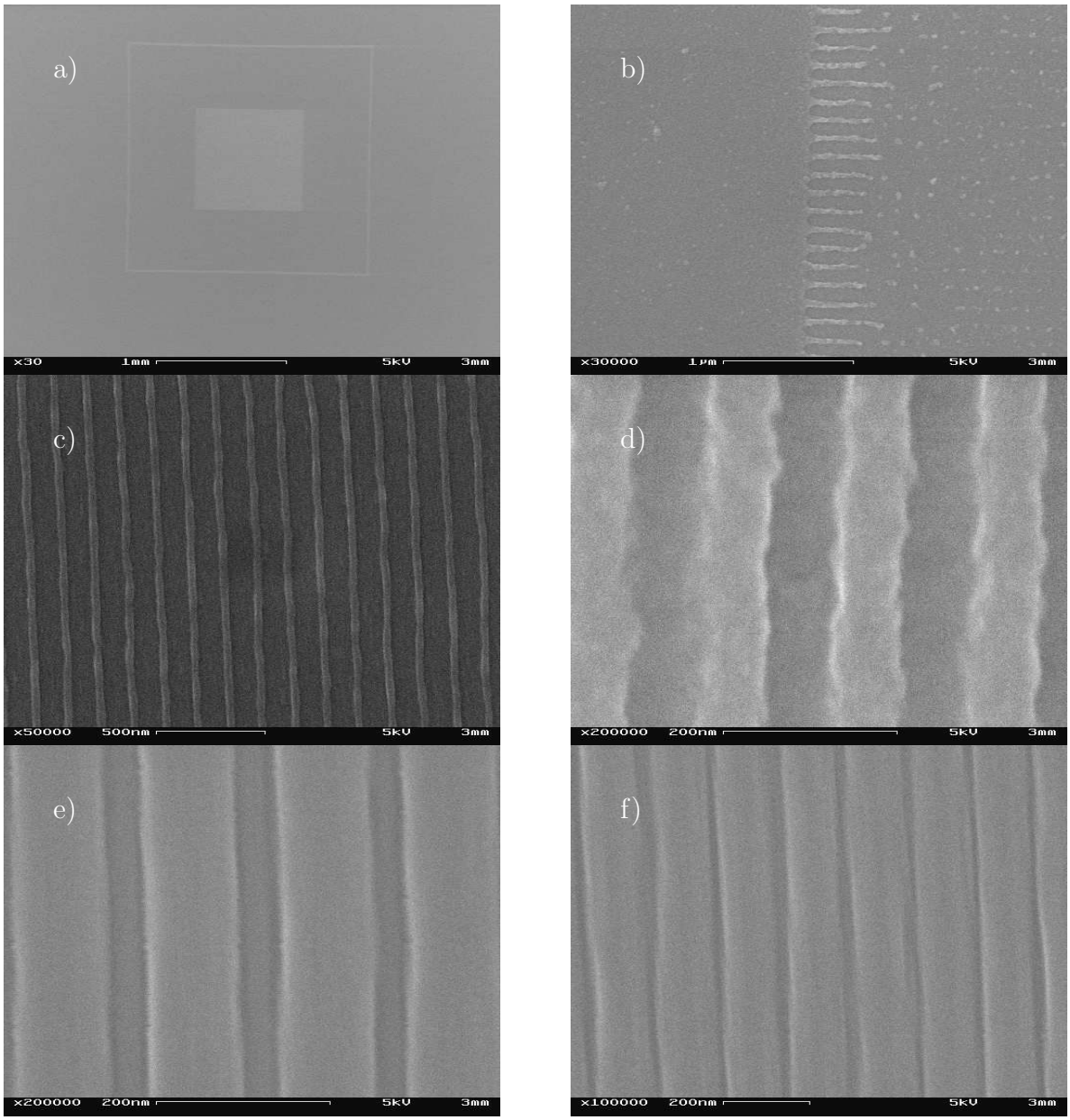

Fig. 1: Optimization steps concerning the e-beam lithography. The overall area is 0.64 mm^2 (a), the proximity of adjacent lines easily leads to overexposure (b), reducing the exposure leads to resist trenches (c), the point by point exposure causes warped, uneven edges (d), reducing the spot size and increasing the number of exposures to have a quasi continuous exposure gives the optimal result with straight lines which have even edges (e), too low exposure results in narrow trenches with remaining resist at the bottom of the trenches (f).

lithography. A good crystalline quality of the QWs depends on the stripes remaining separate [9] with coaelescence occuring after the QW growth. With the period being reduced by approximately one third, non-embedded (open) nanostripes need one third less growth time or growth rate, as compared to their 250 nm period counterparts. For samples structured via e-beam lithography, however, the area of growth is surrounded

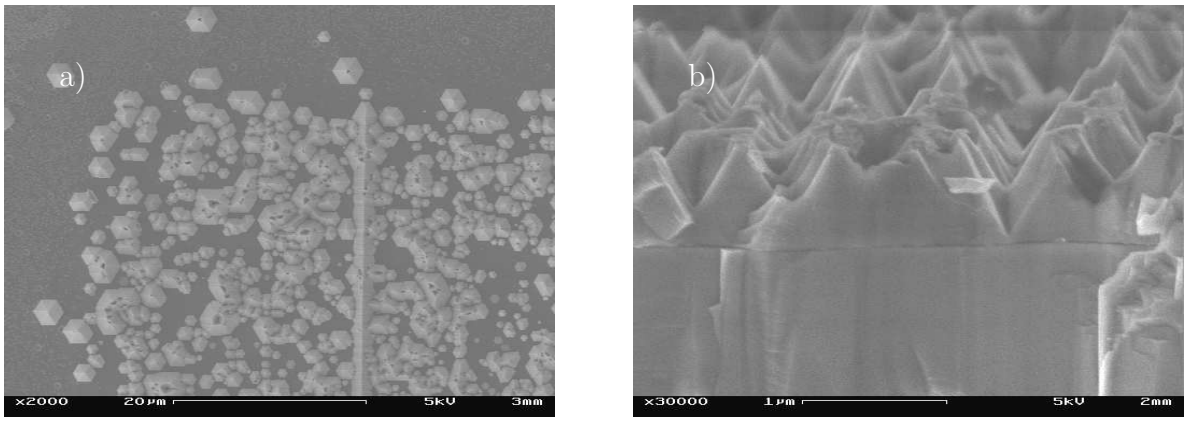

Fig. 2: SAE on templates patterned by electron beam lithography. Insuffcient homogeneity of the trench openings results in chaotic nucleation (a). Even with open trenches, a too high growth rate leads to the merging of neighboring stripes and the regular arrangement with 170 nm period is lost (b).

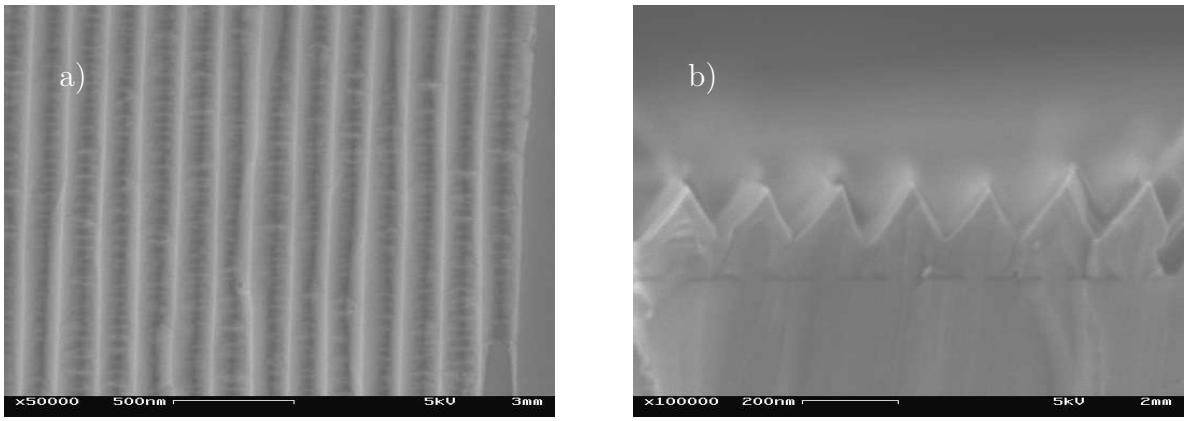

Fig. 3: Using extremely low material supply, homogeneous nanostripes could be realized. Top view shows slight deviations (a). In cross-section view, the homogenous size of the stripes and remarkably narrow ridges can be observed (b).

by vast masked areas where no growth occurs. Precursors diffuse from the completely masked area to the area where the mask is partly open [12], thereby immensely increasing the growth rate. Furthermore, it is critical to achieve homogeneously opened trenches by careful etching of the SiO_2 and sufficient exposure/development of the resist. Otherwise, nucleation will happen randomly. As soon as clusters are generated, stripe growth is no longer possible. More information on the effects of partly patterned masks can be found in [13]. Figure 2 shows the effects of inhomogenious trench openings and too high growth rate. The growth rate was drastically reduced — equivalent to $\approx 1\,\mathrm{nm/min}$ for unmasked templates — by using only TEGa instead of TMGa for the GaN growth and we were able to produce GaN nanostripes with QWs on semipolar $\{10\bar{1}1\}$ side facets on most of the patterned area, see Fig. 3. The top view reveals slight deviations, especially at the regions of beginning coalescence. The ridges are extremely sharp, well below 10 nm in width. Cross-section images reveal a mask opening of 50 nm and that the mask has been

overgrown by 60 nm. The exact position of the QWs is not visible and would necessitate transmission electron microscopy measurements.

4.1 Quantum well luminescence

For this first successful experiment, the QW emission is detuned from its intended blue wavelength. Figure 4 shows the PL spectrum recorded at 300 K. The sample was excited with a HeCd laser emitting at 325 nm, the spectrum was recorded with a monochromator with 300 lines/mm grating and an electrically cooled charge-coupled device (CCD). The excitation spot has a diameter of $\approx 100\,\mu m$, so it averages over a relatively large area, compared to the stripes dimensions. The overall emission is broad but bright and exhibits several sharp resonances which can be attributed to guided modes being extracted due to the growth mask acting as photonic crystal [5].

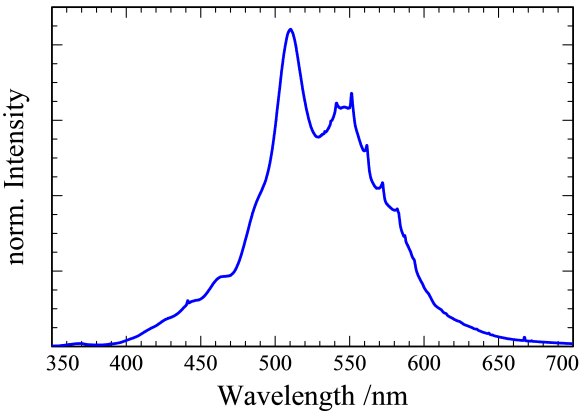

Fig. 4: PL spectrum taken at 300 K. The QW emits at 520 nm. At longer wavelengths, we observe sharp resonances related to the growth mask acting as photonic crystal.

5. Conclusion

Considerable optimization resulted in the realization of regular and homogeneous resist stripes with periodicities of 170 nm and a trench width below 100 nm. These patterns could be transferred to 20 nm thin SiO_2 layers acting as growth mask for SAE. InGaN/GaN nanostripes with triangular cross-sections and semipolar $\{10\bar{1}1\}$ side facets were presented and show QW luminescence, proving that sub-200 nm periodic GaN nanostripes for photonic crystal LEDs and distributed feedback laser diodes are feasible.

Acknowledgment

I gratefully acknowledge support from the following persons: D. Heinz and T. Meisch (epitaxy), T. Zwosta, P. Muralidhar and O. Rettig (processing), S. Jenisch (e-beam lithography), S. Saaslam (PL), S. Strehle, K. Thonke and F. Scholz (scientific support). I thank the DFG for financial support within the research group FOR957 PolarCoN.

References

[1] T.S. Zheleva, O.H. Nam, M.D. Bremser, and R.F. Davis, "Dislocation density reduction via lateral epitaxy in selectively grown GaN structures", *Appl. Phys. Lett.*, vol. 71, pp. 2472–2474, 1997.

[2] O.H. Nam, M.D. Bremser, T.S. Zheleva, and R.F. Davis, "Lateral epitaxy of low defect density GaN layers via organometallic vapor phase epitaxy", *Appl. Phys. Lett.*, vol. 71, pp. 2638–2640, 1997.

[3] F. Scholz, "Semipolar GaN grown on foreign substrates: a review", *Semicond. Sci. Technol.*, vol. 27, pp. 024002-1–15, 2012.

[4] R.A.R. Leute, D. Heinz, J. Wang, F. Lipski, T. Meisch, K. Thonke, J. Thalmair, J. Zweck, and F. Scholz, "GaN based LEDs with semipolar QWs employing embedded sub-micrometer sized selectively grown 3D structures", *J. Cryst. Growth*, vol. 370, pp. 101–104, 2013.

[5] D. Heinz, R.A.R. Leute, S. Kizir, Y. Li, T. Meisch, K. Thonke, and F. Scholz, "Ga(In)N photonic crystal light emitters with semipolar quantum wells", *Jpn. J. Appl. Phys.*, vol. 52, pp. 062101-1–5, 2013.

[6] B. Kuhn and F. Scholz, "An oxygen doped nucleation layer for the growth of high optical quality GaN on sapphire", *Phys. Status Solidi A*, vol. 188, pp. 629–633, 2001.

[7] T.H.P. Chang, "Proximity effect in electron-beam lithography", *J. Vac. Sci. Technol.*, vol. 12, pp. 1271–1275, 1975.

[8] M. Parikh, "Corrections to proximity effects in electron beam lithography. I. Theory", *J. Appl. Phys.*, vol. 50, pp. 4371–4377, 1979.

[9] R.A.R. Leute, "Optimization of GaN based light emitters with semipolar quantum wells and sub-µm patterning within the active zone", *Annual Report 2012*, pp. 69–74, Ulm University, Institute of Optoelectronics.

[10] R.A.R. Leute, J. Wang, T. Meisch, J. Biskupek, U. Kaiser, and F. Scholz, "Blue to true green LEDs with semipolar quantum wells based on GaN nanostripes", *Phys. Status Solidi C*, 2014, DOI: 10.1002/pssc.201400176.

[11] R.A.R. Leute, "Galliumnitride nanostripes with semipolar quantum wells for LED and laser applications", *Annual Report 2013*, pp. 51–56, Ulm University, Institute of Optoelectronics.

[12] M.A. Alam, R. People, E. Isaacs, C.Y. Kim, K. Evans-Lutterodt, T. Siegrist, T.L. Pernell, J. Vandenberg, S.K. Sputz, S.N.G. Chu, D.V. Lang, L. Smith, and M.S. Hybertsen, "Simulation and characterization of the selective area growth process", *Appl. Phys. Lett.*, vol. 74, pp. 2617–2619, 1999.

[13] O. Rettig, "Nitridische Nanosäulen – Design und Wachstum für Sensoranwendungen", Master Thesis, Ulm University, Ulm, Germany, 2014.

True-Green Photonic Crystal LED With Semipolar Quantum Wells Based on Embedded GaN Nanostripes: Polarized and Directional Light Emission

Robert A. R. Leute

A bottom-up approach for photonic crystal emitters and LEDs with semipolar quantum wells on large foreign substrates is presented. Structured c-oriented GaN/AlGaN templates are overgrown with GaN nanostripes and semipolar QWs emitting in the true-green spectral region. After embedding, the stripes and the growth mask act as one-dimensional (1D) photonic crystal. Electroluminescence shows bright green emission. The photonic crystal dispersion relation is simulated and confirmed by angle-resolved spectroscopy, structural analysis is performed by transmission electron microscopy.

1. Introduction

Nitride based light emitting diodes (LEDs) are widely used for lighting and display applications. Especially for the latter application, tailored emission properties, like long wavelength, degree of polarization and directionality are of high interest [1]. Nanostructuring methods allow us to influence both epitaxial growth and the optical properties of our material. The selective epitaxy on a nanoscale allows the embedding of semipolar quantum wells (QWs) with their distinct polarization properties [2] within c-oriented layers [3] while submicrometer periodicities of dielectrics create a photonic crystal (PhC) [4,5] and manipulate the light extraction. Reported PhC LEDs based on InGaN/GaN quantum wells [6, 7] typically use a top-down approach, etching holes into the semiconductor material. We employ a patterned dielectric mask in a dual use as both growth mask and PhC.

2. Experimental

All epitaxial growth takes place inside an Aixtron-200/4RF-S HT metal organic vapor phase epitaxy (MOVPE) reactor with standard precursors TMAl, TMGa, TMIn and high purity ammonia. Silane and Cp_2Mg are used for n- and p-doping, respectively. Firstly, c-oriented GaN/AlGaN templates are grown on 2-inch sapphire substrates. An oxygen doped AlN nucleation layer [8] and an *in-situ* SiN_x nanomask [9] are used for defect reduction. An AlGaN layer of 0.4 µm thickness is used as lower waveguide cladding. 20 nm SiO_2 are deposited via plasma enhanced chemical vapor deposition (PECVD) and

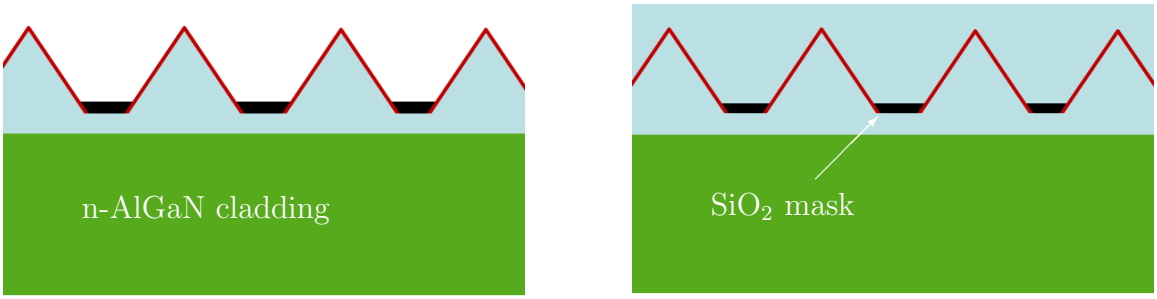

Fig. 1: Schematic drawing of a cross-section of our samples. Nanostripes with semipolar QWs are grown by selective epitaxy (left). After embedding, both QWs and the growth mask acting as 1D PhC are completely buried and the sample has a planar surface (right).

patterned into stripes aligned parallel to GaN a-direction by hot embossing nanoimprint lithography and dry etching with SF_6 plasma. The patterned SiO_2 acts both as 1D PhC and growth mask. GaN nanonstripes are grown by selective epitaxy, including an InGaN prewell. A single QW with 20% indium is deposited on the $\{10\bar{1}1\}$ side facets. After an undoped spacer, the structure is planarized with Mg-doped GaN; exact growth conditions are found in [10]. A schematic of the structure is given in Fig. 1. After growth, the samples are annealed in ambient atmosphere at 750°C for one minute to activate the Mg acceptors. For electrical characterization, 1 µm thick circular indium contacts are evaporated on the surface. Optical output power is measured on-wafer inside an integrating sphere. No additional light extraction methods besides the built-in photonic crystal were used. Angle-resolved photoluminescence (ARPL) spectra are recorded with a TRIAX monochromator and a liquid-nitrogen-cooled charge-coupled device (CCD) at the Institute of Quantum Matter by F. Huber of the Semiconductor Physics Group. The dispersion relation and other modal properties of the PhC are calculated using finite-difference-time-domain (FDTD) simulations [11] using a wavelength dependent dielectric function based on a Lorentz oscillator model; details are found in [12]. The PhC LED structures were investigated by J. Biskupek from the Central Facility of Electron Microscopy via transmission electron microscopy (TEM) after preparation of cross-section TEM samples. Conventional bright- and dark-field TEM experiments for analysis of the crystal structure of the LEDs were carried out using a Philips CM20 operating at 200 kV.

3. Results

3.1 Electroluminescence

The LED shows stable emission, centered at 535 nm, under continuous-wave operation up to 100 mA. Figure 2 shows the power-current-voltage characteristics of the device. Spectra show a broad emission with characteristic modulations, as can be seen in Fig. 3 which will be discussed in subsequent sections.

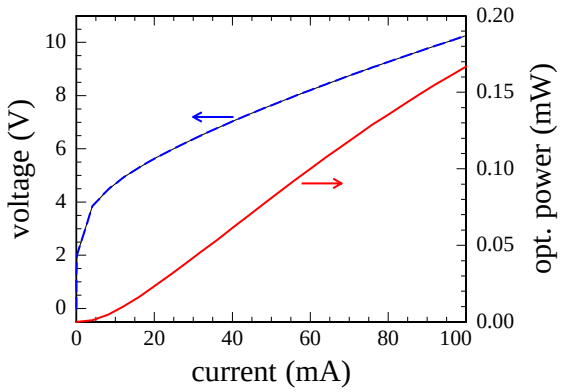

Fig. 2: Voltage-light-current characteristics of the photonic crystal LED.

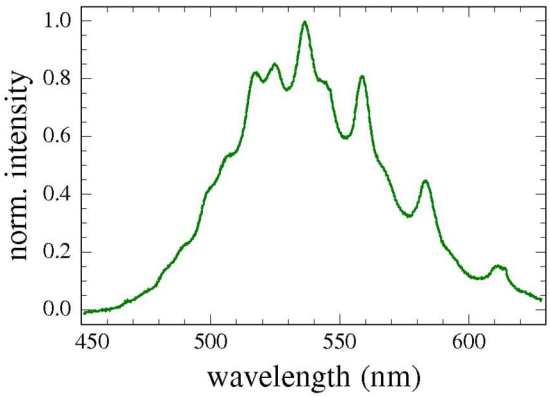

Fig. 3: Electroluminescence spectrum taken at 30 mA. The periodic modulation is caused by the built-in PhC.

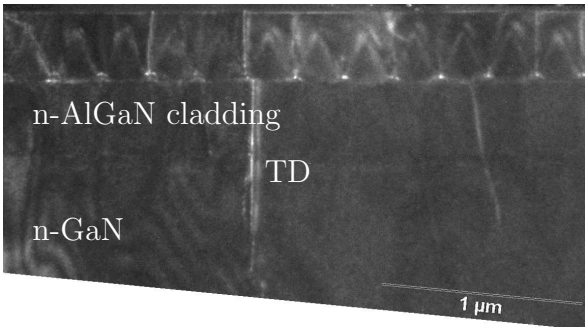

Fig. 4: Weak-beam dark-field TEM image. Few dislocations thread from the sapphire-GaN interface. Some dislocations are created at the coalescence point of the nanostripes.

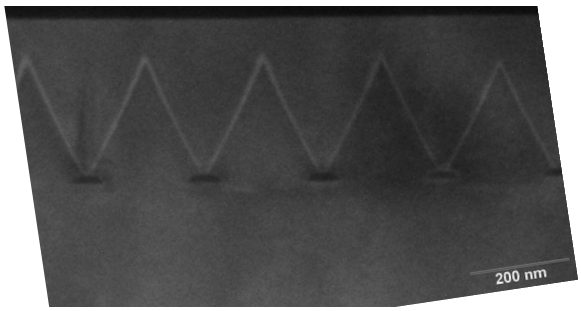

Fig. 5: HACDF image with high Z-contrast. The semipolar QWs show excellent quality and homogeneity despite high indium content.

3.2 Structural analysis

Weak-beam dark-field TEM investigations of our samples show the high quality of the c-oriented heteroepitaxial growth (Fig. 4). Very few dislocations penetrate to the active zone. However, during embedding, new dislocations are formed at the coalescence region, presumably caused by high strain due to the large indium content of the quantum well. In similar samples with QWs emitting in the blue spectral range and lower In content, the active zone maintained the disclocation density of the underlying template [13]. Nevertheless, we find no stacking faults, which are a common challenge to semipolar GaN [14]. The high quality and homogeneity of the QWs, paramount for efficient light emission, relies on a nano-scale precision of all patterning processes and is clearly visible in high-angle center-dark-field (HACDF) images (Fig. 5). The ridge of the nanostripes is as narrow as 2 nm (HRTEM picture not shown).

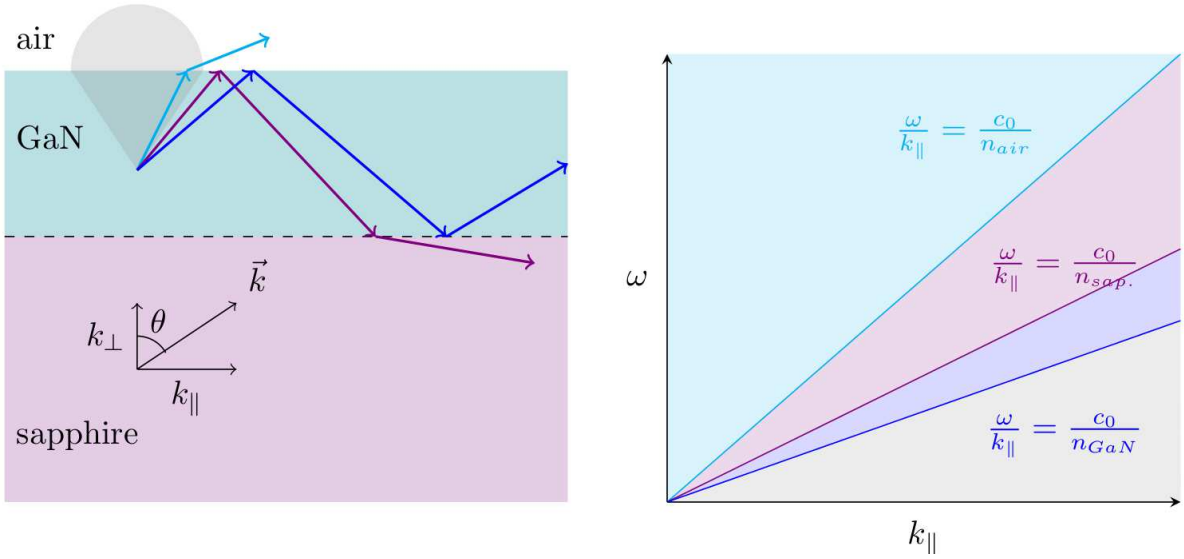

Fig. 6: Waveguiding within a GaN layer on sapphire (left) and the resulting dispersion relation (right). ω is the angular frequency and $k_\parallel$ is the part of the wave vector parallel to the sample surface. In the dispersion relation, the cyan area relates to directly emitted light. Light emitted more shallowly is totally reflected. In the violet area, the light leaks into the substrate. Between the violet sapphire line and the blue GaN line (blue area), the light is guided inside the GaN layer and forms discrete modes. Below the GaN line (gray area) no light propagation is possible.

3.3 Emission properties

Since the embedding of the nanostripes leads to a planar surface of the LED, light emitted by the semipolar QWs will be reflected internally if its angle towards the surface normal θ is larger than the critical angle $\sin\theta_c = n_{\text{air}}/n_{\text{GaN}}$. If we take the wave vector parallel to the surface $k_\parallel = |\vec{k}|\sin\theta$ with $|\vec{k}| = 2\pi n_{\text{GaN}}/\lambda$, the requisition for total reflection is

$$k_{\parallel,c} = |\vec{k}|\sin\theta_c = \frac{2\pi n_{\text{GaN}}}{\lambda}\frac{n_{\text{air}}}{n_{\text{GaN}}}, \quad \omega = 2\pi c/\lambda, n_{\text{air}} \approx 1, \quad \Rightarrow k_{\parallel,c} = \frac{\omega}{c}\,. \tag{1}$$

λ is the vacuum wavelength, ω is the angular frequency and c the vacuum velocity of light. The boundary condition of $k_\parallel = \omega/c$ defines the light cone. All emission with k-vectors inside the light cone are emitted directly from the surface. When the k-vector lies outside the light cone, the light is confined within the layer (see Fig. 6).

Discrete modes are formed which store a large part of the energy lost in conventional devices without light extraction mechanisms [15]. The number and spacing of the confined modes depend on the geometry of the device, with the typical thickness of a LED layer stack leading to dozens of modes with narrow linewidths. The presence of a cladding layer below the active zone introduces additional modes which are efficiently pumped (store more energy) due to the large spatial overlap with the emitting QWs (Fig. 7). For non-structured devices, these cladding modes would still be confined and ultimately lost. The periodic variation of the dielectric function caused by the growth mask of the GaN nanostripes acts as photonic crystal. The reciprocal lattice vector $\vec{G}$ of the PhC can be

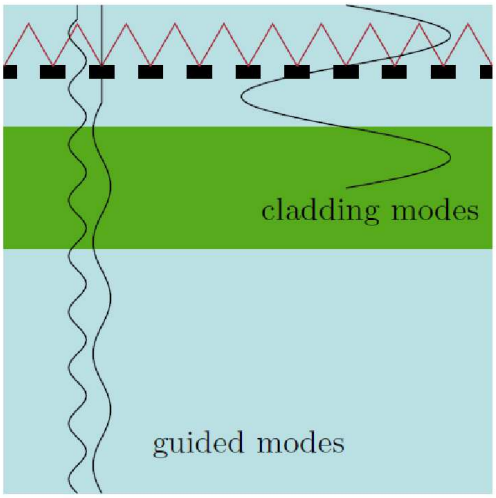

Fig. 7: Introducing an additional cladding layer, most energy is stored inside low order cladding modes with a large overlap with both the QWs and the PhC.

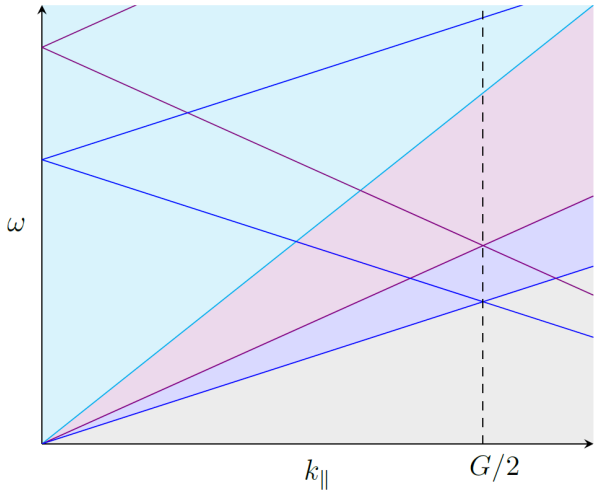

Fig. 8: The PhC leads to a periodicity of the dispersion relation. Confined light (i.e. located between sapphire and GaN line) is folded back into the light cone and extracted.

added to the wave vector of the confined modes $\vec{k}^* = \vec{k} + n \cdot \vec{G}$, folding them back into the light cone and extracting them with high efficiency, shown in Fig. 8. Since the cladding mode stores more energy, than the high-order modes, we obtain a directional emission with a narrow linewidth. Furthermore the semipolar nature of the QWs leads to a high polarization degree [2,3,16]. For full analysis of the luminescence properties, the samples are investigated by polarization-dependent ARPL (Fig. 9). Spectral resolution is 0.7 nm and angular resolution is 0.33°.

The flat sample surface leads to typical Fabry-Pérot modulations. The guided modes are extracted by the PhC and appear as sharp resonances. The inclusion of the AlGaN cladding layer leads to a high intensity of few select cladding modes. The very sharp high order modes which propagate in the complete layer stack carry less energy. This preferential selection leads to a strong directionality for the true-green QW emission with highest intensity between 10° and 25°. Comparison of single spectra, taken in this range, show that the cladding mode is highly polarized parallel to the a-direction (parallel to the nanostripes) and exhibits a full-width at half-maximum (FWHM) of 17 meV which gives a Q-factor of 150. The ARPL spectra can be transformed into the dispersion relation (Fig. 10) using the axis transformation (λ, θ) to $(a/\lambda, a/\lambda \cdot \sin(\theta))$ with a being the periodicity of the PhC, which corresponds to reduced frequency and parallel wave vector respectively. The light line marks the border of the light cone. GaN, AlGaN and sapphire line are folded back by the PhC and indicate the area where guided modes can exist. GaN and AlGaN lines are calculated by using a Lorentz oscillator model for the dielectric function [12]. Guided modes within the GaN layer are parallel to the GaN line and confined between GaN line and sapphire line, the cladding mode is localized between GaN and AlGaN line. This is in contrast to the Fabry-Pérot modes which are found without boundary. FDTD simulations with MEEP [11] are in good agreement with the experimental data (not shown).

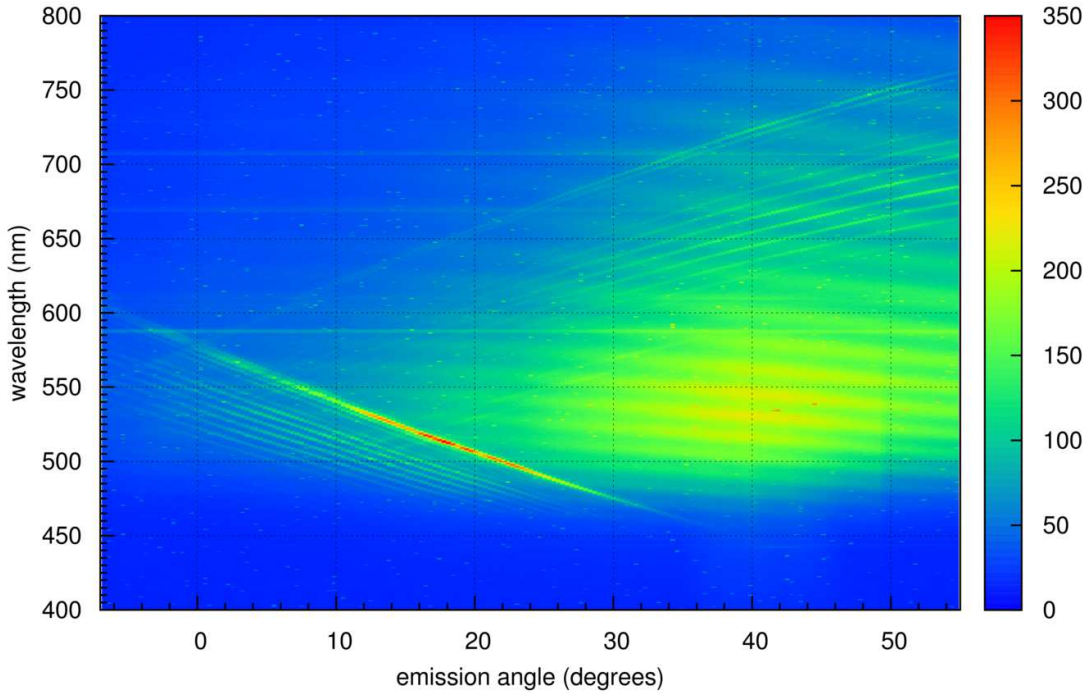

Fig. 9: ARPL spectrum of PhC LED. The polarizer is set parallel to the a-direction. We observe efficient mode outcoupling by the PhC. A single cladding mode has enhanced intensity, is highly polarized and exhibits a narrow linewidth.

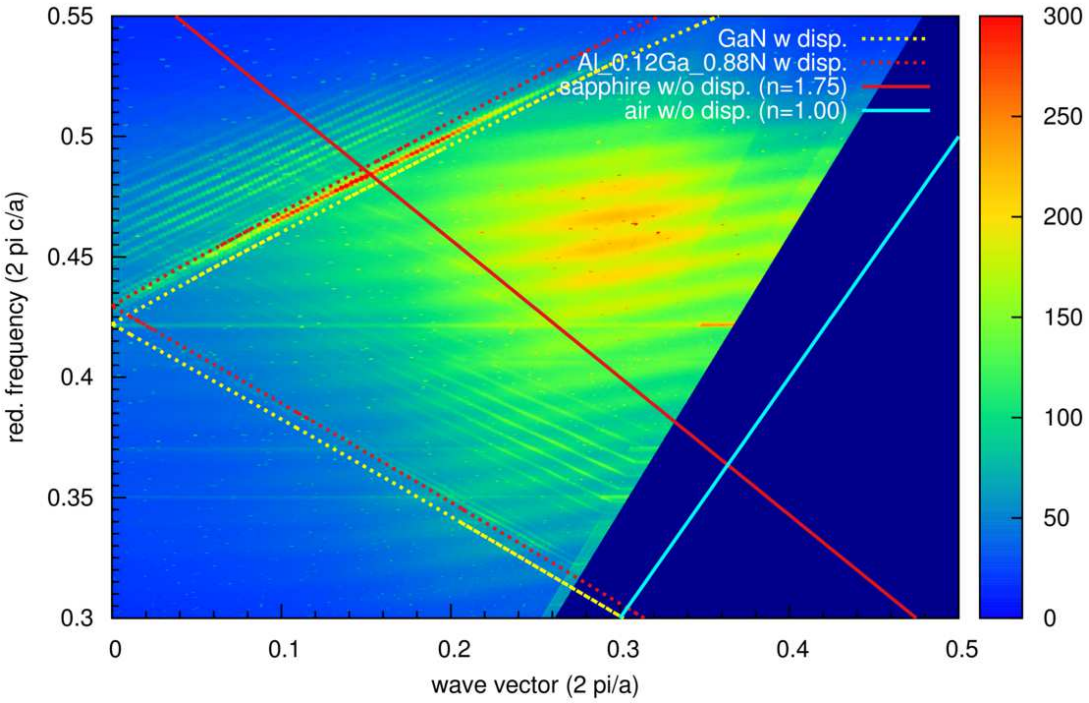

Fig. 10: Dispersion relation of the PhC LED. The cladding mode is localized between the GaN line and AlGaN line.

4. Conclusion

In this work, a PhC LED based on GaN nanostripes with semipolar QWs emitting in the true-green spectral range has been demonstrated on c-sapphire substrates. Nanopatterning was achieved on full 2-inch wafers. TEM analysis shows excellent structural quality, electrical excitation shows stable emission up to 100 mA. The directional extraction of highly polarized cladding modes was demonstrated by angle-resolved photoluminescence.

Acknowledgment

This work was made possible by many fruitful collaborations. Scientific support from D. Heinz, J. Wang, T. Meisch, F. Scholz, F. Huber, K. Thonke, J. Biskupek and U. Kaiser is gratefully acknowledged. Furthermore, I thank J. Harming and C. Thanner from EVG for nanoimprint patterning, R. Rösch and R. Blood for their technical support, B. Neuschl and O. Rettig for fruitful discussions and S. Grözinger for TEM sample preparation. The research was funded by Deutsche Forschungsgemeinschaft (DFG) within the research group FOR957 PolarCoN.

References

[1] C. Wiesmann, K. Bergenek, N. Linder, and U.T. Schwarz, "Photonic crystal LEDs – designing light extraction", *Laser and Photonics Reviews*, vol. 3, pp. 262–286, 2009.

[2] M. Feneberg, F. Lipski, R. Sauer, K. Thonke, P. Brückner, B. Neubert, T. Wunderer, and F. Scholz, "Polarized light emission from semipolar GaInN quantum wells on $\{1\bar{1}01\}$ GaN facets", *J. Appl. Phys.*, vol. 101, pp. 053530-1–6, 2007.

[3] R.A.R. Leute, D. Heinz, J. Wang, F. Lipski, T. Meisch, K. Thonke, J. Thalmair, J. Zweck, and F. Scholz, "GaN based LEDs with semipolar QWs employing embedded sub-micrometer sized selectively grown 3D structures", *J. Cryst. Growth*, vol. 370, pp. 101–104, 2013.

[4] J.D. Joannopoulos, P.R. Villeneuve, and S. Fan, "Guided modes in photonic crystal slabs", *Nature*, vol. 386, pp. 143–149, 1997.

[5] D. Heinz, "Zweidimensionale photonische Kristalle basierend auf nitridischen Halbleitern", Diplomarbeit, Universität Ulm, Institut für Quantenmaterie – Gruppe Halbleiterphysik der Fakultät für Naturwissenschaften, 2011.

[6] K. McGroddy, A. David, E. Matioli, M. Iza, S. Nakamura, S. DenBaars, J.S. Speck, C. Weisbuch, and E.L. Hu, "Directional emission control and increased light extraction in GaN photonic crystal light emitting diodes", *Appl. Phys. Lett.*, vol. 93, pp. 103502-1–3, 2008.

[7] E. Matioli and C. Weisbuch, "Impact of photonic crystals on LED light extraction efficiency: approaches and limits to vertical structure designs", vol. 43, pp. 354005-1–6, 2010.

[8] B. Kuhn and F. Scholz, "An oxygen doped nucleation layer for the growth of high optical quality GaN on sapphire", *Phys. Status Solidi A*, vol. 188, pp. 629–633, 2001.

[9] J. Hertkorn, F. Lipski, P. Brückner, T. Wunderer, S.B. Thapa, F. Scholz, A. Chuvilin, U. Kaiser, M. Beer, and J. Zweck, "Process optimization for the effective reduction of threading dislocations in MOVPE grown GaN using in situ deposited SiN_x masks", *J. Cryst. Growth*, vol. 310, pp. 4867–4870, 2008.

[10] R.A.R. Leute, J. Wang, T. Meisch, J. Biskupek, U. Kaiser, and F. Scholz, "Blue to true green LEDs with semipolar quantum wells based on GaN nanostripes", *Phys. Status Solidi C*, 2014, DOI: 10.1002/pssc.201400176.

[11] A.F. Oskooi, D. Roundy, M. Ibanescu, P. Bermel, J.D. Joannopoulos, and S.G. Johnson, "MEEP: A flexible free-software package for electromagnetic simulations by the FDTD method", *Comput. Phys. Commun.*, vol. 181, pp. 687–702, 2010.

[12] D. Heinz, R.A.R. Leute, S. Kizir, Y. Li, T. Meisch, K. Thonke, and F. Scholz, "Ga(In)N photonic crystal light emitters with semipolar quantum wells", *Jpn. J. Appl. Phys.*, vol. 52, pp. 062101-1–5, 2013.

[13] R.A.R. Leute, T. Meisch, J. Wang, J. Biskupek, U. Kaiser, M. Muller, P. Veit, F. Bertram, J. Christen, and F. Scholz, "GaN laser structure with semipolar quantum wells and embedded nanostripes", in Proc. *10th Conf. on Lasers and Electro-Optics Pacific Rim (CLEO-PR)*, paper WH3-4, 2 pages, June 2013.

[14] F. Wu, Y. Zhao, A. Romanov, S.P. DenBaars, S. Nakamura, and J.S. Speck, "Stacking faults and interface roughening in semipolar $(20\bar{2}\bar{1})$ single InGaN quantum wells for long wavelength emission", *Appl. Phys. Lett.*, vol. 104, pp. 151901-1–5, 2014.

[15] T. Fujii, Y. Gao, R. Sharma, E.L. Hu, S.P. DenBaars, and S. Nakamura, "Increase in the extraction efficiency of GaN-based light-emitting diodes via surface roughening", *Appl. Phys. Lett.*, vol. 84, pp. 855–857, 2004.

[16] Y. Zhao, R.M. Farrell, Y.R. Wu, and J.S. Speck, "Valence band states and polarized optical emission from nonpolar and semipolar III-nitride quantum well optoelectronic devices", *Jpn. J. Appl. Phys.*, vol. 53, pp. 100206-1–17, 2014.

Defect Reduction in GaN by Facet Assisted Lateral Overgrowth With Hexagonal Mask Geometry

Maryam Alimoradi-Jazi and Ferdinand Scholz

The goal of this project was the development of a complex growth procedure of a GaN layer on sapphire with minimized dislocation density, which can be used as template for the subsequent growth of a thick GaN layer by hydride vapor phase epitaxy. We extended a conventional stripe-based FACELO approach (FACELO = facet assisted epitaxial lateral overgrowth) [1] to a mask geometry where the stripes are arranged as a hexagonal honeycomb grid. We expect a more uniform defect reduction and more isotropic strain and curvature development in the GaN layer by such a mask geometry. By a careful optimization of each layer in a multi-layer growth procedure, GaN structures with excellent spectroscopic properties could be grown. Although some surface features visible by optical microscopy could not be completely suppressed, a very low dislocation density below $10^6\ cm^{-2}$ *was evaluated from etch experiments performed in our hydride vapor phase reactor.*

1. Introduction

GaN layers and device structures grown on foreign substrates like sapphire still dominate by far the current approaches for such structures, although the hetero-epitaxial approach leads to a comparably huge defect density. Various defect-reduction methods have been developed over the recent decades, mainly based on the idea of 'epitaxial lateral overgrowth' (ELO) [2]. A particularly effective method was originally proposed by Vennéguès *et al.* [3], called 'facet-assisted epitaxial lateral overgrowth' (FACELO) [4]: On a GaN template layer, a dielectric stripe mask is fabricated. In a second epitaxial process, GaN grows out of the mask openings forming GaN stripes with triangular cross section. By changing the growth conditions, lateral growth can be enhanced leading to a lateral bending of the originally vertically running threading dislocations. This potentially leads to a completely dislocation-free final surface, if the coalescence of neighboring stripes does not induce new defects. Besides the coalescence problem, this approach leads to an anisotropic strain situation in the final GaN layer with great differences for the strain parallel and perpendicular to the stripes.

Based on our previous work towards the conventional FACELO approach [1], we extended such a stripe-based approach to a mask geometry where the stripes are arranged as a hexagonal honeycomb grid. We expect a more uniform defect reduction and more isotropic strain and curvature development by such a mask geometry.

2. Experimental

For these studies, optimized c-plane GaN layers grown by metalorganic vapor phase epitaxy (MOVPE) [5] are used as templates, which contain a fairly low dislocation density of about $3-5\cdot10^8\,\mathrm{cm}^{-2}$. On those templates, a 200 nm thick SiO_2 layer is deposited on top by plasma enhanced chemical vapor deposition (PECVD) as a mask for the subsequent selective area growth of GaN. A stripe pattern with periodicity of 11 µm (3 µm opening) is created in the SiO_2 layer.

In the second MOVPE process, a multi step procedure is applied based on our earlier findings [1]. This process needed careful adaption to the current MOVPE reactor conditions etc. which have been changed since our studies in 2004.

3. FACELO Multi-Step Growth of GaN With Stripe Mask

In the first overgrowth step, GaN stripes with a triangular cross section are developed at a temperature of 980 °C and pressure of 250 hPa. Then, lateral overgrowth is enhanced by lowering the reactor pressure and increasing the temperature. In the last step, very good coalescence is achieved at higher temperature and lower reactor pressure, leading to samples without wing-tilt, as observed in scanning electron microscopy (SEM, Fig. 1, left) and confirmed by only one peak in high-resolution X-ray diffraction (HRXRD) 0002 rocking curve measurements (Fig. 2, left). The still fairly large full width at half maximum (FWHM) of such peaks of about 280 arcsec may be due to some bowing of the samples. For the X-ray beam parallel to the stripes, the samples exhibit very narrow peaks with a FWHM of only 150 arcsec. However, the surface is not completely smooth (Fig. 1, right).

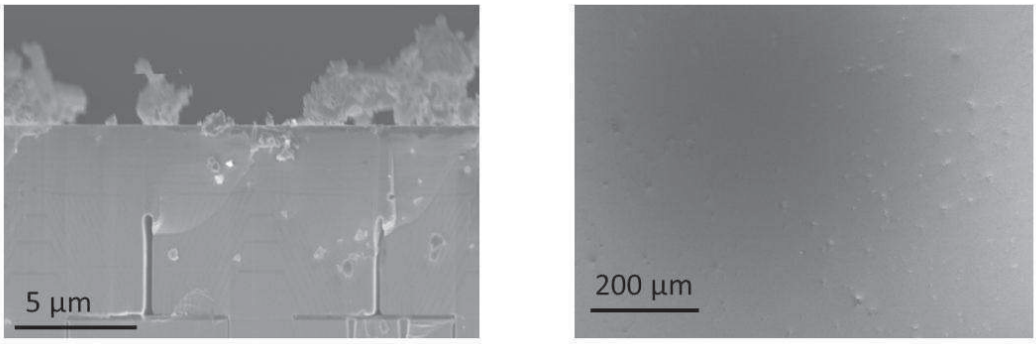

Fig. 1: SEM cross section (left) and top view image (right) of stripe mask sample. The dust seen in the cross section image is some contamination after cleaving of the sample.

The low-temperature photoluminescence (PL) spectra of this sample (Fig. 2, right) shows an extremely narrow peak at 3.487 eV related to the donor-bound excitonic transition (D°X) with a FWHM of 2 meV. The peak at 3.493 eV can be related to the free exciton (named FX) as confirmed by temperature dependent PL measurement.

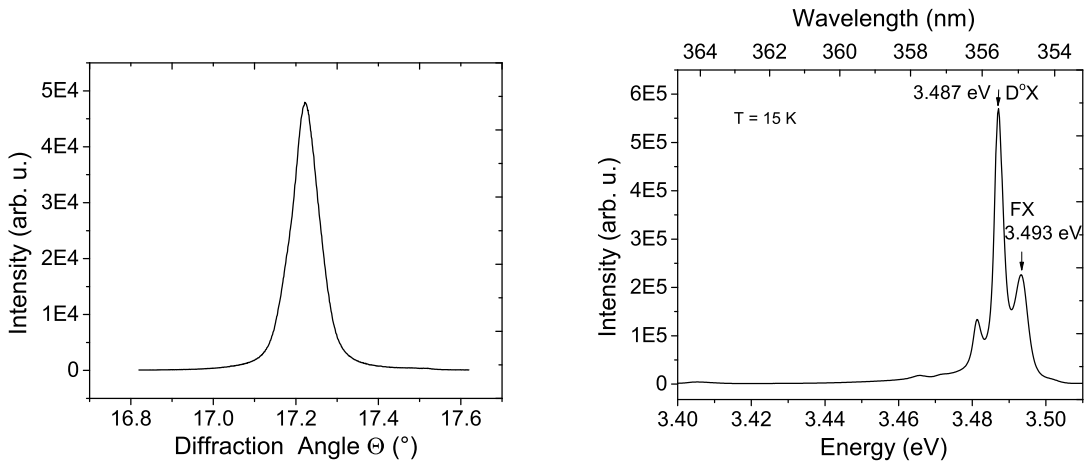

Fig. 2: HRXRD rocking curve with the beam perpendicular to the stripes (left) and low temperature PL spectra (right) for the sample on SiO_2 mask.

To improve the surface morphology, we reduced the growth temperature in both, the lateral growth and coalescence steps to 1020 °C and 1065 °C respectively. Indeed, we successfully reduced the size of the round shaped defects in the surface (Fig. 3). By HRXRD rocking curve measurements we could confirm that this temperature reduction doesn't lead again to some wing-tilt, which is often observed in such structures [6]. For the 0002 reflection with the beam parallel and perpendicular to the stripes, only one peak with a FWHM of 300 and 375 arcsec, respectively, was observed.

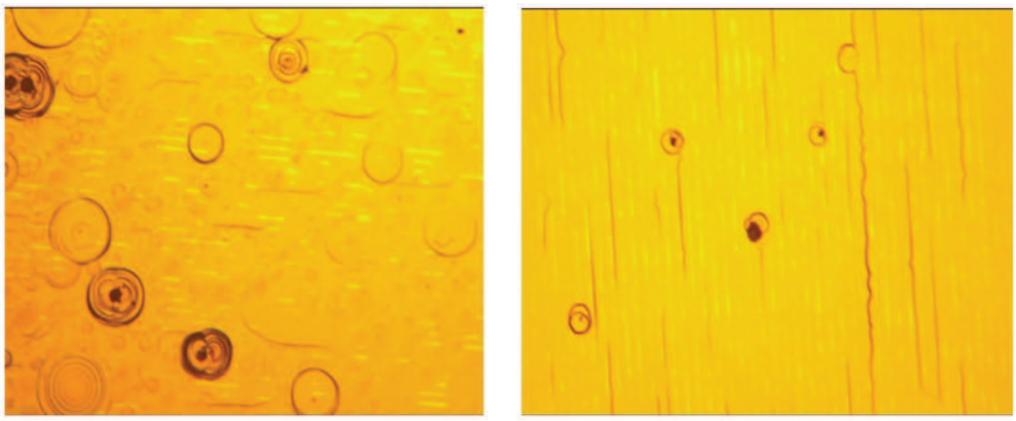

Fig. 3: Optical microscope image for sample with stripe structure: Lateral and coalescence growth performed at high temperature (left) and at low temperature (right).

The low temperature PL measurements further confirmed the high quality of these samples (Fig. 4), featuring a narrow and intense signal at 3.486 eV related to the D°X transition with a FWHM of 3 meV and the free-exciton peak at 3.492 eV.

These optimized parameters formed a sound base for our further investigations using a honeycomb mask made of SiO_2.

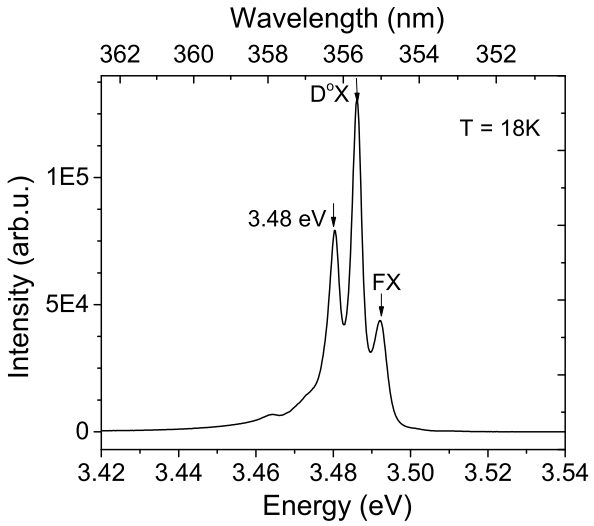

Fig. 4: Low temperature PL spectrum for the sample with stripe structure and improved surface morphology.

4. FACELO Multi-Step Growth of GaN With Hexagonal Mask

We extended our stripe-based approach to a mask geometry where the stripes are arranged as a hexagonal honeycomb grid with a periodicity of 13 µm and an open stripe width of 3 µm with the stripes running along the m-directions of GaN. In the first overgrowth step, GaN with a triangular cross section is developed at a temperature of 980 °C and pressure of 200 hPa (Fig. 5, left). Then, lateral overgrowth is enhanced by lowering the reactor pressure to 90 hPa and increasing the temperature to 1160 °C. As it is seen in the SEM cross section image (Fig. 5, right), no tilting angle in the top c-plane surface is observed.

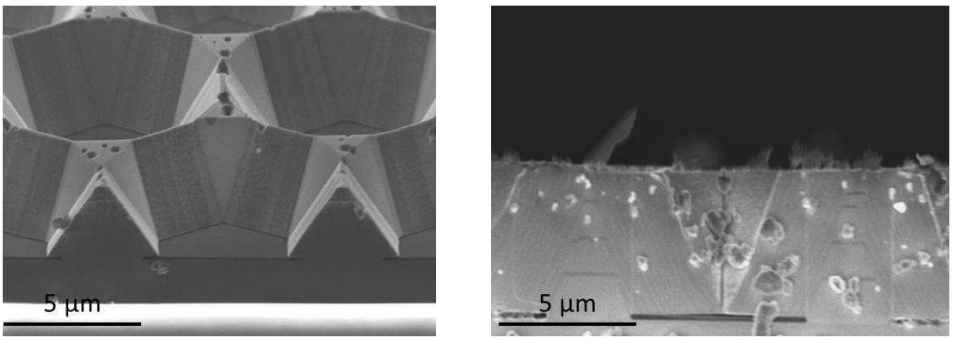

Fig. 5: SEM bird's eye view after second growth step (left), cross section image after lateral growth step (right).

In the last step, the coalescence is achieved at a higher temperature of 1220 °C and the same pressure of 90 hPa (Fig. 6a). However, again, the surface is not completely smooth (Fig. 6b and 8, right). We also have studied another mask orientation with a 30° rotation of the hexagonal structure resulting in $(10\bar{1}1)$ facets at the beginning of the growth procedure (sample B). The SEM cross section for this sample also confirms that the FACELO technique is working (Fig. 6c). However, the surface is rougher than on the sample A with the lines of the mask running along m-direction (Fig. 6d). The FWHMs of

the HRXRD rocking curve peaks are determined to 325 and 370 arcsec for samples A and B, respectively. Therefore, sample A is considered as the desirable result. Furthermore, the PL spectrum for this sample exhibits an extremely intense and narrow peak (FWHM of 3 meV) related to the D°X transition (Fig. 7).

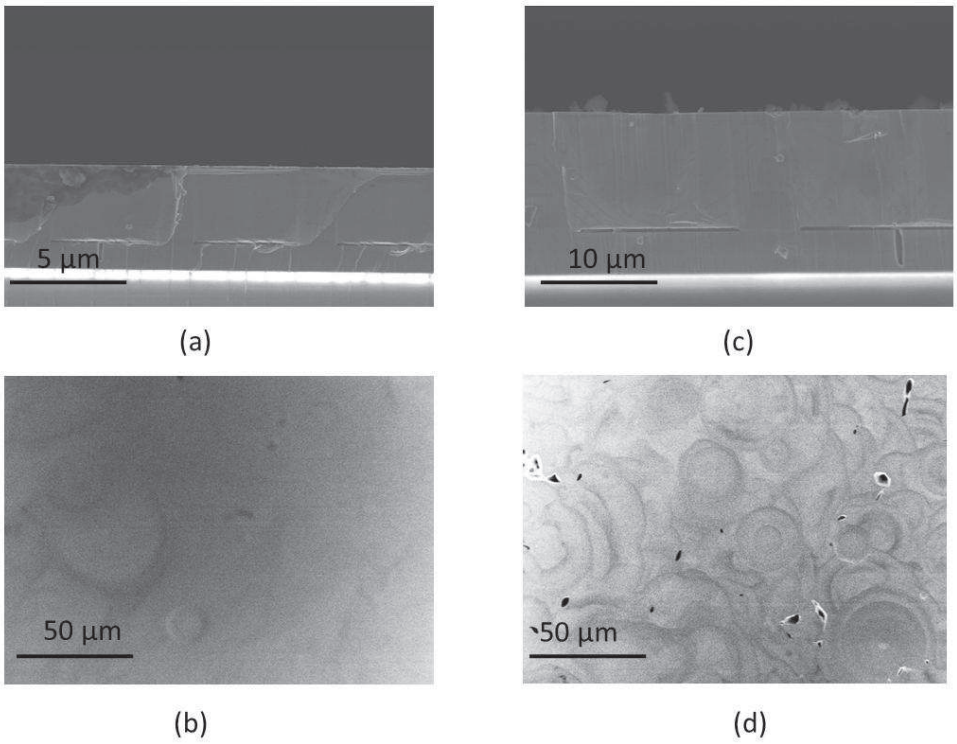

Fig. 6: SEM micrographs of the samples grown with the hexagonal masks: cross section (a, c) and top view (b, d) images of samples A and B, respectively.

The procedure to improve the surface morphology of stripe mask samples mentioned in Sect. 3 was then also applied successfully to our hexagon mask samples: We decreased again the temperature of the lateral and coalescence growth to 1080 °C and 1150 °C, respectively (Fig. 8, right). Very narrow rocking curve peaks with FWHM of 190 and 240 arcsec for the beam parallel and perpendicular to the stripes, respectively, confirm their excellent quality with no indication for any wing-tilt, again confirmed by excellent PL spectra with an extremely intense and narrow D°X peak (FWHM of 2 meV) at 3.488 eV and a significant FX related signal at 3.492 eV (Fig. 9).

5. Etch Pit / Dislocation Density

In order to evaluate the dislocation density of our optimized samples, we have applied our vapor phase etching process where the samples are exposed to 50 sccm HCl gas diluted by nitrogen at an elevated temperature of 600 °C and a pressure of 940 hPa for 15 minutes in an Aixtron hydride vapor phase epitaxy (HVPE) reactor [7] to decorate the dislocations on the surface. The sample with the coalesced stripes and sample A and

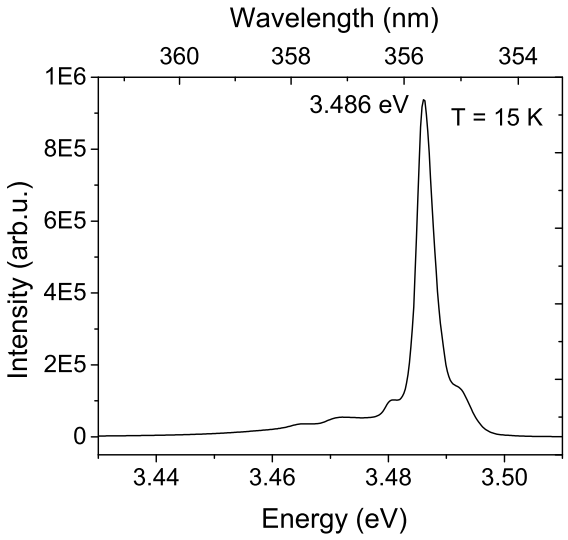

Fig. 7: Low temperature PL spectrum of sample A.

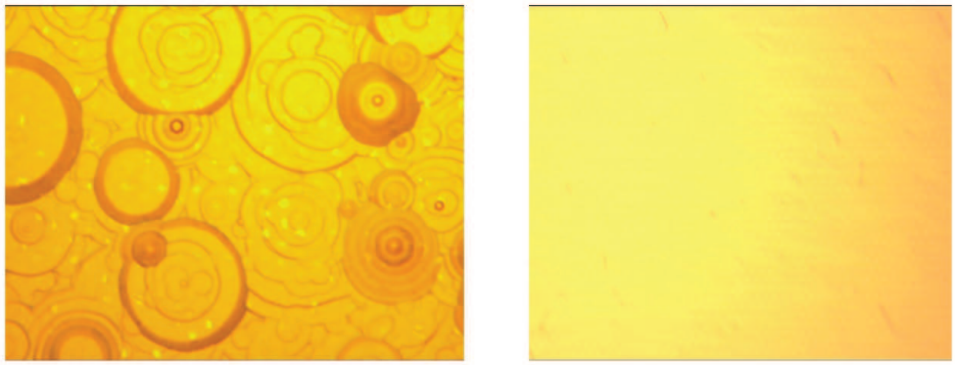

Fig. 8: Optical microscope image for sample with hexagonal structure: Lateral and coalescence growth performed at high temperature (left) and at low temperature (right).

B with the coalesced hexagonal structures were etched by the described experiment. In addition, a standard c-plane GaN layer was etched to check the validity of the experiment. $10 \times 10\,\mu m^2$ atomic force microscopy (AFM) scans were evaluated to determine the etch pit density (EPD; Fig. 10). On the standard c-plane sample, we found an EPD value of $5 \cdot 10^8\,cm^{-2}$ (Fig. 10a), which is very reasonable for such a sample. However, no pits were observed on the other three samples (Fig. 10b-d) which obviously confirms the very low dislocation densities for the samples grown by the FACELO technique. Even on larger area AFM scans including about three periods of stripes and hexagons ($30 \times 30\,\mu m^2$), we could not identify etch pits on the optimized FACELO samples. Hence, we estimate the EPD to be below $10^6\,cm^{-2}$.

6. Summary

Based on our experience obtained in 2004, we could re-establish a multi-step FACELO process for GaN on sapphire by using a stripe mask pattern. By carefully improving this process, layers with excellent X-ray and photoluminescence properties have been

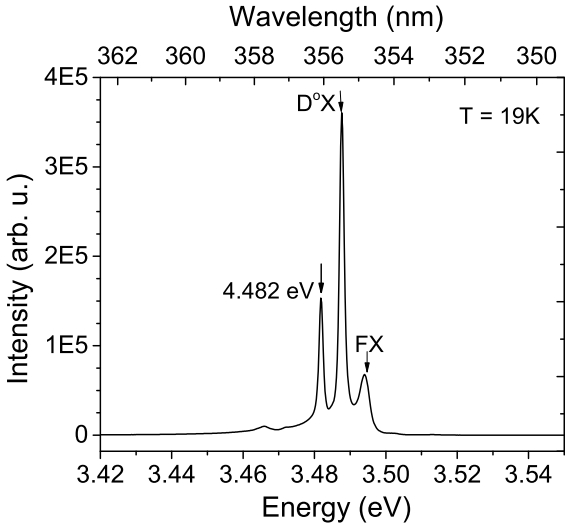

Fig. 9: Low temperature PL spectrum for the sample with hexagonal structure and improved surface morphology.

obtained. The very often observed wing-tilt could be efficiently suppressed. Also the surface morphology could be drastically improved, although some features still are present on the best wafers. Anyway, the density of threading dislocations at the surface could be decreased to values below $10^6\,\mathrm{cm}^{-2}$ according to EPD experiments performed in our HVPE reactor. These excellent properties have been also obtained on samples grown on full 2" sapphire wafers using a mask pattern with hexagonal (honeycomb) geometry in order to improve the lateral isotropy of our structures. Very similar data have been obtained on such wafers as on the stripe mask wafers including EPD-values below $10^6\,\mathrm{cm}^{-2}$.

Acknowledgment

We thank Tobias Meisch, Martin Klein and Thomas Zwosta for technical assistance and Junjun Wang for fruitful discussions. This work was financially supported by Freiberger Compound Materials, which is gratefully acknowledged.

References

[1] F. Habel, P. Brückner, and F. Scholz, "Marker layers for the development of a multi-step GaN FACELO process", *J. Cryst. Growth*, vol. 272, pp. 515–519, 2004.

[2] K. Hiramatsu, "Epitaxial lateral overgrowth techniques used in group III nitride epitaxy", *J. Phys.: Condens. Matter*, vol. 13, pp. 6961–6975, 2001.

[3] P. Vennéguès, B. Beaumont, V. Bousquet, M. Vaille, and P. Gibart, "Reduction mechanisms for defect densities in GaN using one- or two-step epitaxial lateral overgrowth methods", *J. Appl. Phys.*, vol. 87, pp. 4175–4181, 2000.

[4] K. Hiramatsu, K. Nishiyama, M. Onishi, H. Mizutani, M. Narukawa, A. Motogaito, H. Miyake, Y. Iyechika, and T. Maeda, "Fabrication and characterization of low defect

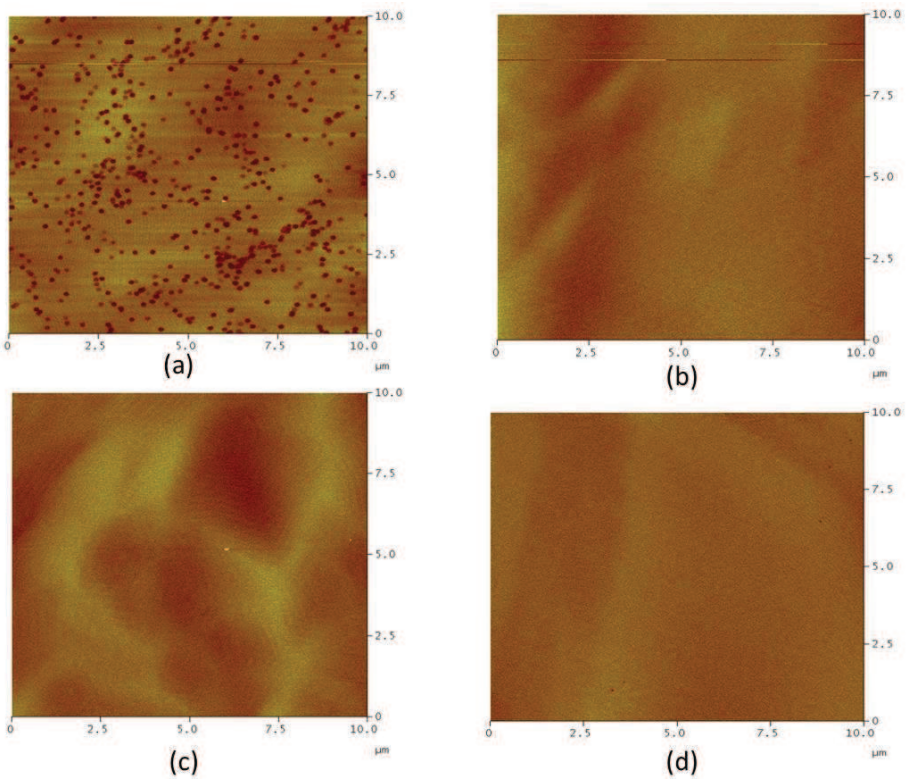

Fig. 10: $10 \times 10\,\mu m^2$ AFM image of etched samples: normal c-plane (a), coalesced stripes (b), sample A (c) and sample B (d) with the coalesced hexagonal structures.

density GaN using facet-controlled epitaxial lateral overgrowth (FACELO)", *J. Cryst. Growth*, vol. 221, pp. 316–326, 2000.

[5] J. Hertkorn, F. Lipski, P. Brückner, T. Wunderer, S.B. Thapa, F. Scholz, A. Chuvilin, U. Kaiser, M. Beer, and J. Zweck, "Process optimization for the effective reduction of threading dislocations in MOVPE grown GaN using in situ deposited SiN_x masks", *J. Cryst. Growth*, vol. 310, pp. 4867–4870, 2008.

[6] P. Fini, A. Munkholm, C. Thompson, G.B. Stephenson, J.A. Eastman, M.V. Ramana Murti, O. Auciello, L. Zhao, S.P. DenBaars, and J.S. Speck, "In situ, real-time measurement of wing tilt during lateral epitaxial overgrowth of GaN", *Appl. Phys. Lett.*, vol. 76, pp. 3893–3895, 2000.

[7] F. Habel and M. Seyboth, "Determination of dislocation density in epitaxially grown GaN using an HCl etching process", *Phys. Status Solidi C*, vol. 0, pp. 2448–2451, 2003.

Ferrocene Doping in Horizontal Hydride Vapor Phase Epitaxy

Martin Klein

In order to produce semi-insulating, thick layers of gallium nitride we try to incorporate iron into our hydride vapor phase grown material. As past experiments have shown, a solid iron source inside the reactor is not adequate in terms of controllability and purity. Therefore our reactor has been upgraded with a gasoues ferrocene source. This article demonstrates first promising results and shows the current problems together with some possibilities to solve them.

1. Introduction

Gallium nitride (GaN) is a very promising material for the production of high power, high frequency transistor devices [1,2]. However, the standard material grown in metal organic vapor phase epitaxial (MOVPE) and hydride vapor phase epitaxial (HVPE) machines suffer from comparably high unintentional n-type doping levels. These high doping levels favor the formation of parasitic, conductive channels, interfering with the on/off ratio of the device. As a simple and carefree way to get rid of excess carriers we are trying to incorporate deep level traps into our thick GaN buffers grown by HVPE. The source element of our choice to achieve this is iron [3]. In former studies we have described the doping of our HVPE grown GaN by creating iron-chloride from a solid iron source inside the reactor [4]. However, controllability and purity of the source did not meet our requirements in the end. In general, gaseous sources are known to perform very well in both of these regimes. Indeed, ferrocene is well established as a metalorganic precursor for iron doping in MOVPE [5] and has also been tested in HVPE growth of GaN before [6]. Because of the horizontal hot-wall design of our reactor, special care has to be taken in the design of the doping line. With our project partner Aixtron we were able to overcome these specific problems and successfully added a ferrocene source to our setup.

2. Design of the Doping Line

We expected, that for the high amount of unintentional dopants in our standard layers, we need a lot of incorporated iron for compensation. Owing to the low vapor pressure of ferrocene, this can only be realized by heating the bubbler. The standard implementation of such a heating consists of a temperature controlled bath with a heat transfer medium which contains the bubbler and keeps it at the desired temperature. During the transport to the reactor we must not allow the hot gas to cool down, else we risk depositions inside

the transport line. The solution is a line heating, reaching from the last flow controller to the reactor inlet. For better controlability of the doping level, a dilution stage has been chosen for use with the bubbler setup (Fig. 1). The setup can be supplied by either nitrogen or hydrogen for different operation purposes.

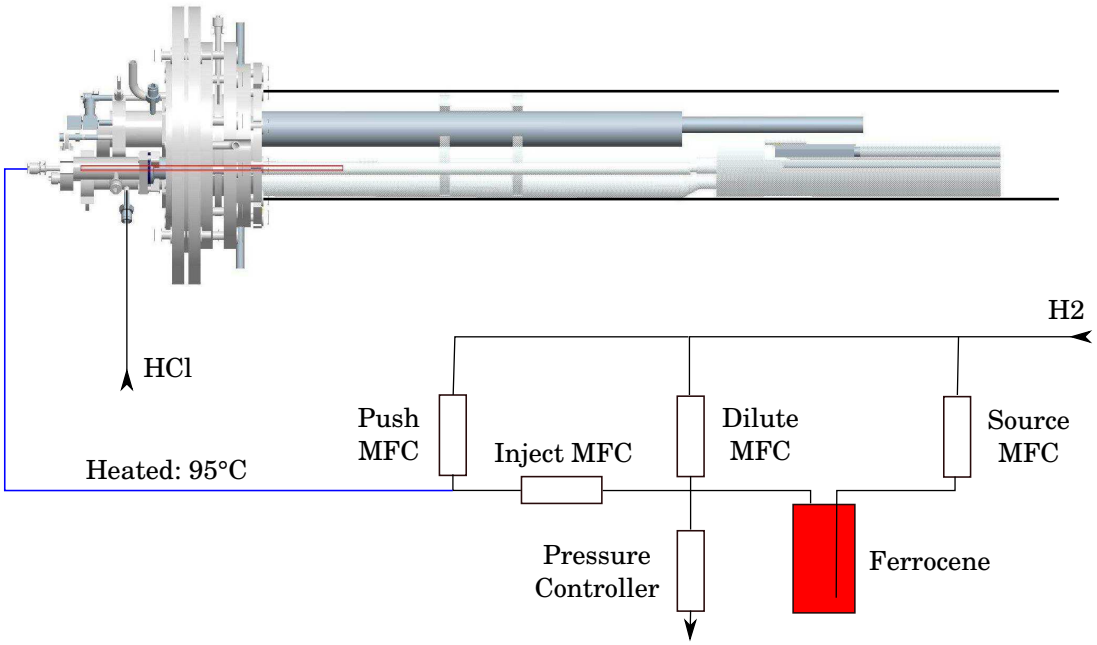

Fig. 1: Reactor source flange and bubbler setup with gas flow controllers. Gas flow from hydrogen source to the growth zone: the bubbler is fed with gas by the source MFC. The hereby enriched carrier gas can be diluted and sent towards the reactor via the inject MFC. In order to regulate the pressure, the pressure controller sends surplus gas to the vent. For faster transport, the injected gas can be filled up with the push MFC. After the heated line from the push MFC to the reactor, a small tube guides the gas into the reactor. HCl is provided coaxially through the same flange for creation of iron chloride inside the heated zone.

From literature we know that ferrocene decomposes at temperatures above 500 °C [7]. Because of our HVPE being a hot-wall reactor, the ferrocene has to be transported through thermal zones with temperatures of up to 1100 °C before it reaches the growth zone. To prevent the ferrocene from decomposing prematurely and forming an iron deposition on the glass parts, we add hydrogen chloride (HCl) to the carrier gas/ferrocene mixture. Ferrocene together with HCl forms the thermally stable gaseous species iron-(II)-chloride and iron-(III)-chloride at elevated temperatures, which then can be transported to the growth zone.

With the new line installed, the reactor inlet flange is almost at its maximum functionality (Fig. 2 (top)). For the purpose of introducing the new source gases into the reactor, the small 25 mm flange between the Ga-channel and the ammonia inlet has been chosen. On top of this flange, a short steel tube with a side inlet has been mounted (Fig. 2 (bottom)). Inside this tube we find a spring load mechanism that fastens the glass tube reaching into the reactor. At the end of the steel tube we find another 25 mm flange that is sealed by

a lid, incorporating an ultra-torr fitting on the inside and a VCR port on the outside. The ultra-torr holds a 8 mm glas tube that coaxially reaches into the bigger glass tube inside the reactor and transports the carrier gas/ferrocene mixture. The sideport is used to introduce HCl gas into the gap between the two coaxial glass tubes.

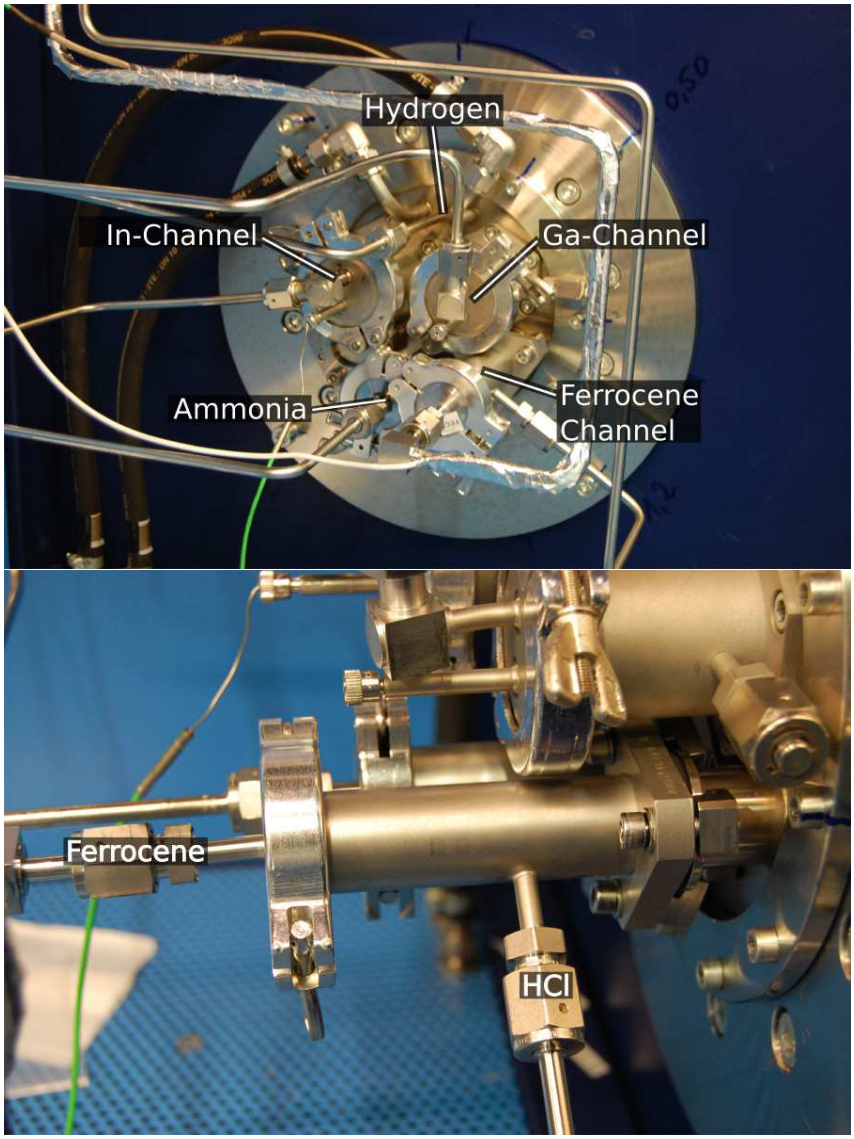

Fig. 2: Photographs of the reactor flange with all gas inlets (top) and the ferrocene inlet in detail (bottom).

Inside the reactor the spring loaded glass tube transports the gases towards a newly designed gas-mixing-chamber, where it is guided to a small showerhead on top of the growth zone. The 8 mm tube only covers some small part of this length. The end of this inner glass tube marks the mixing zone for the carrier gas/ferrocene mixture with the HCl and therefore defines the reaction temperature of these two species.

The small showerhead currently posseses 8 holes with a diameter of about 2 mm, dis-

tributed evenly over the 3" of the rotation tray, which is holding the sample substrate. By this design a uniform distribution of the dopant gas over the rotating wafer is expected.

3. Estimating the Operating Parameters

The parameters that influence the mass transport of the source material in a bubbler setup are the bubbler pressure, the carrier gas flux through the bubbler and the temperature of the material inside the bubbler.

Our HVPE growth is currently established at a reactor pressure of 900 hPa. In order for the ferrocene doping line to be functional, the bubbler pressure has to be kept above the reactor pressure. Therefore the bubbler pressure can currently not be set to values below 950 hPa. It is generally possible to establish growth at lower pressure values but this would require extensive optimization efforts.

Concerning the possible flux through the doping line, we conducted some ammonium-chloride haze experiments: in order to conduct such an experiment, we have filled the reactor with ammonia and subsequently supplied HCl flux to the source lines that are to be examined. At the position where the ammonia comes into contact with HCl, ammonium-chloride is formed. At room temperature, the ammonium chloride appears as a white haze and can be perceived optically. When supplying HCl to the new iron dopant line, we could see some depositions on all ports of the reactor inlet flange and at the quartz/quartz junction at the gas lead chamber above a total flux of 60 sccm of total gas supply to this line (Fig. 3). From this fact we can conclude, that leakages occur at these positions as a result of the combination of dynamic pressure effects inside the quartz tube and insufficient gas tightness at the respective junctions. Due to the thermally and chemically very harsh conditions inside the reactor, it is not possible to apply proper sealings at these junctions. As a result, we had to limit the maximum gas flow through the ferrocene doping line to 60 sccm in all subsequent experiments.

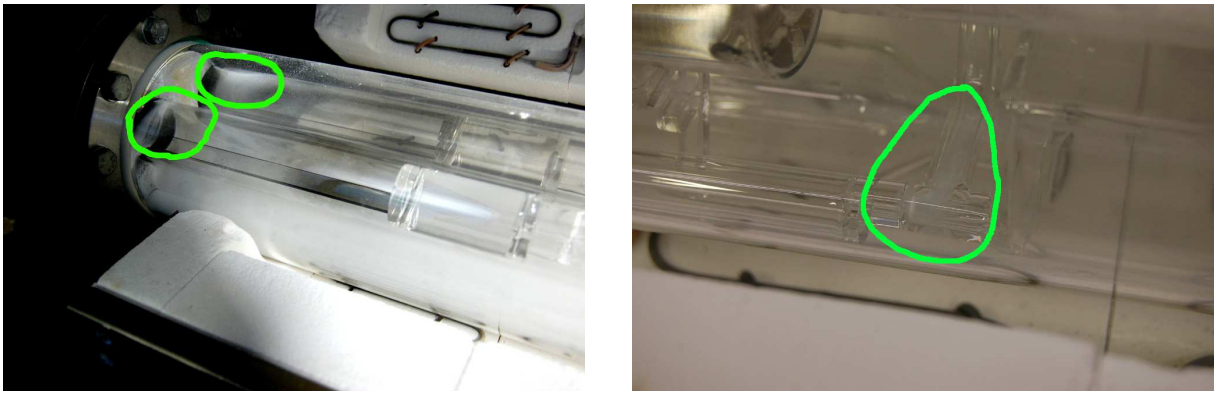

Fig. 3: Photographs of the reactor inlets (left) and the quartz tube/gas-mixing chamber junction (right) during an ammonium-chloride haze experiment to determine the maximum possible flow inside the ferrocene doping channel. Bright lines are enclosing ammonium-chloride depositions.

Table 1: Overview on sample resistivities.

Bath temperature (°C)	Bath medium	Growth rate (%)	Ferrocene flow (µmol min^{-1})	Resistivity (Ωcm)
-	-	100	0	0.2
25	Water	100	0.03	0.35
60	Water	50	0.65	3.6
90	Ultra 350	100	2.6	2.1
90	Ultra 350	100	6.2	1.8
90	Ultra 350	50	6.2	1.4

The parameter the most influential on the amount of ferrocene transported to the reactor, is the temperature of the bubbler. While carrier gas flux and bubbler pressure have a linear influence, the vapor pressure and hence the material flux is exponentially dependent on the temperature of the respective material. The highest stable temperature that can be achieved inside our transport lines with the installed line heating is 95 °C. Therefore the bubbler temperature should be limited to 90 °C, else we risk ferrocene depositions inside the gas lines.

If we set all parameters to their respective limits (bubbler pressure to 950 hPa, bubbler temperature to 90 °C and total doping line flux to 60 sccm), taking into account a vapor pressure of 200 Pa for ferrocene at the given temperature [8], we get a calculated maximum molar flow of 6.2 µmol min^{-1}.

4. First Doping Experiments

Table 1 shows the resistivity results for the first experiments that we conducted with the new doping setup. The first line of this table shows the resistivity of an undoped sample as a reference. The following samples have been grown during different stages of the installation of the setup. With the progressing installation of the line heating, we were able to increase the bubbler temperature step by step. Before increasing the bath temperature from 60 °C to 90 °C, we exchanged the bath medium from water to *Lauda Ultra 350*. This is a toluol based liquid which can be used to operate the bath with temperatures of up to 150 °C. As we can see, the resistivity values increase with an increasing calculated molar flow of up to 0.65 µmol min^{-1}, combined with a lower growth rate. For higher molar flows the resistivity decreases again. Lower growth rates seem to make things worse at these high ferrocene flow rates.

In order to exclude effects caused by premature decomposition of the ferrocene inside the reactor (see Sect. 2), we had a look at the short, 8 mm thick quartz pipe, transporting the ferrocene from the line into the reactor. Near the end of the small, inner quartz tube we could see a grey, transparent deposit (Fig. 4), most probably consisting of metallic iron. As a consequence, the 8 mm tube has been cut at the start of the grey deposits. By this we decrease the temperature at which we mix the ferrocene with the HCl gas, favoring the reaction of the ferrocene with HCl over thermal decomposition. However,

Table 2: SIMS sample overview.

Sample	Growth rate (%)	Ferrocene flow (µmol min^{-1})	Growth temperature (°C)	Resistivity (Ωcm)
A	50	0.65	1050	3.6
B	50	2.6	1050	1.7
C	100	6.2	1050	1.8
D	100	2.6	1050	0.49
E	100	2.6	950	0.018
F	100	2.6	1100	0.62

comparing samples before and after the shortening of the glass tube, only a small increase in resistivity could be seen.

Fig. 4: Photographof the 8 mm glass tube with iron deposits (inside the circle). The bright line marks the position of the shortening. The larger transport tube also shows some depositions.

As means to investigate the reasons for the low resistivity values at high ferrocene molar flows, we sent some samples to the Fraunhofer Institute for Applied Solid State Physics (IAF) in Freiburg, for secondary ion mass spectrometry (SIMS) of the iron concentration (Fig. 5). The Fe concentration near the surface of all analyzed samples approaches a value in the low $10^{17}\,\mathrm{cm}^{-3}$ range. However, at the beginning of the ferrocene doped growth in HVPE, we can see a peak in the iron concentration. The drastic decline in the iron incorporation shortly after the maximum concentration may be due to local cooling of the solid ferrocene in the bubbler, caused by the hydrogen carrier gas entering the bubbler at room temperature. With a lower partial pressure, caused by the decreased temperature, the molar flow of the ferrocene drastically decreases, leading to a smaller iron concentration in the grown material.

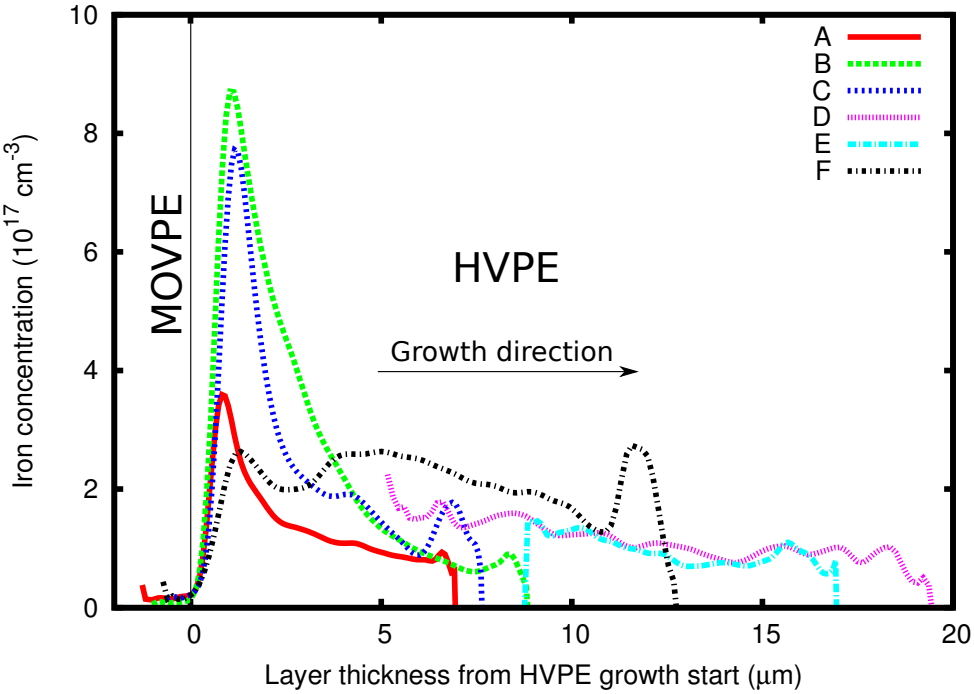

Fig. 5: SIMS profiles of the iron concentration of the samples from Table 2. Samples A–C are grown with different ferrocene molar flows, samples D–F are grown at different growth temperatures (see Table 2). The sample surface is situated at the right end of the measurement curve, the MOVPE-HVPE-GaN interface can be found at the x-axis origin.

In order to prevent this effect, we intend to preheat the carrier gas before it enters the bubbler. As a simple solution we have designed and ordered a gas line coil, that can be placed in the temperature-controlled bath, next to the bubbler. By using this device, the carrier gas will ideally be heated to the temperature of the bubbler.

5. Summary

A ferrocene doping line including a temperature controlled bubbler, a dilution setup, a heated transport line and modified quartz parts to securely transport this source gas species to the growth zone has been designed and put into service at our hydride vapor phase epitaxial machine. First experiments show, that in order to overcome the high unintentional doping levels in our thick GaN layers, we need a rather high ferrocene molar flow for compensation. To achieve the necessary high molar flows, a heated bubbler is essential. Most probably because of the low heat transfer of the powdery ferrocene inside the bubbler, high doping levels can only be achieved in the first few micrometers of ferrocene doped growth before the material is locally cooled down and the mass transport of the ferrocene is limited to a rather small level. In order to overcome this problem, we intend to preheat the carrier gas upstream of the bubbler. An appropriate device has been designed and ordered.

Acknowledgment

I thank T. Meisch, J. Wang, M. Alimoradi-Jazi, D. Heinz and O. Rettig for their continuous effort to supply me with templates. I also thank AIXTRON SE, Aachen for planning and realizing the ferrocene doping line and L. Kirste from the Fraunhofer Institute of Applied Solid State Physics (IAF) in Freiburg for conducting SIMS measurements. This work was financially supported by the German Federal Ministry of Education and Research (BMBF) within the "TeleGaN" project.

References

[1] R. Mitova, R. Ghosh, U. Mhaskar, D. Klikic, M. Wang, and A. Dentella, "Investigations of 600-V GaN HEMT and GaN diode for power converter applications", *IEEE Trans. Power Electron.*, vol. 29, pp. 2441–2452, 2014.

[2] D.S. Lee, J.W. Chung, H. Wang, X. Gao, S. Guo, P. Fay, P. and T. Palacios, "245-GHz InAlN/GaN HEMTs with oxygen plasma treatment", *IEEE Electron Dev. Lett.*, vol. 32, pp. 755–757, 2011.

[3] M. Wu, J.H. Leach, X. Ni, X. Li, J. Xie, S. Dogan, U. Ozgur, H. Morkoc, T. Paskova, E. Preble, K.R. Evans, and C-Z. Lu, "InAlN/GaN heterostructure field-effect transistors on Fe-doped semi-insulating GaN substrates", *J. Vac. Sci. Technol. B*, vol. 28, pp. 908–911, 2010.

[4] F. Lipski, "Semi-insulating GaN by Fe-doping in hydride vapor phase epitaxy using a solid iron source", *Annual Report 2010*, pp. 63–70, Ulm University, Institute of Optoelectronics.

[5] S. Heikman, S. Keller, S.P. DenBaars, and U.K. Mishra, "Growth of Fe doped semi-insulating GaN by metalorganic chemical vapor deposition", *Appl. Phys. Lett.*, vol. 81, pp. 439–441, 2002.

[6] Y. Kumagai, H. Murakami, Y. Kangawa, and A. Koukitu, "Growth and characterization of thick GaN layers with high Fe doping", *Phys. Status Solidi C*, vol. 2, pp. 2058–2061, 2005.

[7] A. Bhattacharjee, A. Rooj, D. Roy, and M. Roy, "Thermal decomposition study of ferrocene [$(C_5H_5)_2Fe$]", *J. Exp. Phys.*, vol. 2014, pp. 513268-1–8, 2014.

[8] M.J.S. Monte, L.M.N.B.F. Santos, M. Fulem, J.M.S. Fonseca, and C.A.D. Sousa, "New static apparatus and vapor pressure of reference materials:â naphthalene, benzoic acid, benzophenone, and ferrocene", *J. Chem. Eng. Data*, vol. 51, pp. 757–766, 2006.

Ordered GaN Nanowires on Nitrogen-Polar GaN

Dominik Heinz

In this work, the position-controlled growth of GaN nanowires on sapphire wafers and on N-polar GaN templates is presented using selective area vapor-liquid-solid growth in a metalorganic vapor phase reactor. Misoriented sapphire wafers and TMIn acting as surfactant are applied in order to achieve N-polar GaN buffer layers with high crystal and surface quality, suitable for a subsequent nano-patterning by electron-beam lithography.

1. Introduction

Gallium nitride (GaN) nanowires find strong interest in academic research due to their potential for future light emitting [1] and sensing [2] devices. While typically the ordered growth of nanowires can be well controlled with molecular beam epitaxy (MBE) [3], selective area epitaxy with metalorganic vapor phase epitaxy (MOPVE) on the nano-scale is still very challenging. Inhomogeneity from wire to wire and inhomogeneous growth of single wires is often observed [4]. Recently, a nanowire growth model based on a vapor-liquid-solid (VLS) process has been reported by Tessarek *et al.* using unpatterned sapphire substrates [5, 6]. Particularly, Ostwald ripening is discussed as one source for inhomogeneous growth of the nanowires in MOVPE [5, 6].

Depending on the growth conditions, GaN-based nanowires can be either grown with gallium- [1] or with nitrogen-polarity [7,8]. Growth in N-polar direction seems to be easier achievable than with Ga-polarity [1]. However, while high quality Ga-polar GaN templates are easily available, there exists a lack of MOVPE grown N-polar GaN buffer layers with high crystal and surface quality. Therefore, mainly structured sapphire substrates [4], polished freestanding GaN [8], or N-polar GaN templates realized in MBE [9] are applied for the nanowire growth. On sapphire, the N-polar GaN growth is achieved by *in-situ* nitridation of sapphire in ammonia (NH_3) ambient at high temperatures [10]. For selective growth of GaN nanowires in MOVPE, mainly two methods are reported in literature. Either a continuous growth [1], or a pulsed growth mode [11] with modulated metalorganic and hydride precusor flows is performed. Typically, small V/III-ratios and additional silane flows [12] are required in order to achieve a vertical growth. Recently, first studies on the diffusion processes occuring during the selective growth of GaN nanowires in MOVPE have been performed by Wang *et al.* [7].

Usually, the nanowire growth conditions are very different from growth conditions applied during nucleation of the wires. For nucleation, increased V/III-ratios, reduced temperatures, and reduced silane flows are applied. Small variations in the mask-patterning on the nano-scale typically have a strong influence on the latter nanowire growth. Additionally, due to charging effects, electron-beam lithography on sapphire is often more difficult

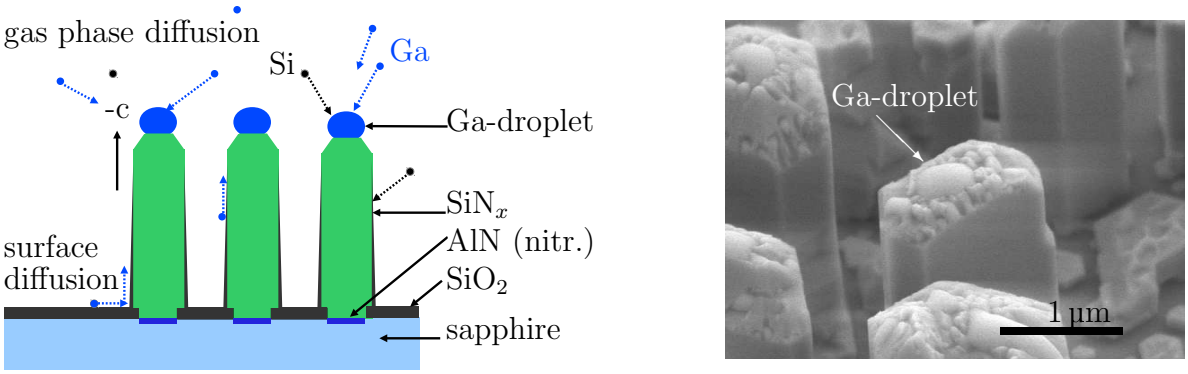

Fig. 1: Schematic illustration of the "selective area" vapor-liquid-solid nanowire growth in MOVPE based on [5] dominated by surface and gas phase diffusion (left). Scanning electron micrograph of GaN microrods on unpatterned sapphire. After cooldown without ammonia [6], Ga-droplets are visible at the tips (right).

than on slightly doped GaN templates. An improved homogeneity and better control during nanowire nucleation is excepted on structured N-polar GaN buffer layers. In recent years, the quality of N-polar MOVPE-GaN templates on sapphire could be significantly improved [13]. Particularly, the application of misoriented sapphire wafers [13] and TMIn acting as surfactant [14] enabled a reduced density of inversion domain boundaries (IDBs).

In this work, the growth of N-polar GaN nanowires on nano-structured N-polar GaN templates is demonstrated and compared to the direct growth on sapphire. In order to reduce Ostwald ripening effects [5, 6] under Ga-rich growth conditions, the application of selective area VLS growth in MOVPE is investigated. A study on the gas phase and surface diffusion processes during nanowire growth with VLS is performed.

2. Experimental

N-polar GaN-nanowire and GaN-template growth is performed in an Aixtron AIX200 MOVPE reactor using ammonia (NH_3), silane (SiH_4), trimethylgallium (TMGa), trimethylindium (TMIn) precursors as well as hydrogen and nitrogen as carrier gases.

For growth of GaN nanowires on sapphire, conventional *c*-sapphire substrates are applied with a miscut of 0.3° towards the *m*-direction. The substrates are covered with a 20 nm thick SiO_2-layer deposited using plasma enhanced chemical vapor deposition (PECVD) and patterned with electron-beam (e-beam) lithography. For e-beam lithography, PMMA 950K is used as resist and a thin layer of germanium is evaporated onto the resist to avoid charging during exposure. After exposure, the germanium is wet chemically removed in diluted H_2O_2 and the resist pattern is tranferred into the SiO_2 using dry etching techniques. Resist residues are removed in oxygen plasma and wet chemically using potassium hydroxide and piranha etching. *In-situ* nitridation of the sapphire is performed in the MOVPE reactor, using nitrogen and ammonia ambient. The selective nanowire nucleation is realized with a V/III-ratio of $\sim$ 200 at $T \sim 950\,^{\circ}\mathrm{C}$ using a hydrogen to nitrogen ratio of $\sim 2:1$. All temperatures are given as process temperatures measured inside the susceptor core. Subsequently, the GaN nanowire overgrowth is performed

with a V/III-ratio of $\sim$ 60 at $T \sim 1100\,^{\circ}\mathrm{C}$ in hydrogen ambient. Additionally, silane ($\sim 70\,\mathrm{nmol/min}$) is applied to promote the vertical growth [1].

For growth of GaN nanowires on N-polar GaN, buffer layers are realized on *c*-plane sapphire wafers with a miscut of 0.3° towards the *m*-direction and compared to layers grown on *c*-plane with 3.5° miscut towards the *a*-direction [13] and *a*-plane sapphire wafers. The sapphire wafers are nitridized and subsequently a N-polar GaN nucleation layer and buffer layer are grown using TMIn as surfactant [14]. For the nucleation layer growth, a high V/III-ratio of $\sim$ 8200 at $T \sim 1020\,^{\circ}\mathrm{C}$ and nitrogen as carrier gas are applied. Buffer layers are realized with a reduced V/III-ratio of $\sim$ 500 at $T \sim 1170\,^{\circ}\mathrm{C}$. Finally, the templates are patterned *ex-situ* using SiO_2 as mask material and electron-beam lithography in accordance with the previously mentioned procedure. A second MOVPE step is carried out and GaN nanowires are selectively grown out of the mask openings without nucleation step.

3. Ordered Growth of N-Polar GaN Nanowires on Sapphire

In order to allow investigations on diffusion processes and local V/III-ratios, the masked substrates are patterned with a hole mask with fields of varying period (1 µm, 2 µm, 5 µm, and 10 µm), but same opening diameter. Scanning electron micrographs of the selectively grown GaN nanowires on sapphire are given in Fig. 2. Unintentional parasitic growth on masked areas can be observed which can be attributed to the Ga-rich growth conditions. The density of the clusters appears to be highest in the areas with smallest period and corresponding smallest mask filling factor. Partly, the clusters can be related to coalescence of neighboring nanowires which mainly appears for small periods. The corresponding larger local V/III-ratio for smaller periods might promote lateral growth of the wires in these regions.

Surprisingly, the height and diameter of the nanowires appears to be to a large extend independent of the filling factor of the mask and the local V/III-ratio. This could be related to the VLS growth mode reported by Tessarek *et al.* [5] which is different than the typically observed selective area growth in MOVPE. During VLS growth, the formation of gallium droplets at the tip of the nanowires is assumed while the side facets of the wires are passivated by Si-compounds [5]. The droplet-formation requires Ga-rich growth conditions, where Ga-atoms from surface and gas-phase diffusion are adsorbed in the droplet. In areas with large filling factor, only Ga-atoms within the surface diffusion length are able to reach the droplet. Adsorbed Ga-atoms at larger distances either desorb back to gas-phase or promote the formation of parasitic growth.

The total amount of deposited GaN per unit area is significantly reduced in areas with large periods. The estimated surface diffusion length is in the range of 1–2 µm [15] which is in good agreement with results obtained by others [7]. Interestingly, most wires have a uniform length of about 1.3 µm which is in good agreement with the estimated diffusion length. Increasing the growth time (not shown) does not increase the length of the wires but promotes cluster formation. As the Ga-droplet at the wire-tip is mainly fed by surface diffusion, droplets can completely desorb if the wires reach a length larger than the surface

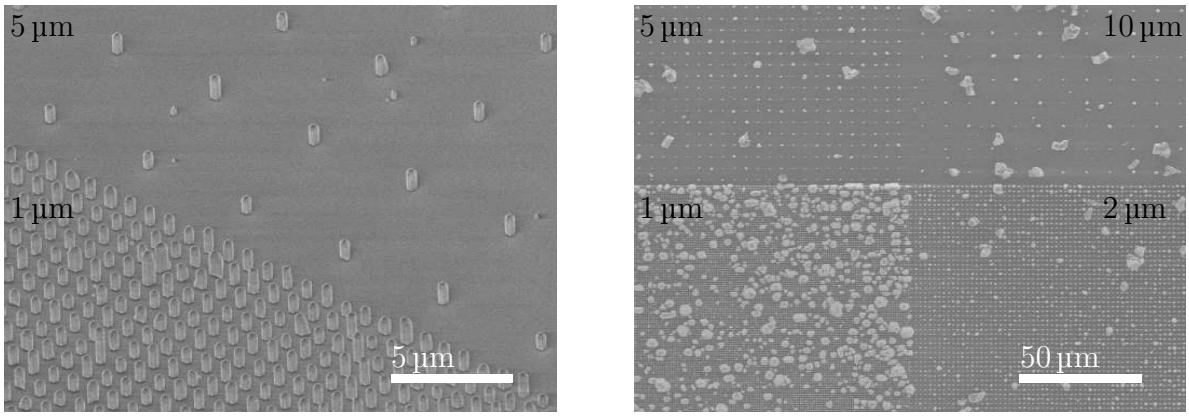

Fig. 2: Scanning electron micrographs of ordered N-polar GaN nanowires on sapphire at the border between the 1 µm and 5 µm period region (left). Density of parasitic GaN clusters with varying mask filling factor (right).

diffusion length. Without Ga-droplet the wires can easily be completely passivated due to the high silane flows and a stop of growth occures. Additionally, due to the VLS growth, Ostwald ripening has to be taken into account [5]. For small periods, accidentally smaller droplets at the tips of the wires can easily desorb and promote the formation of larger neighboring droplets and thereby cluster formation. This phenomenon was also observed for nanowires grown on unpatterned substrates without size-control due to the unavoidable size fluctuations of the droplets [5].

4. Realization of N-Polar GaN Templates

A comparison is made for N-polar GaN grown on different sapphire orientations with varying thickness, carrier gas, and TMIn surfactant flows. While Ga-polar GaN is typically grown on *c*-sapphire wafers, *c*-oriented GaN with good crystal quality can also be realized on *a*-sapphire wafers [16]. According to our knowledge, the growth of N-polar GaN on *a*-plane sapphire and the influence of TMIn acting as surfactant has not been reported in literature. Additionally, the influence of the carrier gas is investigated, e.g., hydrogen is known to result in a strongly reduced lateral growth compared to nitrogen [12]. Particularly, a strong influence on the nucleation and coalescence of the buffer layers is expected.

Optical micrographs of buffer layers grown on *c*-sapphire with 0.3° miscut, *c*-sapphire with 3.5° miscut and *a*-sapphire using nitrogen as carrier gas and 20 µmol/min TMIn are given in Fig. 3. High densities of inversion domain boundaries (IDBs) can be observed for N-polar GaN buffers grown on conventional *c*-plane and *a*-plane sapphire wafers. IDBs are known to result in hexagonal hillock formation during growth which are also clearly visible in the optical micrographs [13]. In contrast, much smaller and fewer hillocks can be observed on the strongly misoriented *c*-sapphire wafers in accordance to findings reported by Keller *et al.* [13]. Pronounced cracks are visible in the N-polar GaN layers on *c*-sapphires with 3.5° miscut caused by tensile strain. All layers are almost completely etched after 10 min in 5M potassium hydroxide solution (KOH) at 80 °C confirming the predominant

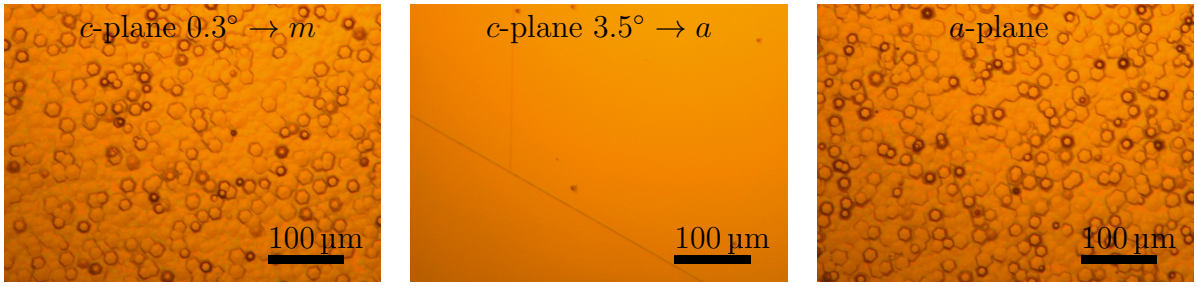

Fig. 3: Optical micrographs of N-polar GaN templates on conventional *c*-sapphire with 0.3° miscut towards *m* (left), *c*-sapphire with 3.5° miscut towards *a* (middle) and *a*-sapphire (right) using nitrogen as carrier gas and 20 µmol/min TMIn surfactant flow.

N-polarity [17] (not shown). For increased TMIn flows (40 µmol/min), smoother layers can be found on conventional *c*- and *a*-plane while a reduced quality is observed on the misoriented *c*-sapphire wafers. In contrast, a lower TMIn flow of 10 µmol/min results in a reduced surface quality on all sapphire wafers (not shown). Using hydrogen instead of nitrogen as carrier gas results in crack-free and almost hillock-free N-polar GaN layers on 2"-substrates. Hall-measurements show an increased unintentional n-type carrier concentration of $n \sim 3 \cdot 10^{19}$ cm^{-3} for layers grown with nitrogen compared to $n \sim 7 \cdot 10^{18}$ cm^{-3} for layers grown with hydrogen as carrier gas. High resolution X-ray diffraction analysis furthermore confirms an improved crystal quality of the N-polar GaN layers grown with hydrogen (see Table 1).

Table 1: Full widths at half maximum of the high resolution (0002) X-ray diffraction rocking curves of N-polar GaN layers grown with nitrogen and hydrogen as carrier gas.

thickness	0.8 µm	1.6 µm
hydrogen	509″	381″
nitrogen	800″	621″

5. Ordered Growth of N-Polar GaN Nanowires on GaN

An homogeneous resist patterning is achieved on N-polar GaN templates with circular openings and diameters of approximately 150 nm (Fig. 4 top, left). Scanning electron micrographs of the selectively grown GaN nanowires are given in Fig. 4. Compared to the mask openings, an increased diameter of about 300 nm can be observed for the hexagonally-shaped wires caused by lateral growth over masked regions. Surprisingly, despite of their N-polarity, the nanowires form semipolar side-facets and a flat *c*-plane like plateau at the tips. In fact, the plateau turns out to be rather circularly-shaped and slightly raised with respect to the semipolar facets. The diameter of the plateau is corresonding to the diameter of the circular mask openings. It is expected that the initial size of the Ga-droplet is mainly determined by the size of the mask openings.

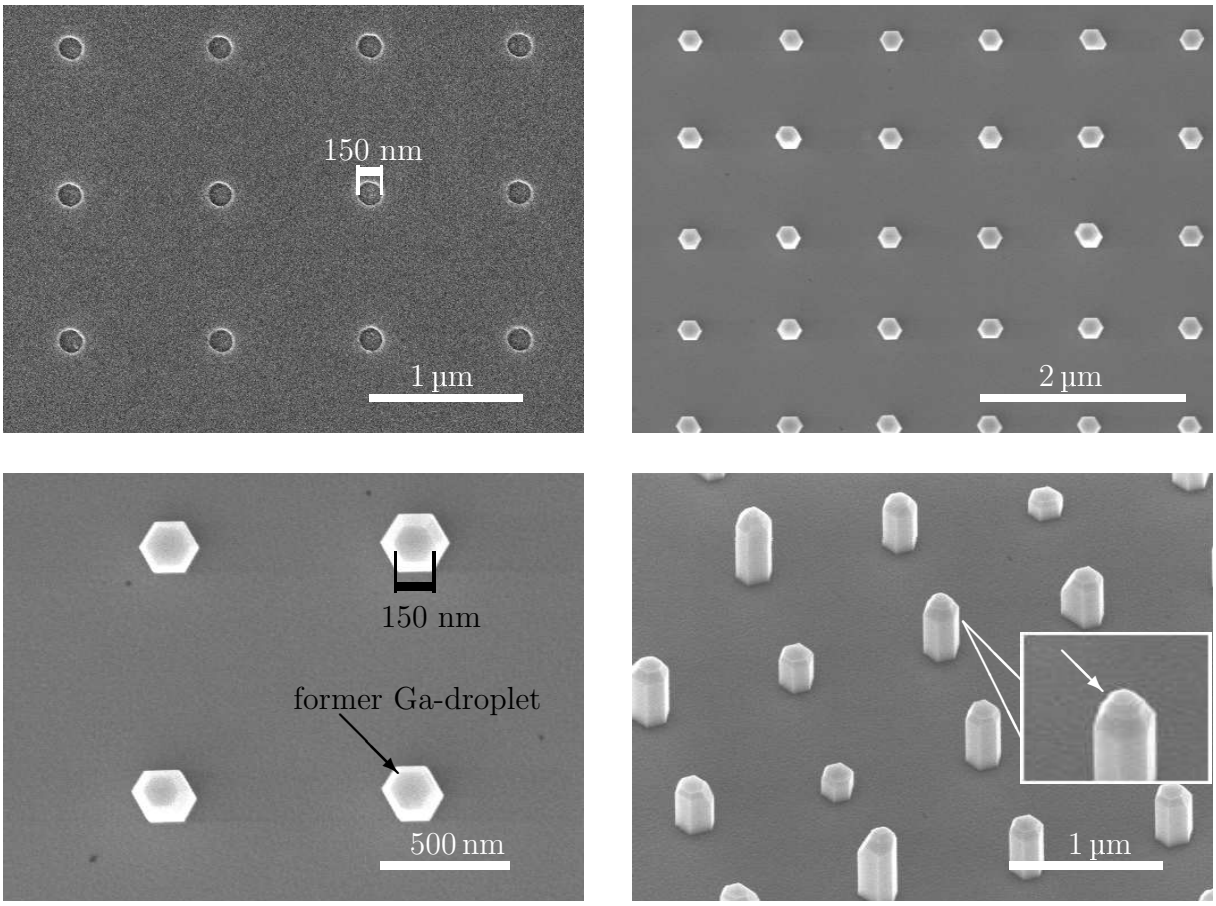

Fig. 4: (top) Scanning electron micrograph of a structured resist on N-polar GaN created by electron beam lithography (left) and corresponding micropraphs of N-polar GaN nanowires with 1 µm periodicity after overgrowth in MOVPE (right); (bottom) indicated positions of the former Ga-droplet (left); height fluctuations and observable hillocks (see white arrow in magnified region) at the nanowire tips (right).

We conclude, that under Ga-rich growth conditions the plateau formation of the nanowires is closely related to the VLS growth mode. Due to the VLS growth, layer-by-layer growth occurs on the *c*-plane like plateau at the tips which are covered by the droplet (compare Fig. 1, left). Occasionally, smaller circular hillocks are visible at the nanowire tip (Fig. 4 bottom, right). These features presumably develop during the final stage of the nanowire growth or even during cooldown due to the nitridation of the deposited Ga-droplet after stopping the Ga-supply. Additionally, height fluctuations can be observed for GaN nanowires grown on the N-polar templates similar to wires grown on sapphire. These fluctuations are likely not resulting from an inhomogeneous mask patterning but might be related to fluctuations in the size of the Ga-droplets. Particularly, Ostwald ripening is known to result in competition between individual droplets for the Ga-supply. Smaller droplets desorb more easily and result in a passivation of the GaN-nanowire at an early stage. Increasing height fluctuations appear more pronounced on the nano-scale and for closely-packet nanowires compared to micrometer-sized rods. This can be explained by the increasing challenge to prevent Ostwald ripening on the nanometer-sized structures.

6. Summary

The ordered realization of N-polar GaN nanowires by a selective area VLS growth in MOVPE was demonstrated. The influence of surface and gas phase diffusion on the nanowire growth was investigated with respect to the mask filling factor. High quality N-polar GaN buffer layers were realized suitable for nano-lithographic processing. Furthermore, a comparison between nanowires grown on structured sapphire substrates and on patterned N-polar GaN templates was performed.

Acknowledgment

Scientific and technical support by O. Rettig, F. Huber, and K. Thonke from the Institute of Quantum Matter / Semiconductor Physics Group (Ulm University) and by R.A.R. Leute, R. Blood, T. Zwosta and R. Rösch from the Institute of Optoelectronics (Ulm University) is gratefully acknowledged. The author thanks S. Jenisch from the Institute of Electron Devices and Circuits (Ulm University) for the electron beam lithography processing. This work was financially supported by the Baden-Württemberg Stiftung gGmbH within the project "Nitridische Nanosäulen für optisch auslesbare Sensoranwendungen".

References

[1] A. Waag, X. Wang, S. Fündling, J. Ledig, M. Erenburg, R. Neumann, M. Al Suleiman, S. Merzsch, J. Wei, S. Li, H.H. Wehmann, W. Bergbauer, M. Straßburg, A. Trampert, U. Jahn, and H. Riechert, "The nanorod approach: GaN NanoLEDs for solid state lighting", *Phys. Status Solidi C*, vol. 8, pp. 2296–2301, 2011.

[2] J. Teubert, P. Becker, F. Furtmayr, and M. Eickhoff, "GaN nanodiscs embedded in nanowires as optochemical transducers", *Nanotechnology*, vol. 22, pp. 275505-1–5, 2011.

[3] H. Sekiguchi, K. Kishino, and A. Kikuchi, "Emission color control from blue to red with nanocolumn diameter of InGaN/GaN nanocolumn arrays grown on same substrate", *Appl. Phys. Lett.*, vol. 96, pp. 231104-1–3, 2010.

[4] S.F. Li, S. Fuendling, X. Wang, S. Merzsch, M.A.M. Al-Suleiman, J.D. Wei, H.H. Wehmann, A. Waag, W. Bergbauer, and M. Strassburg, "Polarity and its influence on growth mechanism during MOVPE growth of GaN sub-micrometer rods", *Cryst. Growth Des.*, vol. 11, pp. 1573–1577, 2011.

[5] C. Tessarek, M. Heilmann, E. Butzen, A. Haab, H. Hardtdegen, C. Dieker, E. Spiecker, and S. Christiansen, "The role of Si during the growth of GaN micro- and nanorods", *Cryst. Growth Des.*, vol. 14, pp. 1486–1492, 2014.

[6] C. Tessarek, M. Bashouti, M. Heilmann, C. Dieker, I. Knoke, E. Spiecker, and S. Christiansen, "Controlling morphology and optical properties of self-catalyzed, mask-free GaN rods and nanorods by metal-organic vapor phase epitaxy", *J. Appl. Phys.*, vol. 114, pp. 144304-1–10, 2013.

[7] X. Wang, J. Hartmann, M. Mandl, M. Sadat Mohajerani, H.H. Wehmann, M. Strassburg, and A. Waag, "Growth kinetics and mass transport mechanisms of GaN columns by selective area metal organic vapor phase epitaxy", *J. Appl. Phys.*, vol. 115, pp. 163104-1–8, 2014.

[8] X.J. Chen, G. Perillat-Merceroz, D. Sam-Giao, C. Durand, and J. Eymery, "Homoepitaxial growth of catalyst-free GaN wires on N-polar substrates", *Appl. Phys. Lett.*, vol. 97, pp. 151909-1–3, 2010.

[9] N.A. Fichtenbaum, C.J. Neufeld, C. Schaake, Y. Wu, M.H. Wong, M. Grundmann, S. Keller, S.P. DenBaars, J.S. Speck, and U.K. Mishra, "Metalorganic chemical vapor deposition regrowth of InGaN and GaN on N-polar pillar and stripe nanostructures", *Jpn. J. Appl. Phys.*, vol. 46, pp. L230–L233, 2007.

[10] N. Grandjean, J. Massies, and M. Leroux, "Nitridation of sapphire. Effect on the optical properties of GaN epitaxial overlayers", *Appl. Phys. Lett.*, vol. 69, pp. 2071–2073, 1996.

[11] S.D. Hersee, X. Sun, and X. Wang, "The controlled growth of GaN nanowires", *Nano Lett.*, vol. 6, pp. 1808–1811, 2006.

[12] S. Li, X. Wang, M.S. Mohajerani, S. Fündling, M. Erenburg, J. Wei, H.H. Wehmann, A. Waag, M. Mandl, W. Bergbauer, and M. Strassburg, "Dependence of N-polar GaN rod morphology on growth parameters during selective area growth by MOVPE", *J. Cryst. Growth*, vol. 364, pp. 149 – 154, 2013.

[13] S. Keller, N.A. Fichtenbaum, F. Wu, D. Brown, A. Rosales, S.P. DenBaars, J.S. Speck, and U.K. Mishra, "Influence of the substrate misorientation on the properties of N-polar GaN films grown by metal organic chemical vapor deposition", *J. Appl. Phys.*, vol. 102, pp. 083546-1–6, 2007.

[14] T. Aisaka, T. Tanikawa, T. Kimura, K. Shojiki, T. Hanada, R. Katayama, and T. Matsuoka, "Improvement of surface morphology of nitrogen-polar GaN by introducing indium surfactant during MOVPE growth", *Jpn. J. Appl. Phys.*, vol. 53, pp. 085501-1–4, 2014.

[15] O. Rettig, *Nitridische Nanosäulen – Design und Wachstum für Sensoranwendungen*, Master Thesis, Ulm University, Ulm, Germany, 2014.

[16] K. Doverspike, L. Rowland, D. Gaskill, and J. Freitas, "The effect of GaN and AlN buffer layers on GaN film properties grown on both c-plane and a-plane sapphire", *J. Electron. Mat.*, vol. 24, pp. 269–273, 1995.

[17] H.M. Ng, W. Parz, N.G. Weimann, and A. Chowdhury, "Patterning GaN microstructures by polarity-selective chemical etching", *Jpn. J. Appl. Phys.*, vol. 42, pp. L1405–L1407, 2003.

Optically In-Well-Pumped Semiconductor Disk Laser With Low Quantum Defect

Alexander Hein and Uwe Brauch *

An in-well pumped InGaAs disk laser emitting at 984 nm is presented. The device is designed to eliminate major loss mechanisms attributed to heat generation in semiconductor disk lasers. An output power of close to 7 W at room temperature is achieved by optical excitation with a fiber-coupled 940 nm diode laser. Strong cooling or the use of heat spreaders with high thermal conductivity is not necessary. For the investigated pump levels, absorptance values of 48 % are realized without pump recycling. The optical output shows no indication of thermal rollover at room temperature, but is limited by the currently available pump power.

1. Introduction

Generating output powers in optically pumped semiconductor disk lasers (OPSDLs) beyond 10 W is essentially possible due to rather strong cooling [1, 2], partially with liquid nitrogen [3], and the use of high thermal conductivity diamond heat spreaders with mm-scale thickness [4, 5]. Another alternative to diminish the temperature rise in the active region is to attach an optically transparent single-crystal diamond or SiC intra-cavity heat spreader on the front face of the semiconductor disk to bypass the thermal resistance of the highly reflective distributed Bragg reflector (DBR) layers on the backside [6–8]. In endorsement of the cited works it should be noted that for a straightforward and ingenuous comparison of OPSDL performance, it is not sufficient to simply relate output power, but more ratios or factors like output power/spot size, coolant temperature/sample temperature, quantum defect, etc. have to be accounted for. However, room temperature operation with an output power of greater than 10 W to date was never reported for devices that are not based on strong cooling or high thermal conductivity heat spreading materials. OPSDLs with output powers beyond 20 W are typically found in the spectral region 980–1180 nm, drawing on the advantages of strained InGaAs quantum wells (QWs) and good carrier confinement with GaAs/GaAsP/AlGaAs barriers. These devices are mostly pumped with high-power 808 nm laser diodes, where the main part of the pump radiation is being absorbed in the barriers surrounding the QWs due to the high absorption coefficient in these materials at the described pump wavelength of ten to few thousand per cm. The advantage is a short absorption depth allowing for designs of thin active regions and single-pass pumping. However, two major disadvantages arise: a relatively large quantum defect (20–35 %) for 980–1180 nm emission and an inhomogeneous carrier distribution in

* Uwe Brauch is with the IFSW (Institut für Strahlwerkzeuge), Universität Stuttgart, Germany

the respective QWs resulting in increased threshold pump powers [9]. Contrary, in in-well pumped (IP) semiconductor disk lasers, the quantum defect can be essentially minimized to about 5 % for the laser structure described here, thus being comparable to or even lower than in Yb:YAG laser systems. Considering the overall system performance, the efficiency of strained InGaAs-QW based pump diodes emitting above 900 nm is by about 5–10 % higher than unstrained AlGaAs/GaAs-QW based diodes, typical for the spectral emission range of 800–850 nm. Moreover, the implementation of fully binary compound (AlAs/GaAs) mirrors does not suffer from absorption of the remaining pump radiation, thus not contributing to the heat load in the device. Calculations in [10] reveal that the quantum defect and pump absorption in the mirror are responsible for roughly 40 % of loss in output power with similar contributions for an OPSDL pumped at 808 nm and an emission around 1025 nm. According to simulations in [11] disadvantages for in-well pumped structures may arise from gain reduction at the lasing energy due to kinetic hole burning and reduction of the pump absorption due to Pauli blocking. However, since efficient IP structures [12] often utilize a top Bragg reflector in order to resonantly increase the absorption, the modal gain for the emission wavelength is also increased as a consequence of the spectral proximity of the laser and pump resonance, thus counteracting both mentioned shortcomings.

2. Laser Design and Setup

The presented structures are grown in reverse order, top mirror—active region—bottom mirror, by molecular beam epitaxy (MBE) on n-doped 350 µm thick GaAs substrates with (100) orientation. The active region consists of two identical resonant periodically arranged QW packages separated by a GaAs spacer. Each QW package contains 4 periods of double $In_{0.16}Ga_{0.84}As$ QWs that are compressively strained. The active region was grown at a reduced thermocouple substrate temperature of 420°C to prevent indium diffusion while a typical growth temperature for the DBRs is 480°C. Similar to the work described in [13] strain compensation of the QWs is achieved by placing tensilely strained GaAsP layers into the barriers separating the QWs. The GaAs spacer is needed to account for the dephasing of the optical field intensities of the emission and the pump wavelength since pump absorption can only take place in the QW and hence, its antinodes need to overlap with the emission field pattern. The top and bottom Bragg reflectors were realized by a 3.5 and a 24.5 pair AlAs/GaAs sequence, respectively, the reflectivity of the latter further increased by a Ti/Au metalization evaporated directly onto the epitaxial surface, providing a reflectivity of > 99.95 % at the center wavelength.

The metalized structures are soldered with indium onto gold-plated copper heat sinks and the substrate is removed via wet-chemical etching. The laser samples are completed with a tantalum pentoxide (Ta_2O_5) coating applied by ion beam sputter deposition. By this, the semiconductor surface (GaAs) with its potentially absorbing surface states can be placed in a node of the laser field. The structure design is depicted in Fig. 1. The pump light is assumed to be unpolarized and regarding the distribution of the pump field intensity there is almost no difference between the TE- and TM-component, so that only the TE-component is displayed.

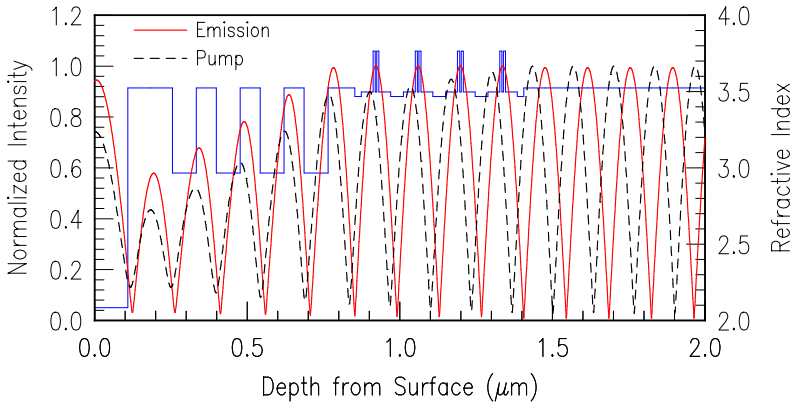

Fig. 1: Refractive index representation of the designed structure and field intensities of the emission and pump (TE-component) wavelength. Displayed is the dielectric coating (Ta_2O_5, $\bar{n} = 2.08$), the top reflector, and the first half of the active region.

Figure 2 shows the measured surface reflectivities for different angles of incidence. Near normal incidence (10° was the smallest possible angle) three dips can be identified within the stop band of the DBR which extends from 925 to 1025 nm. While the excitonic dip at 970 nm remains unchanged with varying angle, the sub-cavity resonances experience the typical cosine shift to shorter wavelengths with an increasing angle of incidence. At 10° the pump and emission resonance are found at 954 nm and 993 nm, respectively, while the latter becomes more pronounced for larger angles as a consequence of a better overlap with the excitonic dip. The detuning between exciton and emission resonance at normal incidence is roughly 24 nm and should promote operation at higher temperatures. The spectral position of the pump resonance follows the same cosine dependence, while the absorption strength shows a linear reduction (increase in reflectivity from 10 % to 20 %) for

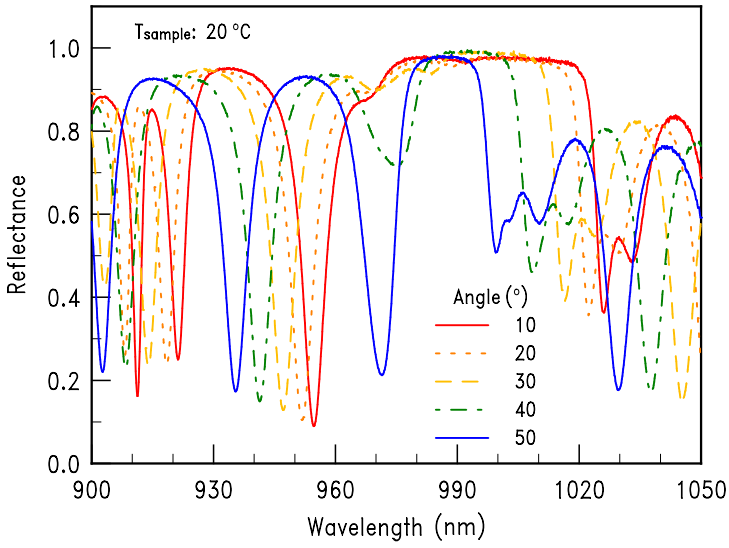

Fig. 2: Reflectivity spectra with varying angles of incidence. Both, laser and pump resonance are visible as pronounced dips in reflector's stop band.

the indicated angles. For pumping with 940 nm diodes and accounting for the temperature dependent spectral shift, the optimum pump angles for a high absorption efficiency are found in the range of 30°–40°.

To characterize the lasing parameters the structures under test were pumped with a fiber-coupled laser diode emitting between 930 and 940 nm depending on the pump current with a maximum output power of roughly 40 W. The beam was focused onto the samples at angles of 24°–26° to give a slightly elliptical spot of $370 \times 420\,\mu m^2$ in the y- and x-axis, respectively. The copper heat sinks were cooled by water of 15°–20°C. A linear resonator with a concave output coupler of −150 mm radius of curvature and transmittance of 2.8 % was used to perform the lasing experiments.

3. Results and Discussion

For high-power operation, care has to be taken to maximize the absorption efficiency of the pump power at the point of operation, e. g., at maximum pump power. This strongly depends on the wavelength of the free-running pump diodes (which is a function of the operating current and cooling-water temperature), the angle of incidence, the temperature of the active region of the disk (which is a function of the absorbed pump power, the heat-sink temperature, and possibly the laser efficiency), and the laser threshold (which is a function of the active-region temperature and the resonator losses, including the outcoupling losses). An example of the absorption efficiency as function of the incident pump power is shown in Fig. 3 for two different devices.

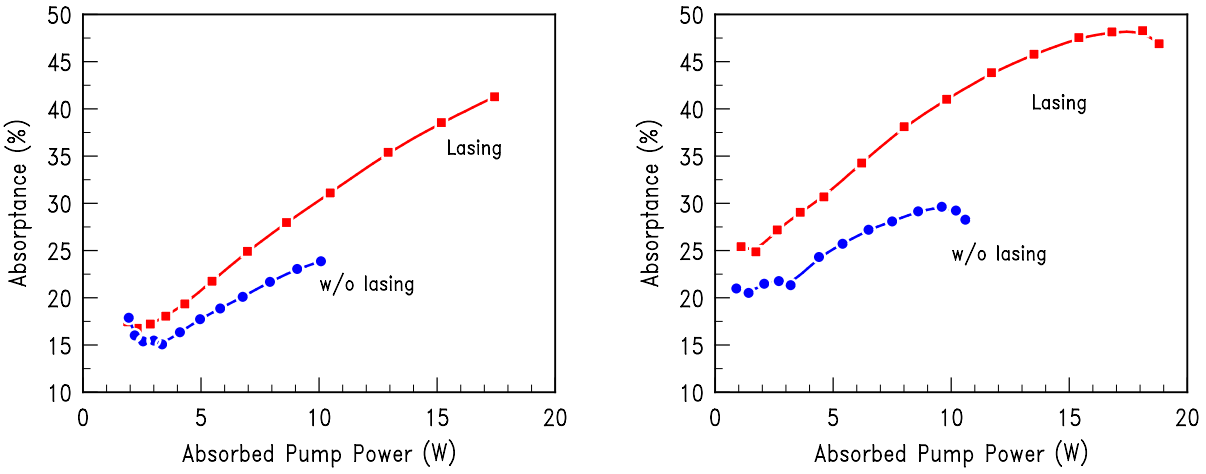

Fig. 3: Absorption efficiency of the pump radiation as function of the incident pump power for two cases: lasing with 2.8 % out-coupling (squares) and not lasing (circles) with out-coupling for two different lasers (left and right).

The absorption increase is mainly due to the shift of the diode laser wavelength into the cavity resonance. The absorption efficiency does not reach the value of 80–90 % one might have expected from the reflectance spectra. This is because with higher population of the upper laser level the wavelength for which the sample is transparent — i.e., the

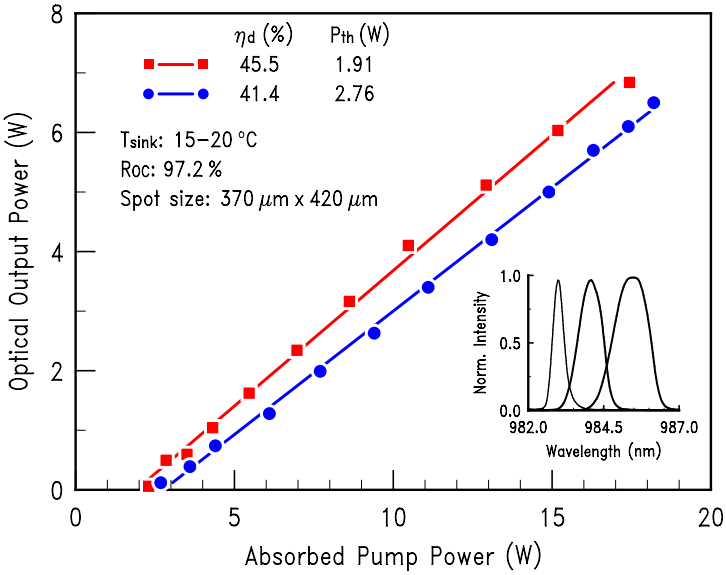

Fig. 4: Laser output power versus absorbed pump power for two devices. The inset shows optical spectra for different excitation levels.

transition from the gain to the absorption region — moves more and more towards shorter wavelengths and finally approaches the pump wavelength. The increase in bleaching is not expected above the lasing threshold where the inversion should be clamped at the threshold value. However, because of heating and other effects this is not strictly true, but the population, and consequently the bleaching, grows significantly slower than under the non-lasing conditions. Laser output power versus absorbed pump power is shown in Fig. 4. The threshold pump power of 2 W corresponds to a power density of 600 W/cm^2, being within a typical range for OPSDLs. The maximum output power, which is limited by the available pump power, is close to 7 W for both devices. The slope efficiency of 45 % is comparable to values typically obtained in barrier pumped structures, but is believed to be limited by the currently relatively poor epitaxial quality of the laser material. The locally resolved photoluminesce of a laser disk is depicted in Fig. 5, where the internal defects can be seen.

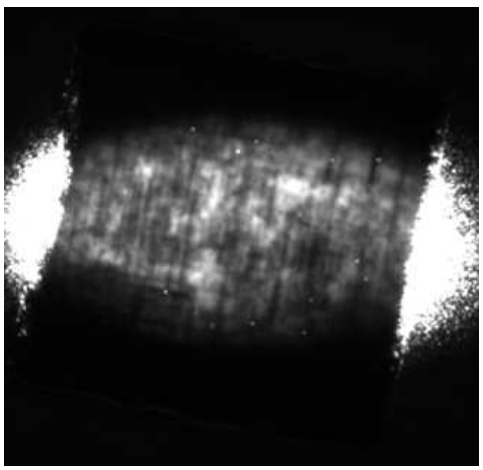

Fig. 5: Locally resolved photoluminescence image of a laser chip. The chip size is approximately $2 \times 2\,\mathrm{mm}^2$. The sample was illuminated with the pump laser diode emitting at 940 nm.

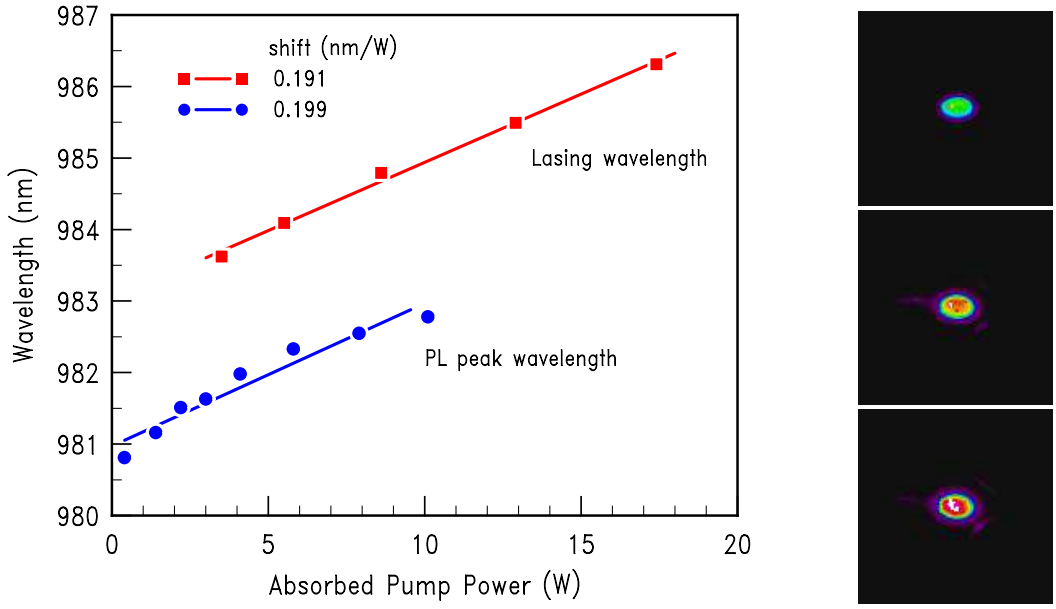

Fig. 6: Lasing wavelength and photoluminecsence wavelength shifts (without outcoupling mirror) versus absorbed pump power (left). Pump spots at different levels of the absorbed pump power (top: 3 W, center: 5.8 W, bottom: 10.1 W) during the PL measurements (right).

Main disadvantage for these devices is the reduced pump absorption. Chosen here was a compromise between absorption efficiency on the one hand and tolerance against misalignment on the other hand. A measured reflectance of roughly 20 % in non-lasing conditions allows to get almost half of the pump power (48 %) been absorbed in one double-pass. With a second double-pass (retro-reflection) one should already get a sufficiently high absorption efficiency (75 %) to realize higher optical outputs. With even more sophisticated pumping schemes, by the use of multipass pump optics, absorptance values comparable to barrier pumped devices (> 90 %) could be easily realized. The in-well pumping scheme allows to operate the laser with almost no sign of thermal rollover despite the relatively simple cooling setup. Using more efficient cooling schemes like diamond heat spreaders should allow to achieve much higher output powers and possibly the regime where a one-dimensional heat flow is sufficient for cooling. This would allow to scale the optical output power freely with the pump-spot size. The results shown here have been achieved with standard diodes without any wavelength stabilization and neither the cooling water for the diodes nor for the laser disk has been stabilized either. Adding volume Bragg gratings (VBGs) to the pump diodes for wavelength stabilization and a temperature controller for the cooling water should further increase the stability of the pump absorption and may even allow to increase the resonance to further enhance the absorption efficiency of one double pass.

The laser wavelength shows a red-shift towards longer wavelengths with 0.191 nm/W; the PL wavelength (without lasing) shifts slightly stronger with 0.199 nm/W absorbed power as depicted in Fig. 6. With a tyical shift of the DBR resonance of 0.07 nm/K this corresponds to a heating of the active layer of 2.73 K/W and 2.84 K/W.

4. Conclusion

In summary, in-well pumped disk lasers emitting at a wavelength of 984 nm with an output power close to 7 W have been demonstrated. The optical output power for this particular type of disk laser is believed to be the highest obtained so far. Thermal rollover is not observed although at maximum output power the laser operates at 9 times of the threshold power while only a simple cooling setup is used. It is likely that with these devices a one-dimensional heat-flow regime may be sufficient for cooling, thus, true power scaling with increasing the pump spot size can become feasible.

Acknowledgment

The authors would like to thank Susanne Menzel for the epitaxial growth of the laser material and Rudolf Rösch for his support with chip processing and mechanical issues.

References

[1] F. Demaria, S. Lorch, S. Menzel, M.C. Riedl, F. Rinaldi, R. Rösch, and P. Unger, "Design of highly efficient high-power optically pumped semiconductor disk lasers", *IEEE J. Select. Topics Quantum Electron.*, vol. 15, pp. 973–977, 2009.

[2] B. Rudin, A. Rutz, M. Hoffman, D.J.H.C. Maas, J.-R. Bellancourt, E. Gini, T. Südmeyer, and U. Keller, "Highly efficient optically pumped vertical-emitting semiconductor laser with more than 20 W average output power in a fundamental transverse mode", *Opt. Lett.*, vol. 33, pp. 2719–2721, 2008.

[3] A. Chernikov, J. Herrmann, M. Koch, B. Kunert W. Stolz, S. Chatterjee, S.W. Koch, T.-L. Wang, Y. Kaneda, J.M. Yarborough, J. Hader, and J.V. Moloney, "Heat management in high-power vertical-external-cavity surface emitting lasers", *IEEE J. Select. Topics Quantum Electron.*, vol. 17, pp. 1772–1778, 2011.

[4] P. Unger, A. Hein, F. Demaria, S. Menzel, M. Rampp, and A. Ziegler, "Design of high-efficiency semiconductor disk lasers", in *Vertical External Cavity Surface Emitting Lasers (VECSELs) III*, J.E. Hastie (Ed.), Proc. SPIE 8606, pp. 860602-1–8, 2013.

[5] B. Heinen, T.-L. Wang, M. Sparenberg, A. Weber, B. Kunert, J. Hader, S.W. Koch, J.V. Moloney, M. Koch, and W. Stolz, "106 W continuous-wave output power from vertical-external-cavity surface-emitting laser", *Electron. Lett.*, vol. 48, pp. 516–517, 2012.

[6] K.-S. Kim, J. Yoo, G. Kim, S. Lee, S. Cho, J. Kim, T. Kim, and Y. Park, "Enhancement of pumping efficiency in a vertical-external-cavity surface-emitting laser", *IEEE Photon. Technol. Lett.*, vol. 19, pp. 1925–1927, 2007.

[7] S. Ranta, M. Tavast, T. Leinonen, N. Van Lieu, G. Fetzer, and M. Guina, "1180 nm VECSEL with output power beyond 20 W", *Electron. Lett.*, vol. 49, pp. 59–60, 2013.

[8] N. Schulz, S. Rösener, R. Moser, M. Rattunde, C. Manz, K. Köhler, and J. Wagner, "An improved active region concept for highly efficient GaSb-based optically in-well pumped vertical-external-cavity surface-emitting lasers", *Appl. Phys. Lett.*, vol. 93, pp. 181113-1–3, 2008.

[9] O. Casel, *Experimentelle Untersuchung und Modellierung des Einflusses der Epitaxiestruktur auf die physikalischen Eigenschaften optisch angeregter Halbleiterscheibenlaser*. Ph.D. Thesis, Technische Universität Kaiserslautern, Germany, 2005.

[10] J. Hader, T.-L. Wang, J.V. Moloney, B. Heinen, M. Koch, S.W. Koch, B. Kunert, and W. Stolz, "On the measurement of the thermal impedance in vertical-external-cavity surface-emitting lasers", *J. Appl. Phys.*, vol. 113, pp. 153102-1–4, 2013.

[11] E. Kühn, S.W. Koch, A. Thränhardt, J. Hader, and J.V. Moloney, "Microscopic simulation of nonequilibrium features in quantum-well pumped semiconductor disk lasers", *Appl. Phys. Lett.*, vol. 96, pp. 051116-1–3, 2010.

[12] S.S. Beyertt, U. Brauch, F. Demaria, N. Dhidah, A. Giesen, C. Kübler, S. Lorch, F. Rinaldi, and P. Unger, "Efficient gallium-arsenide disk laser", *IEEE J. Select. Topics Quantum Electron.*, vol. 43, pp. 869–875, 2007.

[13] A. Hein, S. Menzel, and P. Unger, "High-power high-efficiency optically pumped semiconductor disk lasers in the green spectral region with a broad tuning range", *Appl. Phys. Lett.*, vol. 101, pp. 111109-1–4, 2012.

Electro–Thermal Vertical-Cavity Surface-Emitting Laser Simulation

Markus Daubenschuez

For ongoing optimization of GaAs-based vertical-cavity surface-emitting lasers (VCSELs) it is necessary to predict the current flow and the heat generation of new epitaxial and geometrical designs. To implement a VCSEL model it turned out to be necessary to revisit basic material parameters like the composition, carrier density, and temperature dependencies of the electron and hole mobilities of $Al_xGa_{1-x}As$ semiconductors. In this article we present our quasi-three-dimensional (q3D) electro–thermal device modeling approach and compare the simulation results with current–voltage and wavelength shift measurements.

1. Introduction

VCSELs are established in many technical fields today, in particular optical data communication and sensing [1]. New applications of high-power sources for thermal material treatment or illumination systems are at the horizon. For continuous optimization it is important to have a reliable prediction of the electro–thermal characteristics of such devices and arrays. Several approaches have already been presented in the literature [2–4]. The main difficulty in electrical modeling is the multitude of heterojunctions in the distributed Bragg reflectors (DBRs). It is an extremely demanding task for every commercial semiconductor device simulator to compute the q3D current density distributions and energy band alignments in a full VCSEL. Simplifications are thus necessary.

In Sect. 2 we introduce simple but well suited expressions for the electron and hole mobilities in $Al_xGa_{1-x}As$. We describe the basic scattering mechanisms that limit the mobility of carriers and show comparisons between our model and values given in literature. In Sect. 3 we present the electro–thermal VCSEL simulator, able to handle q3D geometries. We process the whole longitudinal layer structure of a VCSEL with the public domain software SimWindows that gives, among others, spatially resolved carrier density profiles as well as the current–voltage (IV) characteristic. In a further step we combine the data to get a linearized q3D model of the VCSEL itself. The current density distribution inside the entire structure is calculated from the potential profile that is obtained by solving the electrostatic Laplace equation. We then can find the dissipated power density distribution and get the internal temperature profile of the VCSEL. From the calculated temperature profiles we predict the resonance wavelength shifts of the VCSELs which are easily accessible parameters. We show simulation results of VCSEL structures and make comparisons with experimental data.

2. Carrier Mobility

For the simulation of electronic devices, the carrier mobility in the compound semiconductors is one of the key parameters [4]. In the past, quite some effort was put in performing Hall effect measurements [5–8] and provide theoretical descriptions [9] of the carrier mobility. Most of these measurements are in a temperature range irrelevant for practical device applications (typically 77 K) and the theoretical formulations are too complex to use them in a simulation environment. In what follows we describe the most important scattering mechanisms for $Al_xGa_{1-x}As$ and show a combined analytic description of the electron mobility depending on the input parameters temperature, carrier density, and material composition. We show the validity of the formula by comparing the calculated mobilities with experimental data from the literature.

2.1 Scattering mechanisms

The mobility of carriers in a bulk material is defined as

$$\mu = \frac{q}{m_{\text{eff}}} \tau_{\text{sc}} \,, \tag{1}$$

where q is the elementary charge, m_{eff} is the effective mass, and τ_{sc} is the average scattering time. Different scattering effects reduce τ_{sc} and therefore limit the mobility of carriers. The main effects described by Stringfellow [10] are polar optical mode scattering, piezoelectrical scattering, deformation potential scattering, ionized impurity-limited scattering, and space-charge scattering. For electro–thermal simulation we are especially interested in the temperature dependence of the mobility. In the case of ionized impurity-limited scattering we have a relation between the mobility μ_{ii} and the temperature T of the form

$$\mu_{\text{ii}} \propto T^{3/2} \,, \tag{2}$$

causing an increase of μ_{ii} with T due to higher kinetic energy of the carriers. In contrast, all other scattering mechanisms reduce the electron mobility. For instance, the mobility μ_{dp} arising from deformation potential scattering has a proportionality

$$\mu_{\text{dp}} \propto T^{-3/2} \,. \tag{3}$$

This kind of scattering is induced by acoustic phonons which have a larger oscillation for higher temperature. The total scattering in a semiconductor is the sum of all contributions. Thus one can calculate the total mobility μ_{tot} as the reciprocal sum

$$\frac{1}{\mu_{\text{tot}}} = \sum_i \frac{1}{\mu_i} \tag{4}$$

over all individual mobilities μ_i. Figure 1 shows a characteristic mobility curve $\mu_{\text{tot}}(T)$ with contributions of scattering at ionized impurities and deformation potential scattering. These two mechanisms lead to a maximum mobility for a certain temperature.

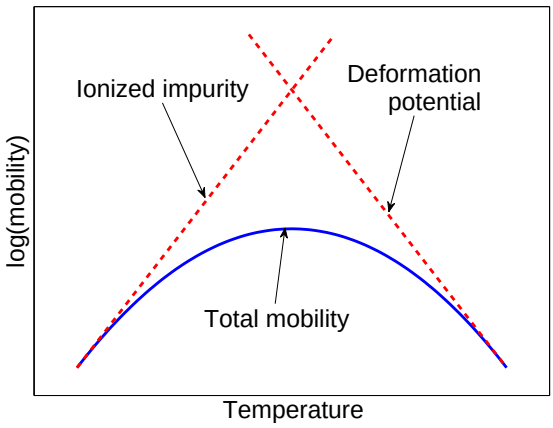

Fig. 1: Total mobility as a function of temperature with two main scattering mechanisms in a semi-logarithmic plot (schematic).

2.2 Electron mobility

To provide a full quantitative model for the electron mobility, one needs to know many material constants like the deformation potentials. One may find these parameters for binary compounds, however, they are hardly available for ternaries. Furthermore one has to describe each scattering mechanism individually. Sotoodeh et al. [11] have developed a low-field Caughey–Thomas-like mobility model for III–V compounds. The model is based on empirical parameters of binary compounds and uses physically justifiable linear interpolations for ternary materials. For our purpose it is convenient to have a single analytical expression for the electron mobility depending on the temperature, the alloy composition, and the carrier density. It should be applicable for practical parameter ranges like temperatures T from 200 to 500 K and electron densities n from $1 \cdot 10^{15}$ to $5 \cdot 10^{18}\,\mathrm{cm}^{-3}$. Therefore we made some simplifications in the parameter set of Sotoodeh's formula which has the form

$$\mu_\mathrm{n}(x,n,T) = \mu_\mathrm{n,min}(x) + \frac{\mu_{\mathrm{n},x} \cdot (300\,\mathrm{K}/T)^{\zeta_\mathrm{n1}(x)} - \mu_\mathrm{n,min}(x)}{1 + \left(\frac{n}{n_\mathrm{ref}(x)\cdot(T/(300\,\mathrm{K}))^{\zeta_\mathrm{n2}}}\right)^{\zeta_\mathrm{n3}(x)}} \tag{5}$$

with the alloy-dependent mobility $\mu_{\mathrm{n},x}$ and the saturated mobility $\mu_\mathrm{n,min}$ for very high n. The electron density at which the mobility reduces to almost half of its maximum value for low doping at a temperature of 300 K is given by n_ref. In contrast to $\mu_\mathrm{n,min}$, $\mu_{\mathrm{n},x}$ and n_ref are temperature-dependent, which is considered by the terms $(300\,\mathrm{K}/T)^{\zeta_\mathrm{n1}}$ and $(T/(300\,\mathrm{K}))^{\zeta_\mathrm{n2}}$. The exponent $\zeta_\mathrm{n2} = 3$ is constant for AlGaAs. All parameters in (5) are listed in Table 1. The dependence of n_ref on the alloy concentration is approximated by [11]

$$n_\mathrm{ref}(x) = (n_\mathrm{ref}(x=0))^{1-x} \cdot (n_\mathrm{ref}(x=1))^{x} \quad . \tag{6}$$

The value of ζ_n1 for different compositions of $\mathrm{Al}_x\mathrm{Ga}_{1-x}\mathrm{As}$ is [11]

$$\zeta_\mathrm{n1}(x) = \frac{(1-x)\zeta_\mathrm{n1}(x=0) + x\zeta_\mathrm{n1}(x=1)}{1+x(1-x)} = \frac{2.1}{1+x(1-x)} \tag{7}$$

Table 1: Fit parameters for the low-field electron mobility after Sotoodeh [11].

Material	$\mu_{\mathrm{n,min}}$ ($\mathrm{cm}^2/(\mathrm{Vs})$)	n_{ref} at 300 K (cm^{-3})	ζ_{n1}	ζ_{n2}	ζ_{n3}
GaAs	500	$6.00 \cdot 10^{16}$	2.1	3	0.394
AlAs	10	$5.46 \cdot 10^{17}$	2.1	3	1.00

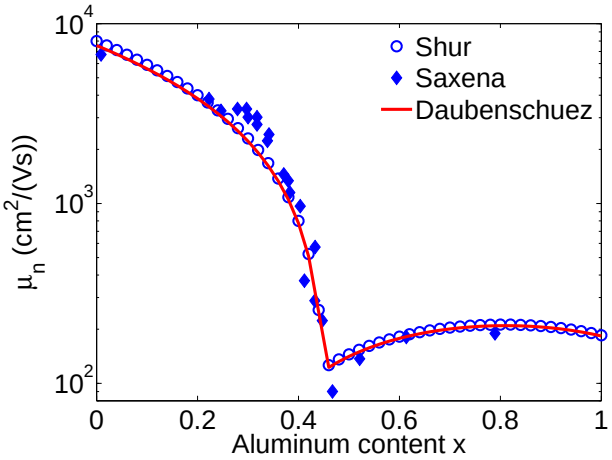

Fig. 2: Electron mobility at $T = 300\,\mathrm{K}$ depending on the fraction x of $\mathrm{Al}_x\mathrm{Ga}_{1-x}\mathrm{As}$ for a free electron density of $n = 5 \cdot 10^{15}\,\mathrm{cm}^{-3}$. Calculated values are compared with Saxena [6] and Shur [12].

according to Table 1. $\zeta_{\mathrm{n3}}(x)$ is linearly interpolated between the values for GaAs and AlAs. The difference between our model and that of Sotoodeh lies in the values for $\mu_{\mathrm{n},x}$ and $\mu_{\mathrm{n,min}}$. To get the typical drop of mobility for $x \approx 45\,\%$ we use the model after Shur [12] as input for $\mu_{\mathrm{n},x}$. In this case, the alloy composition is split into ranges with $x < 0.45$ and $x \geq 0.45$ and $\mu_{\mathrm{n},x}$ is described by the polynomial equations

$$\frac{\mu_{\mathrm{n},x}}{\mathrm{cm}^2/(\mathrm{Vs})} = \begin{cases} 8000 - 22000x + 10000x^2 & \text{for } 0 \leq x < 0.45\,, \\ -255 + 1160x - 720x^2 & \text{for } 0.45 \leq x \leq 1\,. \end{cases} \tag{8}$$

To maintain this mobility drop we decided to change also the linearization of $\mu_{\mathrm{n,min}}$ recommended by Sotoodeh. With a simple linear interpolation between $\mu_{\mathrm{n,min}}(x = 0)$ and $\mu_{\mathrm{n,min}}(x = 1)$ we would overestimate the mobility in the low-mobility range around $x = 45\,\%$. Therefore we choose a small value $\mu_{\mathrm{n,min}}(x = 0.45) = 1$ and linearly interpolate between $\mu_{\mathrm{n,min}}(x = 0)$ and $\mu_{\mathrm{n,min}}(x = 0.45)$ or between $\mu_{\mathrm{n,min}}(x = 0.45)$ and $\mu_{\mathrm{n,min}}(x = 1)$. The calculated room-temperature electron mobilities depending on the alloy composition in Fig. 2 show a good agreement with the experimental data [6] and are nearly congruent with the temperature-independent model by Shur [12]. The results for the temperature and carrier density dependences are shown in Fig. 3. All calculated results are in the uncertainty range of the measurement data found in literature.

However, it should be mentioned that the model has the same limitations as described by Sotoodeh [11]. Additionally our model is limited to a lowest temperature in the range of

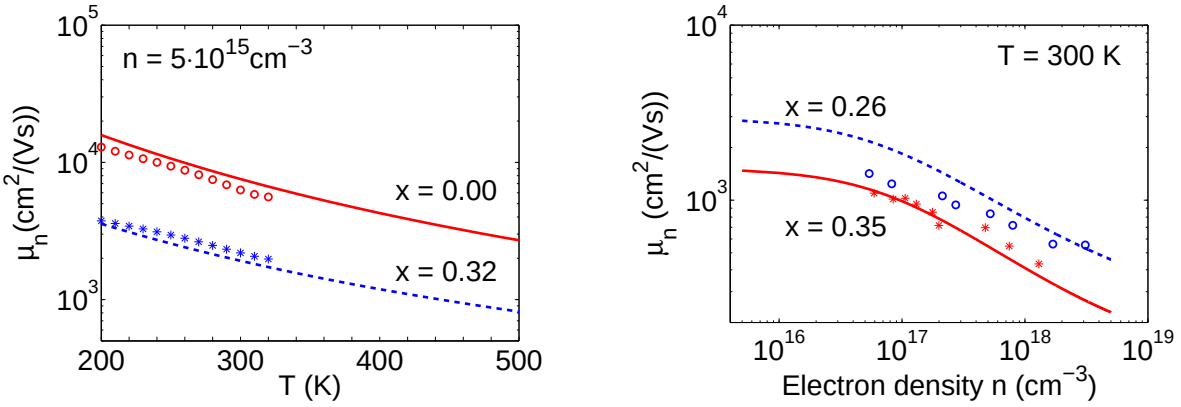

Fig. 3: Calculated (full and dashed lines) electron mobility depending on temperature T (left) and electron density n (right) as well as experimental data (symbols): $x = 0.00$ [7], $x = 0.26$ [8], $x = 0.32$ [6], $x = 0.35$ [8].

200 K. Due to the simplifications made, we do not need to take ionized impurity-limited scattering into account.

2.3 Hole mobility

Like the electron mobility model from the previous section, the model for the hole mobility μ_p is also based on Sotoodeh [11], namely

$$\mu_\mathrm{p}(x,p,T) = \mu_\mathrm{p,min}(x) + \frac{\mu_{\mathrm{p},x}\cdot(300\,\mathrm{K}/T)^{\zeta_\mathrm{p1}(x)} - \mu_\mathrm{p,min}(x)}{1+\left(\frac{p}{p_\mathrm{ref}(x)\cdot(T/(300\,\mathrm{K}))^{\zeta_\mathrm{p2}}}\right)^{\zeta_\mathrm{p3}(x)}} \tag{9}$$

with the alloy-dependent mobility $\mu_{\mathrm{p},x}$ and the saturated hole mobility $\mu_\mathrm{p,min}$ for high hole densities p. All parameters in (9) are listed in Table 2. For computing $\mu_{\mathrm{p},x}$ we use the alloy dependence

$$\mu_{\mathrm{p},x} = 370 - 970x + 740x^2 \tag{10}$$

after Shur [12]. To calculate the saturated mobility, the alloy composition is split into ranges with $x < 0.3$ and $x \geq 0.3$ and therefore $\mu_\mathrm{p,min}$ is described by the linearizations

$$\frac{\mu_\mathrm{p,min}}{\mathrm{cm}^2/(\mathrm{Vs})} = \begin{cases} 20 - 50x & \text{for } 0 \leq x < 0.3\,, \\ 2.857 + 7.142x & \text{for } 0.3 \leq x \leq 1\,. \end{cases} \tag{11}$$

The meaning of p_ref is equivalent to that of n_ref in (5). The values for p_ref and ζ_p3 are calculated with a quadratic interpolation between the data given in Table 2:

$$p_\mathrm{ref}(x) = \left(1.48 - 3.297\cdot x + 5.657\cdot x^2\right)\cdot 10^{17}\,\mathrm{cm}^{-3}\,, \tag{12}$$

$$\zeta_\mathrm{p3}(x) = 0.38 - 0.313\cdot x + 0.421\cdot x^2\,. \tag{13}$$

For ζ_p1 a simple linearized relation

$$\zeta_\mathrm{p1}(x) = 2.2 + 0.04\cdot x \tag{14}$$

Table 2: Fit parameters for the low-field hole mobility after Sotoodeh [11].

Material	$\mu_{\mathrm{p,min}}$ ($\mathrm{cm}^2/(\mathrm{Vs})$)	p_{ref} at 300 K (cm^{-3})	ζ_{p1}	ζ_{p2}	ζ_{p3}
GaAs	20	$1.48 \cdot 10^{17}$	2.2	3	0.38
$Al_{0.3}Ga_{0.7}As$	5	$1 \cdot 10^{17}$			0.324
AlAs	10	$3.84 \cdot 10^{17}$	2.24	3	0.488

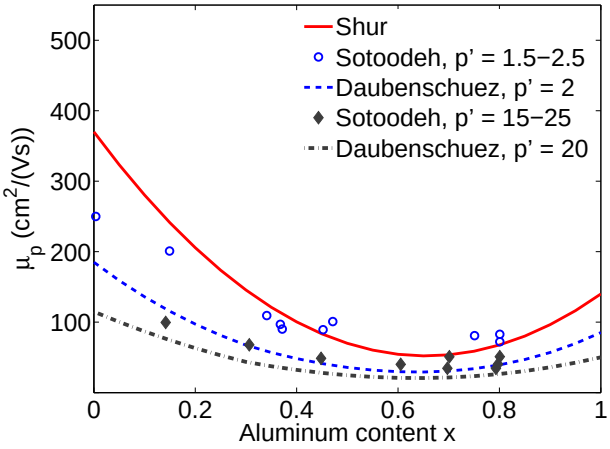

Fig. 4: Hole mobility μ_{p} for different fractions x of $Al_xGa_{1-x}As$ and free hole densities $p = p' \cdot 10^{17}\,\mathrm{cm}^{-3}$ at room temperature. Calculated values are compared with Shur [12] and Sotoodeh [11].

is used. $\zeta_{\mathrm{p2}} = 3$ is assumed for all x. Simulation results for the alloy-dependent mobilities at room temperature are shown in Fig. 4 for different hole densities. The results are compared with measurement data from [11]. Figure 5 shows results for the temperature (left) and carrier density dependence (right). The computed curves are compared with measured data from [13] and [8]. The results are in the uncertainty range of literature data.

3. VCSEL Model

High-power VCSELs are beginning to enable new applications [14, 15]. In parallel there is ongoing research in the more traditional fields of optical data communication and sensing [1]. For continuous optimization it is important to have a reliable prediction of the electro–thermal characteristics of such devices and arrays. In optical data communication, as an example, the constant increase in bandwidth demand requires higher modulation frequencies of the lasers. Neglecting device heating, the resonance frequency ν_{r} can be increased with the injected current I above the threshold current I_{th} according to [16]

$$\nu_{\mathrm{r}} \propto \sqrt{I - I_{\mathrm{th}}}\ .$$

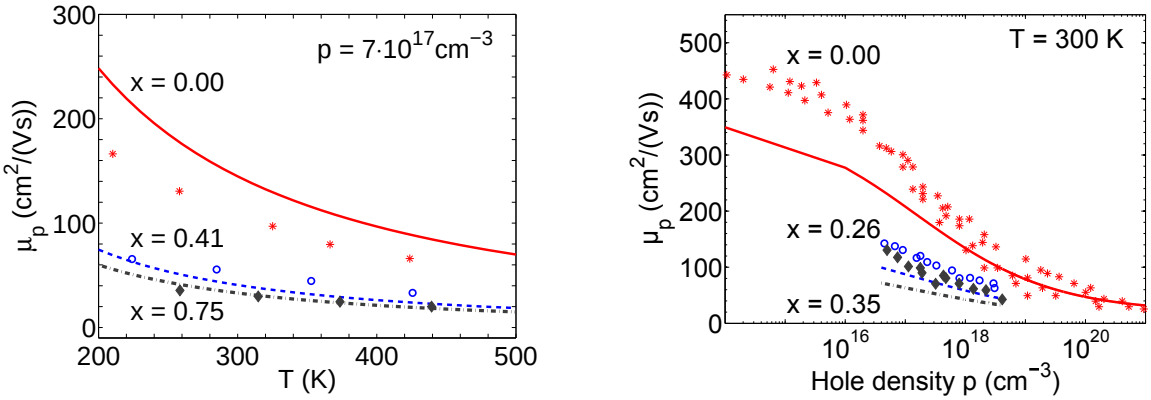

Fig. 5: Calculated (full and dashed lines) hole mobility μ_p depending on temperature T (left) and hole density p (right) as well as experimental data (symbols) from [13] (left) and [8] (right).

In practice, ν_r is limited by thermal effects due to electrical losses in the laser. The motivation behind the simulation model discussed in this paper is the prediction of the electro–thermal behavior of VCSELs and finally the reduction of the dissipated power. In the following we describe the simulation environment that is based on the software SimWindows and a solution of the electrostatic Laplace equation

$$\nabla \cdot \nabla V = 0 \tag{15}$$

with the nabla operator ∇ and the electric potential V as well as of the heat conduction equation

$$\nabla \cdot (\lambda_\mathrm{c} \nabla T) = -p_\mathrm{diss} \tag{16}$$

with the thermal conductivity λ_c and the dissipated power density p_diss.

3.1 Simulation process

All input parameters for the simulation except for the transverse dimensions (active, mesa, and contact diameters) of the oxide-confined VCSELs are given by an epitaxial design file. For each epitaxial layer this file includes the thickness, the alloy gradient, the doping gradient, and the doping material. These parameters are extracted and written into a SimWindows structure definition file.

The 1D energy band alignment is then calculated for the whole structure with the software SimWindows [17], which is a semiconductor device simulation tool that works by solving the semiconductor equations in one dimension. The software thus assumes that all variables such as electron current density j_n, hole current density j_p, electric potential, etc. vary parallel to the flow direction of the current but are uniform in the perpendicular direction. Current continuity $j_\mathrm{n} + j_\mathrm{p} = \mathrm{const}$ is fulfilled. To handle heterojunctions it has a built-in model based on thermionic emission and tunneling currents. To include the temperature dependencies, we have extended the material database of SimWindows by the electron and hole mobility models introduced in Sect. 2. The energy band calculation is done for different material temperatures and voltages between the contacts. Thus we

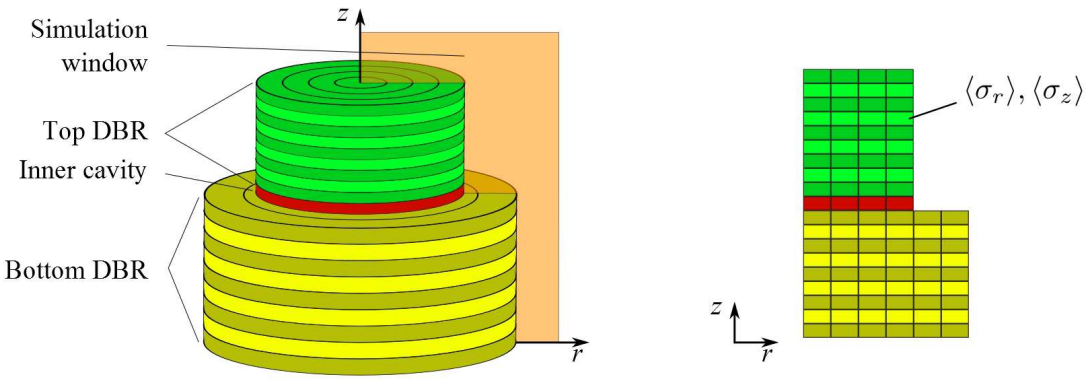

Fig. 6: Calculation plane for the VCSEL simulation (left) and discretization mesh (right).

derive a temperature-dependent longitudinal 1D current–voltage (IV) characteristic of the whole structure. From such an IV characteristic we can derive an average conductivity $\langle\sigma_z\rangle$ for each discretization step in longitudinal z-direction by taking the current density through the whole structure and the voltage drop over each discretization element into account. SimWindows also provides the local carrier densities and mobilities on a user-defined grid with, e.g., 1 nm step width. From those data we calculate a local conductivity $\sigma(z) = q\,(n(z)\cdot\mu_\mathrm{n}(z) + p(z)\cdot\mu_\mathrm{p}(z))$. For in-plane current transport that is not impeded by heterojunctions, we transform the various $\sigma(z)$ into an average conductivity $\langle\sigma_r\rangle$ of the actual discretization block according to a parallel circuit of ohmic resistors.

From the derived data $\langle\sigma_z\rangle$ and $\langle\sigma_r\rangle$ we build a q3D model of the VCSEL. We exploit rotational symmetry and consider only an $(r,\,z)$-plane, as shown in Fig. 6. The plane is divided into segments in lateral r- and vertical z-direction with the discretization widths Δr and Δz.

Once the model of the VCSEL is established, we start the calculation by applying a voltage between the contacts. The following steps are taken iteratively:

1. Solve (15) equivalent to the approach described in [18] to get the potential distribution $V(r, z)$ inside the device.
2. Get the current density and dissipated power density profiles using $\langle\sigma_r\rangle$ and $\langle\sigma_z\rangle$.
3. Take photon cooling in the quantum wells into account.
4. Solve (16) with a fixed heat sink temperature to find $T(r, z)$.
5. Adapt the electric and thermal conductivity values using $T(r, z)$ from step 4.

Those five steps are iterated for each voltage until the total current I converges.

3.2 Simulation results

We now present some results obtained with the described model. Figure 7 shows the electric potential and temperature profiles of a VCSEL with 6.5 µm active diameter. A voltage of 2 V is applied to the top ring contact of the VCSEL at $z = 0\,\mu\text{m}$. The epitaxial layer stack and the substrate have thicknesses of 8.86 µm and 120 µm, respectively. The top mesa diameter is approximately 27.5 µm and the n-DBR region has a diameter of 100 µm. The figures show only the inner part of the VCSEL. The n-contact of the laser is at the back side of the substrate at $z = 128.86\,\mu\text{m}$. Outside the semiconductor material, the electric conductivity is zero and the potential is set to an arbitrary value of -1 V. The top mesa is surrounded by polyimide with a thermal conductivity $\lambda_c = 0.445\,\text{W}/(\text{m}\cdot\text{K})$. As intended, the oxide aperture is strictly blocking the current flow that is perpendicular to the equipotential lines. The main voltage drop obviously occurs over the pn-junction of the active region. The right graph displays the temperature profile for a dissipated power of $P_{\text{diss}} = 9.6\,\text{mW}$. The heat sink is on the back side of the substrate and has a constant temperature of 300 K. No heat flow is assumed across all other surfaces. The maximum temperature increase is $\Delta T_{\text{max}} = 26.14\,\text{K}$ close to the oxide aperture. The corresponding non-averaged thermal resistance of this device thus amounts to $\Delta T_{\text{max}}/P_{\text{diss}} = 2.72\,\text{K/mW}$.

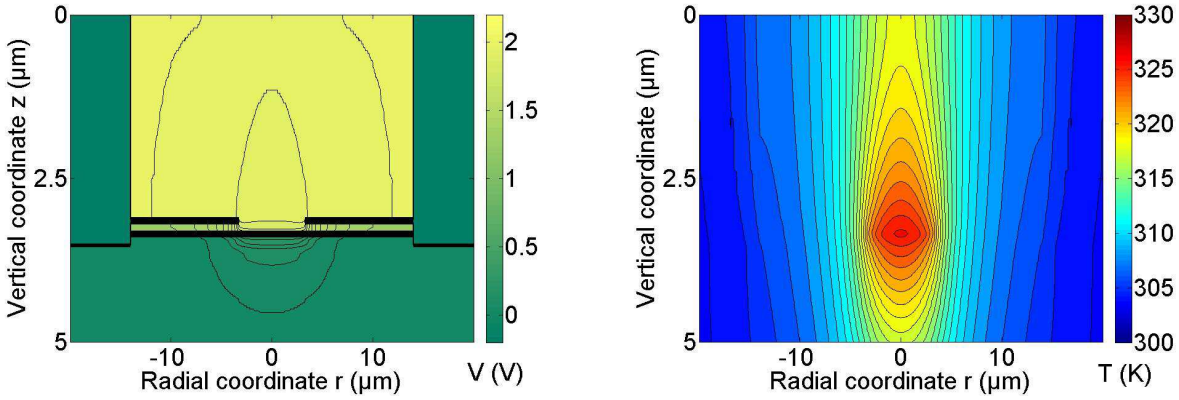

Fig. 7: Simulated electric potential profile $V(r, z)$ (left) and temperature profile $T(r, z)$ (right) of a VCSEL test structure. The oxide aperture is located at $z \approx 3.12\,\mu\text{m}$.

To check the validity of the electro–thermal model we compare it with experimental data of 850 nm GaAs-based VCSELs grown and fabricated by Philips (U-L-M Photonics). First we determine the IV curves of the VCSEL structure described above with two different active diameters D_a. The experimental data in Fig. 8 show excellent agreement with the simulations. A current density distribution $j_z(r, z)$ is also depicted for illustration. The results are obtained without adjustable parameters. We confirm the validity of the approach also via a comparison of the emission wavelength shift as a function of the dissipated power in Fig. 9 for different ambient temperatures T_a. Here, the temperature profile that acts on the refractive indices is weighted by the resonant mode pattern with optical transfer matrix calculations.

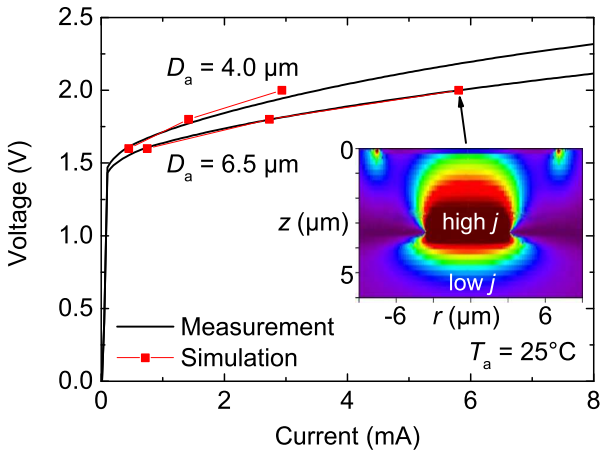

Fig. 8: Simulated and measured IV characteristics for $T_\mathrm{a} = 25°\mathrm{C}$ heat sink temperature and two different active diameters D_a. The inset shows the longitudinal current density distribution $j = j_z$ for $V = 2\,\mathrm{V}$, $D_\mathrm{a} = 6.5\,\mu\mathrm{m}$, and $T_\mathrm{a} = 25°\mathrm{C}$.

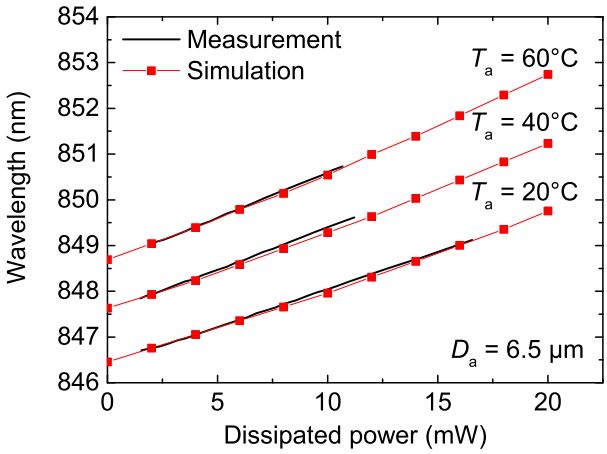

Fig. 9: Dissipated-power-dependent thermal wavelength shifts of a VCSEL with $D_\mathrm{a} = 6.5\,\mu\mathrm{m}$ for various T_a.

4. Conclusion

In this article we have introduced a pragmatic approach to q3D electro–thermal VCSEL simulations employing a proven 1D semiconductor solver. The strong variations of the electron and hole mobilities with composition, temperature, and electron density required to extend the material database of SimWindows with a modified mobility model. The electrical and thermal simulations correspond very well to experimental data. In future we will extend the simulation tool with a simple optical model to take photon cooling and absorption more accurately into account.

Acknowledgment

We would like to thank Dr.-Ing. Philipp Gerlach and Dipl.-Ing. Roger King from Philips Technologie GmbH (U-L-M Photonics) for fruitful discussions and the provision of VCSEL samples. We are grateful to the German Federal Ministry of Education and Research (BMBF) for funding the HyPOT project.

References

[1] R. Michalzik (Ed.), *VCSELs — Fundamentals, Technology and Applications of Vertical-Cavity Surface-Emitting Lasers*. Berlin: Springer, 2013.

[2] S.F. Yu, *Analysis and Design of Vertical Cavity Surface Emitting Lasers*. Hoboken: John Wiley & Sons, 2003.

[3] P. Debernardi, "Three-Dimensional Modeling of VCSELs", Chap. 3 in *VCSELs*, R. Michalzik (Ed.), pp. 77–117. Berlin: Springer, 2013.

[4] J. Piprek, *Semiconductor Optoelectronic Devices*. San Diego: Academic Press, 2003.

[5] S. Adachi, *Properties of Aluminium Gallium Arsenide*. London: INSPEC, 1993.

[6] A.K. Saxena, "Electron mobility in $Ga_{1-x}Al_xAs$", *Phys. Rev. B*, vol. 24, pp. 3295–3302, 1981.

[7] G. Stillman, C. Wolfe, and J. Dimmock, "Hall coefficient factor for polar mode scattering in n-type GaAs", *J. Phys. Chem. Solids*, vol. 31, pp. 1199–1204, 1970.

[8] W.C. Liu, "Investigation of electrical and photoluminescent properties of MBE-grown $Al_xGa_{1-x}As$ layers", *J. Material Sci.*, vol. 25, pp. 1765–1772, 1990.

[9] H.S. Bennett, "Majority and minority electron and hole mobilities in heavily doped gallium aluminium arsenide", *J. Appl. Phys.*, vol. 80, pp. 3844–3853, 1996.

[10] G. Stringfellow, "Electron mobility in $Al_xGa_{1-x}As$", *J. Appl. Phys.*, vol. 50, pp. 4178–4183, 1979.

[11] M. Sotoodeh, A.H. Khalidan, and A.A. Rezazadeh, "Empirical low-field mobility model for III-V compounds applicable in device simulation codes", *J. Appl. Phys.*, vol. 87, pp. 2890–2900, 1999.

[12] M. Shur, *Physics of Semiconductor Devices*. Englewood Cliffs: Prentice Hall, 1990.

[13] J.J. Yang, W.I. Simpson, and L.A. Moudy, "Hole Hall mobility versus temperature". Web page: http://www.ioffe.ru/SVA/NSM/Semicond/AlGaAs/hall.html; last visited Feb. 2015.

[14] J.F.P. Seurin, "High-Power VCSEL Arrays", Chap. 8 in *VCSELs*, R. Michalzik (Ed.), pp. 263–290. Berlin: Springer, 2013.

[15] H. Moench, R. Dumoulin, S. Gronenborn, X. Gu, G. Heusler, J. Kolb, M. Miller, P. Pekarski, J. Pollmann-Retsch, A. Pruijmboom, and M. Stroesser, "Design of high power VCSEL arrays", in *Vertical-Cavity Surface-Emitting Lasers XVI*, C. Lei and K.D. Choquette (Eds.), Proc. SPIE, vol. 8276, pp. 82760B-1–8, 2012.

[16] R. Michalzik, "VCSEL Fundamentals", Chap. 2 in *VCSELs*, R. Michalzik (Ed.), pp. 19–75. Berlin: Springer, 2013.

[17] D.W. Winston, *Physical Simulation of Optoelectronic Semiconductor Devices*. Ph.D. Thesis, University of Colorado, Boulder, CO, USA, 1990.

[18] P. Gerlach, M. Peschke, C. Hanke, B.K. Saravanan, and R. Michalzik, "High-frequency analysis of laser-integrated lumped electroabsorption modulators", *IEE Proc.-Optoelectron.*, vol. 152, pp. 125–130, 2005.

Vertical-Cavity Surface-Emitting Lasers With Record-High Birefringence

Tobias Pusch

Using the elasto-optic effect we increase the frequency difference between the two orthogonally polarized modes, the so-called birefringence, in standard single-mode oxide-confined GaAs-based vertical-cavity surface-emitting lasers (VCSELs). The birefringence may play an important role in the realization of ultra-fast polarization modulation for high-speed data transmission.

1. Introduction

VCSELs are used extensively today as transmitters in high-speed optical interconnects. A first generation of 28 Gbit/s devices is currently being deployed. Although digital modulation at about 50 Gbit/s has been shown [1], it is very unlikely that 100 Gbit/s signals can be generated by direct current modulation. New approaches must thus be explored to satisfy the future demand for higher data throughput. In that sense, the birefringence, i.e., the frequency difference between the two orthogonally polarized components of a VCSEL mode, may play an important role. It has been demonstrated that by optical spin injection a birefringent VCSEL can be excited to oscillations in the degree of circular polarization [2]. The oscillation frequency is very close to the birefringence. The generation of extremely fast polarization bursts is also possible [2]. It is thus of interest to tailor VCSELs to exhibit a maximum amount of birefringence. Contributions to the birefringence are geometrical anisotropies, the electro-optic effect in the cavity, and incorporated strain [3], where the latter is the strongest.

2. Generation of High Birefringence

To get a high birefringence we manipulate the lattice structure of a VCSEL via mechanically induced stress. With this technique, Panajotov et al. [3] have shown that it is possible to increase the birefringence up to 80 GHz. To reach a maximum effect, the VCSEL should be bent in a direction coinciding with one of the two preferred polarization directions. Such bending changes the crystal structure of the VCSEL in one direction, which results in an anisotropic change of the refractive index $\bar{n}$. This is known as the elasto-optic effect. A modified $\bar{n}$ is seen as a change in the emission wavelength λ. From the resonance condition of the laser one expects $\Delta\lambda = \lambda \cdot \Delta\bar{n}/\bar{n}$ or $\Delta\nu = \nu \cdot \Delta\bar{n}/\bar{n}$ for the oscillation frequency $\nu = c/\lambda$ with the vacuum velocity of light c.

Another approach was shown by Jansen van Doorn et al. [4], namely an external heat source can be used to manipulate the birefringence. In this case a Ti-sapphire laser beam is focused close to the VCSEL and the induced heat deforms the crystal structure. The change of birefringence (less than 3 GHz in [4]) is substantially smaller compared to the use of a mechanical bending device due to the much lower induced stress.

3. Experimental Results

To increase the birefringence beyond 100 GHz we employ a custom-made bending device sketched in Fig. 1. It ensures an exact positioning of the VCSEL sample.

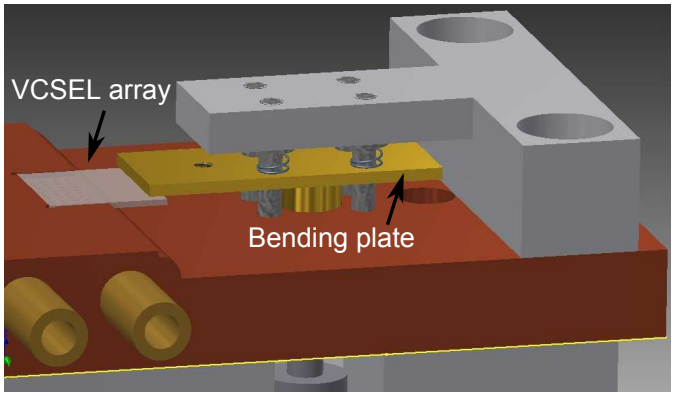

Fig. 1: Drawing of a bending device with bending plate and VCSEL array sample (after [5]).

The sample is a VCSEL array of $10 \times 10\,\mathrm{mm}^2$ size which can be fixed via vacuum in a slot. The bending plate is in a stable horizontal position and can be moved up and down by a micrometer screw. We use a contact current measurement to verify the starting point, just before bending. With this defined starting point and the known step size of the micrometer screw, the bending distance is well under control. In combination with the wavelength difference which we obtain from the spectral measurements we can determine the relation between birefringence and bending distance. For our measurements we contact one VCSEL and bend the sample (grown on (100)-oriented GaAs) along the $[0\bar{1}\bar{1}]$ or $[01\bar{1}]$ crystal direction with a step size of 10 µm. For every step we measure the light–current–voltage (LIV) curves and the optical spectrum. At the end of the measurement series we rotate the VCSEL array by 90°, contact the same device and repeat the procedure by bending along the other crystal direction.

A single VCSEL on the sample with both crystal directions marked is depicted in Fig. 2 (left). Scratches on the bondpad originate from the contact needle. The ground contact is at the bottom of the GaAs substrate. Figure 2 (right) displays the LIV curves of the standard single-mode oxide-confined VCSEL with about 4 µm active diameter. The threshold current and voltage are 0.54 mA and 1.84 V, respectively. An optical output power of 1 mW is reached at about $I = 2\,\mathrm{mA}$ current. The higher-order transverse mode is suppressed by $\approx 37\,\mathrm{dB}$ at $I = 2.1\,\mathrm{mA}$. With the measured wavelength difference in the spectra taken without a polarizer we can calculate the frequency difference $\Delta\nu$, which is equal to the birefringence $B = \Delta\nu$.

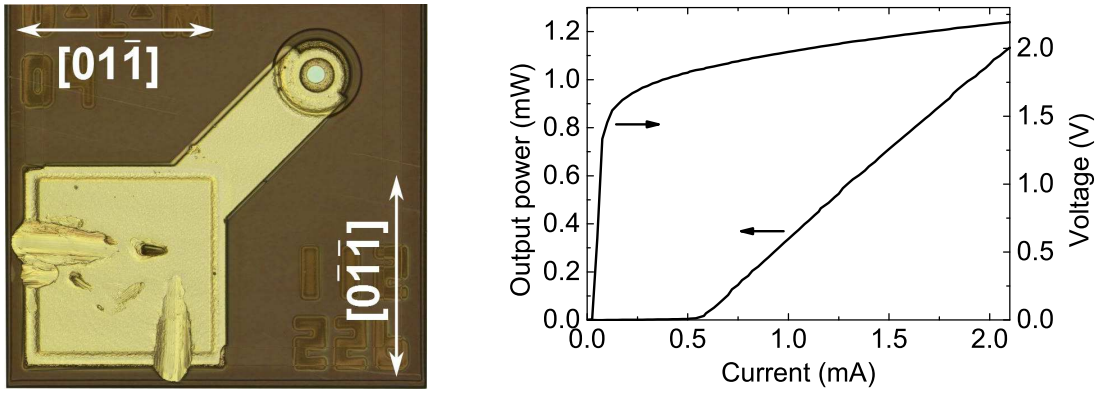

Fig. 2: VCSEL chip with an $80 \times 80\,\mu m^2$ size bondpad and the output aperture in the upper right corner. [01$\bar{1}$] and [0$\bar{1}\bar{1}$] are the crystal directions and preferred polarization directions (left). Operation curves of the VCSEL under investigation (right).

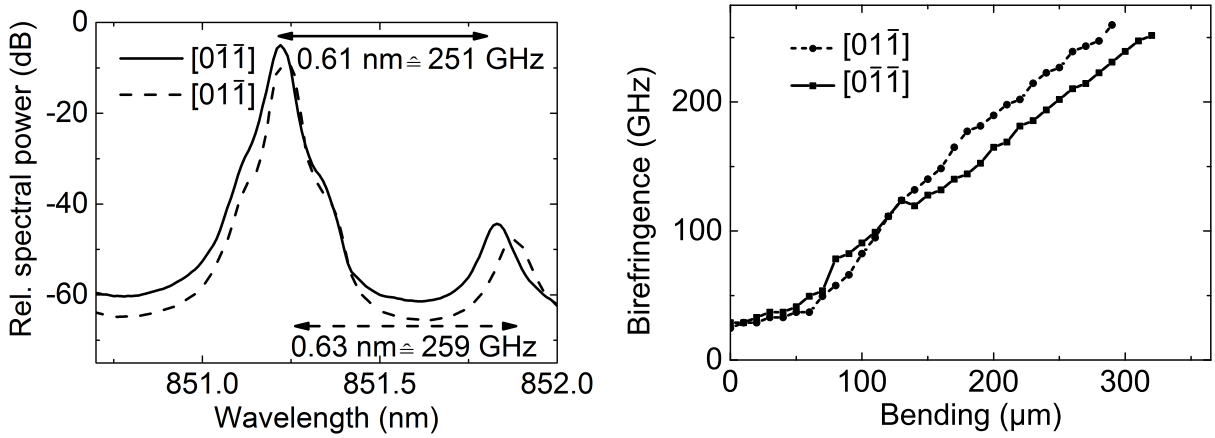

Fig. 3: Spectra of the fundamental mode (at $I = 2.1\,mA$) for maximum bending in the [0$\bar{1}\bar{1}$] and the [01$\bar{1}$] crystal directions. Birefringence versus applied bending in both crystal directions (right).

In Fig. 3, the spectra of the fundamental mode under maximum bending and the relation between bending distance and birefringence are shown. The spectra look similar for both bending directions. We have reached a birefringence of 259 GHz for bending along the [01$\bar{1}$] crystal direction with a maximum bending distance $\hat{L}_b$ of 290 µm and $B = 251\,GHz$ for the [0$\bar{1}\bar{1}$] crystal direction with $\hat{L}_b = 320\,\mu m$. The measured birefringence is more than a factor of three higher than the previous record [3]. There is an approximately linear relationship between birefringence and bending distance in Fig. 3 (right). This behavior is similar for both crystal directions. The second measurement (in [01$\bar{1}$] direction) after rotating the sample has only $\hat{L}_b = 290\,\mu m$. At this point the sample broke into two pieces.

4. Conclusion

With an experimentally obtained value of more than 250 GHz, we have shown that it is possible to increase the birefringence of a VCSEL via mechanically induced stress far

beyond the previous record. The planned experiments in collaboration with the group of Dr. N.C. Gerhardt and Prof. M.R. Hofmann at Ruhr University Bochum [2] will show if spin-induced oscillations in the degree of circular polarization with correspondingly high frequencies can be induced.

5. Acknowledgment

The author thanks Rudolf Rösch and Willi Kogler for fruitful discussions and technical support and Johannes Bläsi for the construction of the bending device. Furthermore the author is grateful to Philips Technologie GmbH (U-L-M Photonics) for the provision of the VCSEL sample. This work is funded by the German Research Foundation.

References

[1] D.M. Kuchta, A.V. Rylyakov, C.L. Schow, J.E. Proesel, C.W. Baks, P. Westerbergh, J.S. Gustavsson, and A. Larsson, "A 50 Gb/s NRZ modulated 850 nm VCSEL transmitter operating error free to 90°C", *J. Lightwave Technol.*, vol. 32, pp. 1–11, 2014.

[2] N.C. Gerhardt and M. Hofmann, "Spin-controlled vertical-cavity surface-emitting lasers", *Advances in Optical Technol.*, article ID 268949, pp. 1–15, 2012.

[3] K. Panajotov and F. Prati, "Polarization Dynamics of VCSELs", Chap. 6 in *VCSELs*, R. Michalzik (Ed.), pp. 181–231. Berlin: Springer, 2013.

[4] A.K. Jansen van Doorn, M.P. van Exter, and J.P. Woerdman, "Strain-induced birefringence in vertical-cavity semiconductor lasers", *IEEE J. Quantum Electron*, vol. 34, pp. 700–706, 1998.

[5] J. Bläsi, *Untersuchung des Doppelbrechungs- und Polarisationsverhaltens bei Vertikallaserdioden unter mechanischer Verspannung*. Bachelor Thesis, Ulm University, Ulm, Germany, 2014.

Optical and Electrical Investigations on GaAs-Based Phototransistors

Sven Bader and Andreas Ziegler

In order to exploit the potential of phototransistors for vertical-cavity surface-emitting laser (VCSEL) applications, optical and electrical investigations on GaAs-based devices were conducted. The characterization of phototransistors consists of measurements and improvements of the current gain and studies on the spectral behavior. In addition, the influences of various doping concentrations and different device structures, such as resonant-cavity-enhanced phototransistors, will be introduced and discussed.

1. Introduction

The detection of infrared signals in optical fiber communication is one of the most quoted applications for phototransistors [1]. High optical gain without excess noise is a potential advantage over the competitive device, the avalanche photodiode [2]. Phototransistors combine the functions of photodiodes and bipolar transistors. Hence, the structure of the device is similar to a common npn- or pnp-bipolar transistor, which consists of emitter, base and collector layers. In this article, we investigate exclusively the pnp structure. To achieve high current gain, it is necessary to integrate a heterojunction, thus a potential barrier, between the p-emitter and n-base layers, equivalent to a heterojunction bipolar transistor (HBT). According to this, the device is similarly named heterojunction phototansistor (HPT). With an HPT it is possible to reach current gains between 10^2 and 10^5 [3]. The photodetection occurs in the depletion zone of the n-base and p-collector junction due to the photoeffect. In more special cases, there is a separate absorption layer with defined width d and absorption coefficient α embedded between the two layers. Incident photons with a total power P_0 and wavelength λ are absorbed and generate the photocurrent I_{ph}, which is equivalent to the base current I_{B} and can be calculated accordingly as

$$I_{\mathrm{B}} \mathrel{\hat{=}} I_{\mathrm{ph}} = (1-R)\cdot\left(1-\exp\left(-\alpha d\right)\right)\cdot\frac{q\lambda}{hc}\cdot P_0\,. \tag{1}$$

R is the intensity reflection coefficient of the surface due to the refractive index step from air to semiconductor, q the elementary charge, h is Planck's constant, and c the vacuum velocity of light. Thus, no external base current is necessary. In active operation, the applied voltage U_{EC} between the emitter and collector layers should be positive. Hence, the electrons of the photocurrent are swept directly through the n-doped base towards the p-emitter layer, where the integrated heterojunction blocks the majority of these free carriers to prevent them from recombining with the holes. Due to the charge neutrality of the base, this leads to an injection of holes into the base layer, the so-called collector

hole current I_C [4]. The ratio between the collector and base current is defined as current gain [5]

$$\beta = I_C/I_B. \tag{2}$$

High current gain requires $w_B \ll L_D$, where w_B is the width of the base and L_D represents the diffusion length of the holes in the n-base. Otherwise, the recombination in the base would decrease I_C and hence the current gain dramatically. Moreover, w_B should not be chosen too thin. This would lead to an early breakdown of the device at low U_{EC}, where the collector current rises exponentially. This occurs when both depletion zones, namely of the emitter–base and base–collector junctions, touch before current-mode operation (where I_C is quasi independent of U_{EC}) could be reached. The breakdown voltage can be adjusted by a proper choice of the doping concentrations of the base $N_{n,B}$ and the collector $N_{p,C}$. Therefore, for common devices, $N_{n,B} > N_{p,C}$ should be valid. As a result, the base–collector depletion zone spreads almost completely into the collector region. Normally, it also makes sense to dope the emitter more than the base ($N_{p,E} > N_{n,B}$), which limits the recombination current at the emitter–base junction. However, due to the integrated potential barrier at the interface, this requirement can be neglected.

2. Experimental

To investigate fabricated GaAs-based HPTs with respect to their output characteristics, breakdown voltage, current gain, and spectral absorption behavior, the measurement setup shown in Fig. 1 (left) is used. Light emitted from a VCSEL with defined wavelength is collimated and focused on an HPT. The intensity of the light can be adjusted by the current source in the circuit. U_{EC} is delivered by a controllable voltage source with integrated amperemeter to measure the collector current I_C. For spectral studies, the wavelength can be changed by replacing the VCSEL device. Four different wavelengths are available here, namely 980, 995, 1040, and 1130 nm. For refined measurements, a monochromator with external lock-in amplifier was used for illumination. Figure 1 (right) shows the schematic layer structure of the HPT, grown by molecular beam epitaxy (MBE). Above the GaAs substrate, the p-doped collector encloses the InGaAs absorption layer with the n-doped base. The absorption layer consists of a 5 nm thick quantum well (QW), which is embedded between two undoped GaAs barrier layers to guarantee intrinsic characteristics. The emitter layer on top of the HPT stack consists of two equally p-doped layers of GaAs and AlGaAs, forming the required heterojunction. To contact the HPT electrically, Ti/Pt/Au top and bottom contacts are evaporated.

2.1 Output characteristics

Calculations of the current gain by (2) require investigations on the output characteristics of the transistor. First measurements of the grown HPT, represented in Fig. 2 (left), show no perceivable current-source mode and only small collector currents in the low µA-range for vanishing optical input powers P. As expected, with increasing P at $\lambda = 980$ nm, I_C raises slightly because of the higher amount of absorbed photons. This HPT does not

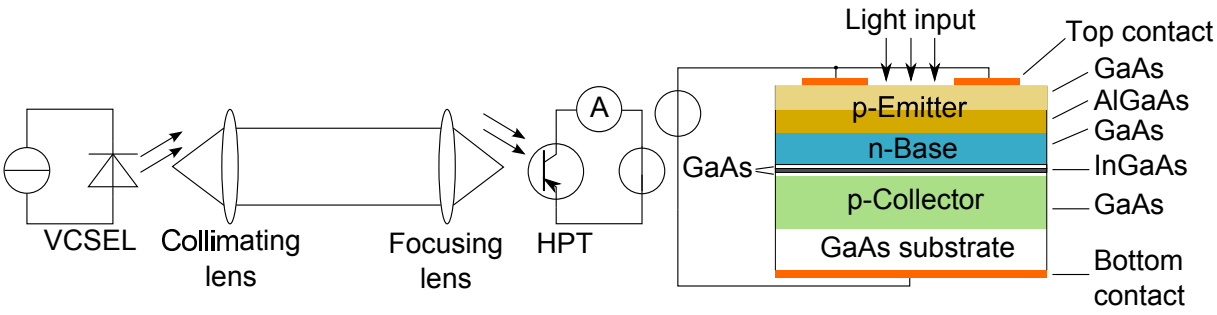

Fig. 1: Measurement setup for optoelectronic investigations on HPTs (left) and schematic layer structure of the GaAs-based HPT (right).

exhibit any current confinement. In consequence, the collector current spreads laterally over the wafer sample and is influenced by the sheet resistance. To force the current to propagate directly through the device and thus reduce lateral leakage currents, a mesa was wet-chemically etched. The output characteristics of the mesa-etched device are shown in Fig. 2 (right). Increasing U_{EC}, three operating regions can clearly be distinguished: The saturation region, the current-source mode, and the breakdown region. The saturation region occurs at low U_{EC} when both pn-junctions, namely of the emitter–base and base–collector, are biased in forward direction. However, the magnitude of the collector current is also decreased, probably due to surface leakage currents along the mesa walls.

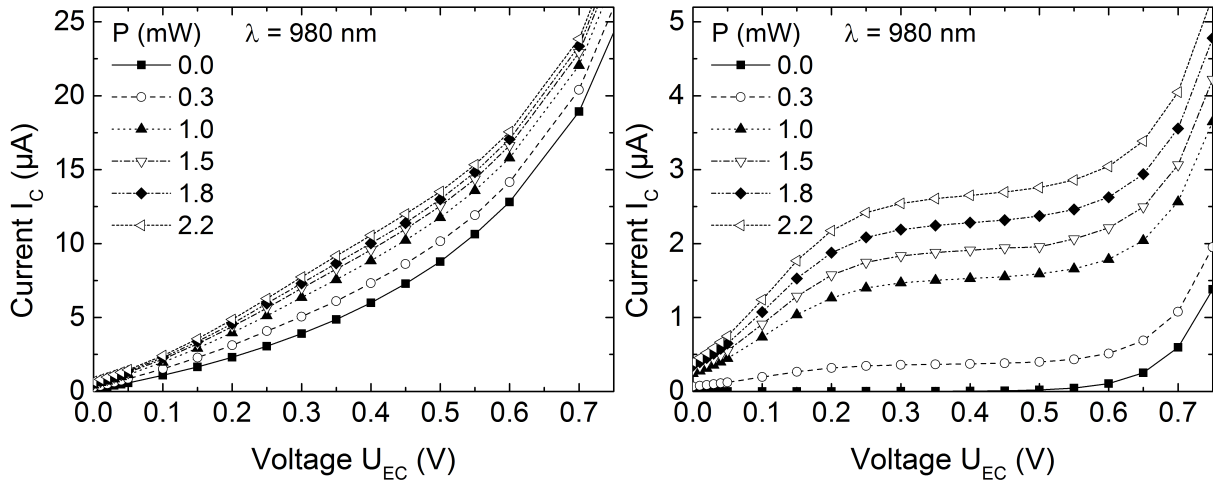

Fig. 2: Measured output characteristics of planar (left) and mesa-etched HPTs using a 980 nm VCSEL for illumination (right).

Calculations of the current gain applying (1) and (2) result in $\beta \approx 1$. This behavior is known and well explained in the literature using the so-called Gummel plot [6]. Low collector currents result in low current gains due to high recombination currents in the emitter–base depletion zone and surface and interface leakage currents. To minimize these effects, the collector current must be increased. This can be solved easily by raising the incident optical power or by ensuring more efficient light absorption.

2.2 Resonant-cavity-enhanced phototransistors

The VCSEL output power cannot be increased arbitrarily because of thermal roll-over. Hence, the light intensity must be increased in a different way. Therefore, the HPT is embedded between two Bragg reflectors, as seen in Fig. 3 (left), to form a resonant cavity. The top Bragg reflector has a reflectivity of $R_\mathrm{t} \approx 0.7$, whereas $R_\mathrm{b} \approx 1$ for the bottom mirror. The resonant cavity raises the probability of a photon to be absorbed by the InGaAs QW by a factor of $M \approx 2/\left(1 - R_\mathrm{t}R_\mathrm{b}\right) \approx 6.7$, where $M/2$ represents the effective number of round-trips of the photon in the resonator. Hence, the quantum efficiency is strongly increased [2]. Measurements of the reflection spectrum of the device clearly show a resonance dip at 1040 nm, which requires using a VCSEL with similar wavelength for external illumination.

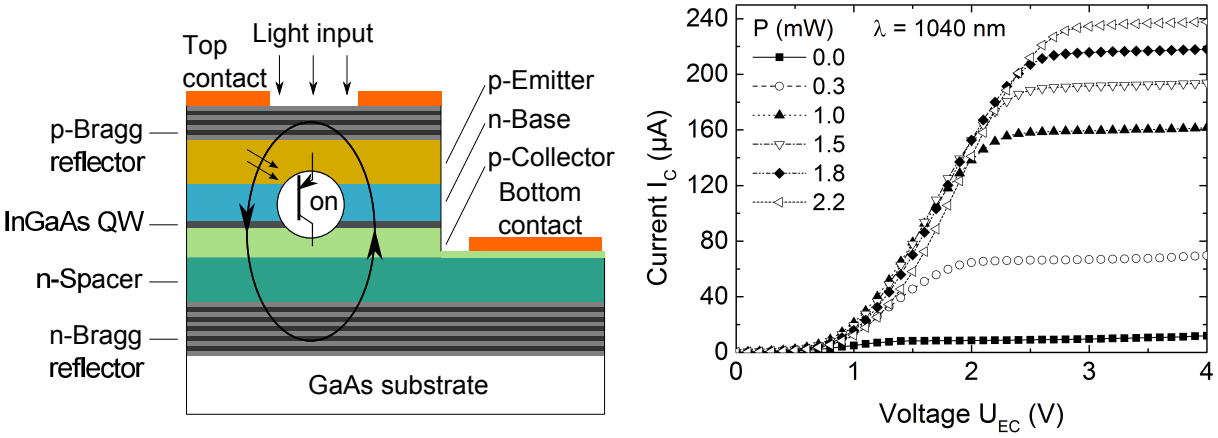

Fig. 3: Schematic layer structure of a resonant-cavity-enhanced phototransistor (left) and measured output characteristic with an incident photon wavelength of 1040 nm (right).

Figure 3 (right) depicts the results of the measured output characteristics. Qwing to a decreased collector doping concentration in comparison to the HPT of Sect. 2.1, the breakdown voltage has raised up to ≈ 7 V. The collector current now reaches 240 µA for an incident optical power of 2.2 mW. Compared to the results seen in Fig. 2 (right), the collector current has increased almost by a factor of 80. Taking the increased quantum efficiency of the resonant cavity into account, the calculated current gain of the HPT is $\beta \approx 165$. This proves the functionality of the phototransistor and confirms the theory of the Gummel plot.

2.3 Spectral investigations

As described in the introduction of Sect. 2, the InGaAs QW is responsible for the absorption of the incident photons. To adjust the wavelength sensitivity of the HPT, it is necessary to do spectral investigations of the absorption coefficient of the QW. As a first step, we have measured the output characteristics of the HPT using the above mentioned four VCSELs with different wavelengths (Fig. 4 (left)). The bandgap wavelengths λ_g of GaAs and the AlGaAs material in the HPT amount to 875 nm and 722 nm, respectively,

which means that the material is transparent when using the 980 nm VCSEL. The target λ_g of the $In_{0.27}Ga_{0.73}As$ QW absorbing layer is 1074 nm. At $\lambda = 1130$ nm the curve is similar to the dark current. Because of the low energy of the photons, absorption in the InGaAs QW is not possible, in contrast to measurements using the 1040 nm VCSEL. Hence, the bandgap wavelength of the QW could be estimated to 1040 nm $\leq \lambda_g \leq$ 1130 nm. A further decrease of the photon wavelength results in a slight increase of the collector current.

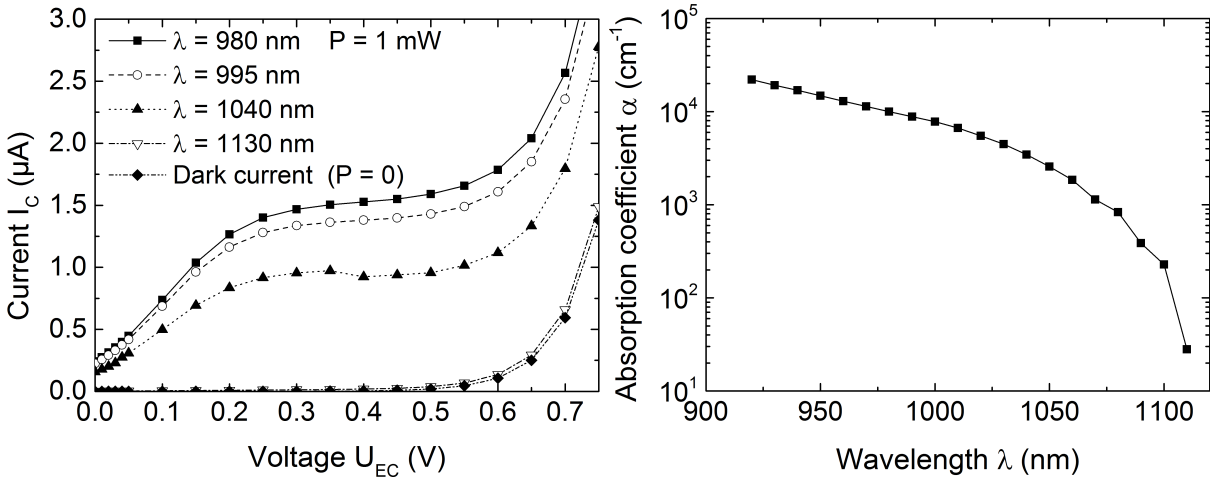

Fig. 4: HPT output characteristics for four different VCSEL wavelengths at an optical power of 1 mW (left) and measured spectral absorption coefficient of an $In_{0.27}Ga_{0.73}As$ QW using a monochromator (right).

More accurate measurements were possible by substituting the VCSEL by a halogen lamp and a monochromator. The low spectral power density required the use of a lock-in amplifier. Assuming an absorption coefficient of $\alpha = 10^4\,\mathrm{cm}^{-1}$ at $\lambda = 980$ nm, the wavelength-dependent absorption coefficient can be calculated using (2) and (1), as shown in Fig. 4 (right). There is a strong drop of α towards long wavelengths (note the logarithmic scale), however, a band edge wavelength cannot be easily identified. As an estimation, 1070 nm $\leq \lambda_g \leq$ 1100 nm. This interval includes the design λ_g of the QW.

3. Conclusion

We have investigated heterojunction phototransistors in order to achieve high current gain and to determine the spectral absorption coefficient of the InGaAs QW absorbing layer in the collector–base depletion zone. We have shown the advantages of mesa-etched structures and have reached high current gain using a resonant-cavity-enhanced HPT, in which the absorption probability of the photons is increased. Although the experimental absorption spectrum shows a more gradual decrease towards the band edge than expected, λ_g can be estimated and is in good agreement with the target bandgap wavelength.

Acknowledgment

We thank Philips Technologie GmbH (U-L-M Photonics) for the MBE growth of the phototransistors and Dr.-Ing. Philipp Gerlach for supplying the transistor and laser samples as well as numerous and fruitful discussions. Also we acknowledge the technical contributions of Rudolf Rösch.

References

[1] R.A. Milano, P.D. Dapkus, and G.E. Stillman, "An analysis of the performance of heterojunction phototransistors for fiber optic communications", *IEEE Trans. Electron Dev.*, vol. 29, pp. 266–274, 1982.

[2] M.S. Ünlü, K. Kishino, J.-I. Chyi, L. Arsenault, J. Reed, S.N. Mohammad, and H. Morkoç, "Resonant cavity enhanced AlGaAs/GaAs heterojunction phototransistors with an intermediate InGaAs layer in the collector", *Appl. Phys. Lett.*, vol. 57, pp. 750–752, 1990.

[3] F. Träger, *Springer Handbook of Lasers and Optics.* Berlin: Springer, 2012.

[4] N. Chand, P.A. Houston, and P.N. Robson, "Gain of a heterojunction bipolar phototransistor", *IEEE Trans. Electron Dev.*, vol. 32, pp. 622–627, 1985.

[5] N. Pan, J. Elliott, M. Knowles, D.P. Vu, K. Kishimoto, J.K. Twynam, H. Sato, M.T. Fresina, and G.E. Stillman, "High reliability InGaP/GaAs HBT", *IEEE Electron Dev. Lett.*, vol. 19, pp. 115–117, 1998.

[6] S.M. Sze, *Physics of Semiconductor Devices.* New York: John Wiley and Sons, 1981.

Ph.D. Theses

1. Ahmed Al-Samaneh,
   VCSELs for Cesium-Based Miniaturized Atomic Clocks,
   March 2014.

2. Dario Schiavon,
   Analysis of the Green Gap Problem in III-Nitride LEDs,
   September 2014.

3. Mohamed Fikry,
   Epitaxial Growth and Characterization of Coaxial GaN/InGaN/GaN Nano-Structures,
   October 2014.

4. Alexander Kern,
   Monolithically Integrated Transceiver Chips for Bidirectional Optical Data Transmission,
   November 2014.

5. Anna Bergmann,
   Optische Partikelmanipulation in mikrofluidischen Kanälen mit Hilfe integrierter VCSEL-basierter optischer Fallen,
   December 2014.

Master Theses

1. Zongzhe Cheng,
   Influence of Micro- and Nanostructuring of r-Plane Sapphire Wafers on MOVPE Growth of (11-22) Oriented GaN,
   March 2014.

2. Oliver Rettig,
   Nitridische Nanosäulen – Design und Wachstum für Sensoranwendungen,
   December 2014.

Bachelor Theses

1. Markus Polanik,
   Experimentelle Charakterisierung von optisch gepumpten Halbleiterscheibenlasern mit Oberflächenpassivierungen durch SiO_2, Al_2O_3, Ta_2O_5 und TiO_2,
   January 2014.

2. Tianyi Wen,
   Investigations on the Etching Behavior of Different GaN Crystal Orientations and Polarities,
   May 2014.

3. Xu Zhang,
   MATLAB-based Test System for Automatic Acquisition of Internal Quantum Efficiency for InGaN Quantum-Well Structure LEDs over GPIB,
   May 2014.

4. Johannes Bläsi,
   Untersuchung des Doppelbrechungs- und Polarisationsverhaltens bei Vertikallaserdioden unter mechanischer Verspannung,
   September 2014.

Talks and Conference Contributions

[1] M. Caliebe, T. Meisch, M. Madel, Z. Cheng, B. Neuschl, J. Helbing, K. Thonke, and F. Scholz, "Surface roughness optimization of (11-22) oriented GaN grown by MOVPE", poster at *17th International Conference on Metalorganic Vapor Phase Epitaxy, ICMOVPE*, Lausanne, Switzerland, July 2014.

[2] M. Caliebe, "Influence of sapphire miscut and MOVPE parameters on (11-22) oriented GaN grown on prestructured substrates", seminar talk, *PolarCoN, Summer School*, Bensheim, Germany, September 2014.

[3] M. Caliebe, T. Meisch, F. Scholz, M. Hocker, K. Thonke, Y. Han, and C. Humphreys, "Growth of semipolar GaN on patterned sapphire wafers", *Solid State Lighting (SSL) Symposium*, Lund University, Lund, Sweden, November 2014.

[4] Z. Cheng, "MOVPE growth of (11-22) oriented GaN on deep UV lithography structured r-plane sapphire substrates", seminar talk, *PolarCoN, Summer School*, Bensheim, Germany, September 2014.

[5] M. Daubenschüz, P. Gerlach, and R. Michalzik, "Electro-thermal characteristics of VCSELs: simulations and experiments", poster at *SPIE Photonics Europe*, Conf. on *Semiconductor Lasers and Laser Dynamics VI*, Brussels, Belgium, April 2014.

[6] D. Heinz, O. Rettig, F. Huber, M. Madel, M. Asad, J. Jakob, I. Tischer, M. Hocker, S. Jenisch, K. Thonke, and F. Scholz, "GaInN nanowires for optical hydrogen sensing", poster at *8th Nanowires Growth Workshop, Nanowires 2014*, Eindhoven, Netherlands, August 2014.

[7] N.I. Khan, A. Bergmann, and R. Michalzik, "Miniaturized VCSEL modules for optical manipulation of microparticles", *8th Int. Conf. on Electr. and Computer Engin., ICECE*, Dhaka, Bangladesh, December 2014.

[8] M. Klein, T. Meisch, A. Aida, N. Aota, H. Takeda, K. Koyama, and F. Scholz, "The influence of prebowed sapphire wafers on self separated GaN layers in hydride vapor phase epitaxy", poster at *International Workshop on Nitride Semiconductors, IWN*, Wroclaw, Poland, August 2014.

[9] R.A.R. Leute, J. Wang, T. Meisch, B. Neuschl, K. Thonke, and F. Scholz, "Light emitters based on GaN nano-stripes with semipolar quantum wells", *DPG Spring Meeting*, Dresden, Germany, March 2014.

[10] R.A.R. Leute, J. Wang, T. Meisch, M. Caliebe, M. Klein, and F. Scholz, "Growth of semipolar gallium nitride structures on sapphire" (invited), *International Symposium on Growth of III Nitrides, ISGN-5*, Atlanta, GA, USA, June 2014.

[11] R.A.R. Leute, D. Heinz, J. Wang, T. Meisch, J. Biskupek, U. Kaiser, F. Huber, O. Rettig, K. Thonke, and F. Scholz, "GaN nanostripes with semipolar quantum wells", *PolarCoN Summer School 2014*, Bensheim, Germany, September 2014.

[12] R.A.R. Leute, T. Meisch, J. Wang, J. Biskupek, U. Kaiser, M. Müller, P. Veit, F. Bertram, J. Christen, and F. Scholz, "GaN nano-stripes for laser devices", *European Semiconductor Laser Workshop, ESLW 2014*, Paris, France, September 2014.

[13] R.A.R. Leute, "LEDs — Herausforderungen für die Zukunft" (invited), *Ringvorlesung Ulmer 3-Generationen Universität u3gu*, Ulm, Germany, October 2014.

[14] R.A.R. Leute, D. Heinz, O. Rettig, T. Meisch, S. Jenisch, S. Strehle, and F. Scholz, "Selective area epitaxy of GaN stripes with sub-200-nm periodicity", *29th DGKK Workshop Epitaxie von III/V-Halbleitern*, Magdeburg, Germany, December 2014.

[15] T. Meisch, M. Alimoradi-Jazi, B. Neuschl, M. Klein, I. Tischer, K. Thonke, and F. Scholz, "(20-21) GaN growth on 2" patterned sapphire substrates", *SPIE Photonics West*, Conf. on *Gallium Nitride Materials and Devices IX*, San Francisco, CA, USA, February 2014.

[16] T. Meisch, S. Schörner, J. Wang, K. Thonke, and F. Scholz, "InGaN/GaN LEDs grown on 2" patterned sapphire substrates", *DPG Spring Meeting*, Dresden, Germany, April 2014.

[17] F. Scholz, M. Caliebe, T. Meisch, M. Alimoradi-Jazi, Z. Cheng, and M. Klein, "Large area semipolar GaN-GaInN hetereo structures grown on foreign substrates" (invited), *225th Meeting of the Electrochemical Society*, Orlando, FL, USA, May 2014.

[18] F. Scholz, T. Meisch, M. Caliebe, B. Neuschl, and K. Thonke, "Semipolar GaN-based optoelectronic structures on large area substrates" (invited), *CIMTEC 6th Forum on New Materials*, Montecatini Terme, Italy, June 2014.

[19] F. Scholz, T. Meisch, M. Alimoradi, M. Caliebe, M. Klein, M. Hocker, B. Neuschl, I. Tischer, and K. Thonke, "Current status of semipolar and nonpolar GaN" (invited), *International Workshop on Nitride Semiconductors, IWN*, Wroclaw, Poland, August 2014.

[20] F. Scholz, "Nobles Licht revolutioniert nicht nur die Beleuchtungstechnologie" (invited), *Physikalisches Kolloquium*, University Ulm, Germany, November 2014.

[21] F. Scholz, M. Caliebe, T. Meisch, M. Alimoradi-Jazi, M. Klein, M. Hocker, B. Neuschl, I. Tischer, and K. Thonke, "Large area semipolar GaN heterostructures grown on patterned sapphire wafers" (invited), *MRS Fall Meeting*, Boston, USA, December 2014.

[22] J. Wang, D. Zhang, and F. Scholz, "Improvement of $\{10\bar{1}1\}$ InGaN/GaN LEDs via optimization of InGaN MOVPE growth conditions", *17th International Conference of Metalorganic Vapor Phase Epitaxy*, Lausanne, Switzerland, July 2014.

[23] S. Bauer, M. Hocker, L. Hiller, F. Lipski, F. Scholz, and K. Thonke, "Microphotoluminescence and micro-Raman studies on strained polar GaN layers", *DPG Spring Meeting*, Dresden, Germany, April 2014.

[24] M. Bou Sanayeh, A. Bergmann, and R. Michalzik, "Simultaneous optical manipulation of multiple particles inside microfluidic channels using one rectangular-shaped VCSEL", poster at *SPIE Photonics Europe*, Conf. on *Biophotonics: Photonic Solutions for Better Health Care III*, Brussels, Belgium, April 2014.

[25] F. Brunner, D. Prasai, W. John, M. Caliebe, F. Scholz, O. Krüger, and M. Weyers, "Semipolar (11-22) GaN templates grown on 100 mm trench-patterned r-plane sapphire", *International Workshop on Nitride Semiconductors, IWN*, Wroclaw, Poland, August 2014.

[26] E.R. Buss, U. Rossow, H. Bremers, T. Meisch, F. Scholz, and A. Hangleiter, "Growth and characterization of non- and semipolar AlInN and possibilities for relaxed buffer layer engineering", *DPG Spring Meeting*, Dresden, Germany, April 2014.

[27] D.V. Dinh, M. Hocker, T. Meyer, M. Caliebe, M. Pristovsek, K. Thonke, F. Scholz, C.J. Humphreys, and P.J. Parbrook, "Luminescence Properties of semipolar (11-22) InGaN single quantum wells", poster at *International Workshop on Nitride Semiconductors, IWN*, Wroclaw, Poland, August 2014.

[28] Y. Han, M. Caliebe, M. Kappers, F. Scholz, and C. Humphreys, "Structural characterisation of semi-polar (11-22) GaN templates grown on pre-structured r-plane sapphire substrates", poster at *International Workshop on Nitride Semiconductors, IWN*, Wroclaw, Poland, August 2014.

[29] C.R. Head, A. Hein, E.A. Shaw, A.P. Turnbull, P. Unger, and A.C. Tropper, "Femtosecond mode-locked VECSEL from widely cw-tunable gain chips", poster at *Conf. on Lasers and Electro-Optics, CLEO 2014*, San Jose, CA, USA, June 2014.

[30] L. Hiller, P. Schustek, M. Hocker, S. Bauer, M. Caliebe, T. Meisch, F. Scholz, and K. Thonke, "Analysis of semipolar gallium nitride layers by micro-Raman spectroscopy", poster at *DPG Spring Meeting*, Dresden, Germany, March 2014.

[31] M. Hocker, I. Tischer, B. Neuschl, J. Helbing, J. Wang, F. Scholz, and K. Thonke, "Cathodoluminescence mapping on differently inclined semipolar InGaN facets", *DPG Spring Meeting*, Dresden, Germany, April 2014.

[32] M. Knab, M. Hocker, I. Tischer, J. Wang, F. Scholz, and K. Thonke, "Development of a dedicated low noise EBIC measurement system", poster at *DPG Spring Meeting*, Dresden, Germany, April 2014.

[33] G. Kozlowski, D.V. Dinh, S. Presa, P.P. Maaskant, P.J. Parbrook, M. Caliebe, F. Scholz, and B. Corbett, "Chemical-mechanical polishing of semi-polar (11-22) GaN templates for use in LEDs", *International Workshop on Nitride Semiconductors, IWN*, Wroclaw, Poland, August 2014.

[34] C. Laurus, T. Aschenbrenner, E. Zakizadeh, S. Figge, D. Hommel, J. Wang, and F. Scholz, "Growth and characterisation of InGaN quantum dots on AlGaN-Templates", *DPG Spring Meeting*, Dresden, Germany, April 2014.

[35] S. Metzner, F. Bertram, T. Hempel, T. Meisch, S. Schwaiger, F. Scholz, and J. Christen, "Correlation of optical properties and defect structures of semipolar GaN on pre-patterned sapphire substrates using cathodoluminescence microscopy", *SPIE Photonics West*, Conf. on *Gallium Nitride Materials and Devices IX*, San Francisco, CA, USA, February 2014.

[36] S. Metzner, M. Müller, G. Schmidt, B. Max, P. Veit, S. Petzold, F. Bertram, R.A.R. Leute, D. Heinz, J. Wang, F. Scholz, and J. Christen, "Optical and structural nano-characterization of GaN based LED structures with semipolar sub-µm patterned InGaN QWs", *DPG Spring Meeting*, Dresden, Germany, April 2014.

[37] M. Müller, S. Metzner, G. Schmidt, P. Veit, S. Petzold, F. Bertram, J. Christen, R. Leute, D. Heinz, J. Wang, T. Meisch, and F. Scholz, "Nanoscale imaging of GaN-based LED structures with semipolar InGaN QWs using scanning transmission electron microscope cathodoluminescence", *SPIE Photonics West*, Conf. on *Gallium Nitride Materials and Devices IX*, San Francisco, CA, USA, February 2014.

[38] B. Neuschl, J. Helbing, M. Knab, H. Lauer, T. Meisch, K. Forghani, F. Scholz, and K. Thonke, "Valence band order in c-oriented wurtzite AlGaN layers", *DPG Spring Meeting*, Dresden, Germany, April 2014.

[39] I. Tischer, M. Frey, M. Hocker, R.A.R. Leute, F. Scholz, H. Groiss, E. Müller, D. Gerthsen, W. v. Mierlo, J. Biskupek, U. Kaiser, and K. Thonke, "Direct identification of luminescence from I1 type basal plane stacking faults in semipolar AlGaN layers with low Al content", *DPG Spring Meeting*, Dresden, Germany, April 2014.

Publications

[1] M. Caliebe, T. Meisch, B. Neuschl, S. Bauer, J. Helbing, D. Beck, K. Thonke, M. Klein, D. Heinz, and F. Scholz, "Improvements of MOVPE grown $(11\bar{2}2)$ oriented GaN on pre-structured sapphire substrates using a SiN_x interlayer and HVPE overgrowth", *Phys. Status Solidi C*, vol. 11, pp. 525–529, 2014.

[2] M. Daubenschüz, P. Gerlach, and R. Michalzik, "Electro-thermal characteristics of VCSELs: simulations and experiments", in *Semiconductor Lasers and Laser Dynamics VI*, K.P. Panajotov, M. Sciamanna, A.A. Valle, R. Michalzik (Eds.), Proc. SPIE 9134, pp. 91342H-1–8, 2014.

[3] D. Heinz, M. Fikry, T. Aschenbrenner, M. Schowalter, T. Meisch, M. Madel, F. Huber, M. Hocker, M. Frey, I. Tischer, B. Neuschl, T. Mehrtens, K. Müller, A. Rosenauer, D. Hommel, K. Thonke, and F. Scholz, "GaN tubes with coaxial non- and semipolar GaInN quantum wells", *Phys. Status Solidi C*, vol. 11, pp. 648–651, 2014.

[4] N.I. Khan, A. Bergmann, and R. Michalzik, "Miniaturized VCSEL modules for optical manipulation of microparticles", in Proc. *8th Int. Conf. on Electr. and Computer Engin., ICECE*, pp. 246–249. Dhaka, Bangladesh, December 2014.

[5] M. Klein, T. Meisch, F. Lipski, and F. Scholz, "The influence of prestrained metalorganic vapor phase epitaxial gallium-nitride templates on hydride vapor phase epitaxial growth", *Appl. Phys. Lett.*, vol. 105, pp. 092109-1–4, 2014.

[6] T. Meisch, M. Alimoradi-Jazi, B. Neuschl, M. Klein, I. Tischer, K. Thonke, and F. Scholz, "Crystal quality improvement of semipolar (20-21) GaN on patterned sapphire substrates by in-situ deposited SiN mask", in *Gallium Nitride Materials and Devices IX*, J.-I. Chyi, Y. Nanishi, H. Morkoç, J. Piprek, E. Yoon, H. Fujioka (Eds.), Proc. SPIE 8986, pp. 89860A-1–7, 2014.

[7] T. Meisch, M. Alimoradi-Jazi, M. Klein, and F. Scholz, "(20-21) MOVPE and HVPE GaN grown on 2" patterned sapphire substrates", *Phys. Status Solidi C*, vol. 11, pp. 537–540, 2014.

[8] S.S. Rahman, R.A.R. Leute, J. Wang, T. Meisch, M. Klein, F. Scholz, K. Koyama, M. Ishii, and H. Takeda, "LEDs on HVPE grown GaN substrates: influence of macroscopic surface features", *AIP Advances*, vol. 4, pp. 077119-1–8, 2014.

[9] F. Scholz, T. Meisch, M. Caliebe, S. Schörner, K. Thonke, L. Kirste, S. Bauer, S. Lazarev, and T. Baumbach, "Growth and doping of semipolar GaN grown on patterned sapphire substrates", *J. Cryst. Growth*, vol. 405, pp. 97–101, 2014.

[10] J. Wang, Y. Gao, S. Alam, and F. Scholz, "Mg doping of 3D semipolar InGaN/GaN-based light emitting diodes", *Phys. Status Solidi A*, vol. 211, pp. 2645–2649, 2014.

[11] M. Bou Sanayeh, A. Bergmann, and R. Michalzik, "Simultaneous optical manipulation of multiple particles inside microfluidic channels using one rectangular-shaped VCSEL", in *Biophotonics: Photonic Solutions for Better Health Care III*, J. Popp, V.V. Tuchin, D.L. Matthews, F.S. Pavone (Eds.), Proc. SPIE 9129, pp. 91292O-1–7, 2014.

[12] E.R. Buss, U. Rossow, H. Bremers, T. Meisch, M. Caliebe, F. Scholz, and A. Hangleiter, "Intentional anisotropic strain relaxation in $\{11\bar{2}2\}$ oriented $Al_{1-x}In_xN$ one-dimensionally lattice matched to GaN", *Appl. Phys. Lett.*, vol. 105, pp. 122109-1–4, 2014.

[13] D.V. Dinh, F. Oehler, V.Z. Zubialevich, M.J. Kappers, S.N. Alam, M. Caliebe, F. Scholz, C.J. Humphreys, and P.J. Parbrook, "Comparative study of polar and semipolar $\{11\bar{2}2\}$ InGaN layers grown by metalorganic vapour phase epitaxy", *J. Appl. Phys.*, vol. 116, pp. 153505-1–7, 2014.

[14] C.R. Head, A. Hein, E.A. Shaw, A.P. Turnbull, P. Unger, and A.C. Tropper, "Femtosecond mode-locked VECSEL from widely cw-tunable gain chips", in Proc. *Conf. on Lasers and Electro-Optics, CLEO 2014*, paper JTu4A.120, two pages. San Jose, CA, USA, June 2014.

[15] B. Neuschl, J. Helbing, M. Knab, H. Lauer, M. Madel, K. Thonke, T. Meisch, K. Forghani, F. Scholz, and M. Feneberg, "Composition dependent valence band order in c-oriented wurtzite AlGaN layers", *J. Appl. Phys.*, vol. 116, pp. 113506-1–8, 2014.

[16] B. Neuschl, J. Helbing, K. Thonke, T. Meisch, J. Wang, and F. Scholz, "Optical absorption of polar and semipolar InGaN/GaN quantum wells for blue to green converter structures", *J. Appl. Phys.*, vol. 116, pp. 183507-1–8, 2014.

[17] P. Schustek, M. Hocker, M. Klein, U. Simon, F. Scholz, and K. Thonke, "Spectroscopic study of semipolar (11-22)-HVPE GaN exhibiting high oxygen incorporation", *J. Appl. Phys.*, vol. 116, pp. 163515-1–9, 2014.

[18] I. Tischer, M. Frey, M. Hocker, L. Jerg, M. Madel, B. Neuschl, K. Thonke, R.A.R. Leute, F. Scholz, H. Groiss, E. Müller, and D. Gerthsen, "Basal plane stacking faults in semipolar AlGaN: hints to Al redistribution", *Phys. Status Solidi B*, vol. 251, pp. 2321–2325, 2014.

ulm university universität ulm

Ulm University
Institute of Optoelectronics
Albert-Einstein-Allee 45
89081 Ulm | Germany

Ulm University | Institute of Optoelectronics | Annual Report 2014